**REPUBLIC OF TÜRKİYE**
**YILDIZ TECHNICAL UNIVERSITY**
**GRADUATE SCHOOL OF SCIENCE AND ENGINEERING**

# FINITE ELEMENT ANALYSIS OF REINFORCED CONCRETE BEAMS INCORPORATING A FRICTIONAL AND ELASTOMERIC SEISMIC ENERGY DISSIPATION DEVICE

**Lal OĞUZ**

MASTER OF SCIENCE THESIS
Department of Civil Engineering
Program of Structural Engineering

Supervisor
Asst. Prof. Dr. Orkun YILMAZ

July, 2026

**REPUBLIC OF TÜRKİYE**

**YILDIZ TECHNICAL UNIVERSITY**

**GRADUATE SCHOOL OF SCIENCE AND ENGINEERING**

# FINITE ELEMENT ANALYSIS OF REINFORCED CONCRETE BEAMS INCORPORATING A FRICTIONAL AND ELASTOMERIC SEISMIC ENERGY DISSIPATION DEVICE

A thesis submitted by Lal OĞUZ in partial fulfillment of the requirements for the degree of **MASTER OF SCIENCE** is approved by the committee on 30.07.2026 in Department of Civil Engineering, Program of Structural Engineering.

Asst. Prof. Dr. Orkun YILMAZ
Yildiz Technical University
Supervisor

**Approved By the Examining Committee**

Asst. Prof. Dr. Orkun YILMAZ, Supervisor
Yildiz Technical University _____

Prof. Dr. Serkan BEKİROĞLU, Member
Yildiz Technical University _____

Prof. Dr. Hasan ÖZKAYNAK, Member
Beykent University _____

I hereby declare that the study entitled “Finite Element Analysis of Reinforced Concrete Beams Incorporating a Frictional and Elastomeric Seismic Energy Dissipation Device” that I prepared under the supervision of Asst. Prof. Dr. Orkun YILMAZ was conducted in full compliance with the relevant legal requirements regarding data collection and data use; that all information obtained from other sources has been fully and properly acknowledged in the main text and references; that no fabrication and/or falsification has been made with respect to the research data or findings; and that throughout the study I have adhered to the principles of scientific research and academic ethics.

In the course of this thesis study, Generative Artificial Intelligence (GenAI) tools—specifically ChatGPT (GPT-5.6 Luna) were utilized under the author’s supervision for purposes such as enhancing linguistic clarity and coherence and conducting literature review.

I declare that I am aware of the risk that GenAI tools may generate inaccurate or fabricated information (hallucinations), and that I have carefully reviewed and verified all outputs obtained from these tools in terms of accuracy, integrity, reliability, and compliance with ethical standards.

The use of GenAI tools has not, at any stage, replaced the author’s intellectual contribution, scientific judgment, or original idea generation. Full responsibility for the accuracy, currency, and scientific validity of all information, data, analyses, claims, and references presented in this thesis rests entirely with me.

I accept full administrative and legal responsibility for any consequences that may arise if this declaration is determined to be false.

Lal OĞUZ

Signature

*Dedicated to my family*

# ACKNOWLEDGEMENT

During my master's studies and throughout the preparation of this thesis, I would like to express my sincere gratitude to my advisor, Asst. Prof. Dr. Orkun YILMAZ, for his guidance, support, and encouragement, as well as for sharing his knowledge, experience, and academic expertise with me. His valuable contributions have been instrumental both in broadening my scientific perspective and in shaping this study.

I would also like to express my sincere gratitude to Prof. Dr. Serkan BEKİROĞLU for his valuable guidance, support, and contributions throughout the preparation of this thesis. His knowledge, experience, and constructive feedback have been greatly appreciated and have contributed significantly to the development of this study.

I would also like to thank Prof. Dr. Hasan ÖZKAYNAK for taking the time to evaluate this thesis and for his valuable comments and suggestions, which contributed to the improvement of this study.

Finally, I would like to thank all my professors who contributed to my academic development throughout my graduate education by sharing their knowledge and experience.

Lal OĞUZ

# TABLE OF CONTENTS

**LIST OF SYMBOLS** ix
**LIST OF ABBREVIATIONS** x
**LIST OF FIGURES** xi
**LIST OF TABLES** xiv
**ABSTRACT** xv
**ÖZET** xvii
**1 INTRODUCTION** 1
1.1 Seismic Damage and Energy Dissipation in Reinforced Concrete Structures ..... 1
1.2 Fuse-Type Energy Dissipation Systems in Reinforced Concrete Structures ..... 3
1.3 Fuse-Type Energy Dissipation Systems in Steel Structures ..... 7
1.4 Steel Friction-Based Fuse Systems ..... 11
1.5 Hybrid and Replaceable Fuse Systems in Steel Frames ..... 13
1.6 Aim of the Thesis ..... 20
1.7 Hypothesis ..... 21
**2 FRICTIONAL AND ELASTOMERIC SEISMIC DEVICE** 22
2.1 General Structure and Components of the Device ..... 22
2.1.1 Steel Body Plates ..... 23
2.1.2 Master Pin ..... 23
2.1.3 Additional Bolts ..... 24
2.1.4 Stiffness Member ..... 24
2.1.5 Friction Members ..... 24
2.1.6 Elastomeric Element ..... 24
2.2 Calculation of the Moment-Carrying Capacity of the Seismic Connection Device ..... 25
**3 GENERAL INFORMATION ON THE CONCEPTS DISCUSSED IN THE THESIS** 27
3.1 Finite Element Method (FEM) ..... 27
3.2 Finite Element Types in Ansys ..... 29

3.3 Contacts ..... 32
3.3.1 Contact Elements ..... 32
3.3.2 Contact Types ..... 32
3.4 Material Models ..... 33
3.4.1 Plasticity Models ..... 33
3.4.2 Concrete Model – Menétrey–Willam Model ..... 34
3.4.3 Hyperelastic Model ..... 34
**4 VERIFICATION OF THE NUMERICAL MODEL 35**
**5 FINITE ELEMENT MODELS 39**
5.1 Idealization ..... 39
5.2 Geometry of RC Beam ..... 41
5.3 Geometry of the RC Beam Integrated With The Seismic Device ..... 42
5.4 Boundary Conditions ..... 45
5.5 Materials and Parameters ..... 45
5.6 Mesh Details ..... 47
5.7 Contacts ..... 49
5.7.1 Bonded Contact Definitions ..... 49
5.7.2 Frictional Contact Definitions ..... 49
5.7.3 Frictionless Contact Definitions ..... 51
5.7.4 Contact Formulation ..... 51
5.8 Loading Protocol ..... 51
5.9 Finite Element Model Configurations ..... 52
**6 RESULTS 56**
6.1 Hysteresis Response of the Prepared Models ..... 56
6.2 Distribution of Plastic Deformations and Failure Modes ..... 62
6.3 Force Transfer in Friction Members ..... 67
6.4 Force Transfer in Elastomeric Pads ..... 70
**7 DISCUSSION 72**
7.1 Effect of Embedment Length and Multiple Plates on Damage Mitigation .. 72
7.1.1 Hysteretic Behavior and Energy Dissipation ..... 72
7.1.2 Plastic Deformation Distributions and Failure Modes ..... 75
7.2 Discussion Of Force Transfer Mechanisms ..... 77
7.2.1 Friction Mechanism ..... 77
7.2.2 Elastomeric Pad Mechanism ..... 80
**8 LIMITATIONS AND FUTURE RESEARCH 81**

**9 CONCLUSION** **84**

**REFERENCES** **86**

**A EFFECT OF LONGITUDINAL PLATE GEOMETRY ON THE SEISMIC PERFORMANCE OF RC BEAMS** **90**

A.1 Geometry of the RC Beam ..... 90

A.1.1 Model 1 ..... 91

A.1.2 Model 2 ..... 92

A.1.3 Model 3 ..... 92

A.2 Results ..... 93

A.2.1 Hysteretic Response ..... 93

A.2.2 Energy Dissipation Capacity ..... 94

A.2.3 Equivalent Plastic Strain Distributions ..... 95

A.3 Discussion ..... 96

**PUBLICATIONS FROM THE THESIS** **97**

# LIST OF SYMBOLS

| | |
|---|---|
| $A_{s'}$ | Area of compression reinforcement |
| $A_s$ | Area of tensile reinforcement |
| $f'_c$ | Compressive strength of concrete |
| $E_d$ | Cumulative energy dissipation |
| $a$ | Depth of equivalent rectangular compression block |
| $d'$ | Distance from extreme compression fiber to compression reinforcement |
| $d$ | Effective depth of the beam section |
| $x_F$ | Effective distance from the center of rotation to the friction members |
| $L_{long}$ | Embedment length of the longitudinal plate |
| $M_{rc}$ | Flexural moment capacity of the reference beam |
| $\mu$ | Friction coefficient of the sliding interface |
| $M_F$ | Frictional moment generated by the friction members |
| $M_{max,FEA}$ | Maximum moment obtained from finite element analysis |
| $M_E$ | Moment contribution of the elastomeric components |
| $M_{E,j}$ | Moment contribution of the j-th elastomer |
| $m$ | Number of elastomers in a single layer |
| $n$ | Number of layers in the device |
| $x_{E,j}$ | Radial distance of the j-th elastomer from the center of the device |
| $\theta$ | Rotation angle of the device |
| $k_E$ | Shear stiffness of the elastomer |
| $y_{E,j}$ | Tangential displacement of the j-th elastomer |
| $M_{dev}$ | Total moment capacity of the seismic device |
| $T_F$ | Total pretension force applied to the bolts |
| $f_y$ | Yield strength of reinforcing steel |

# LIST OF ABBREVIATIONS

| | |
|---|---|
| AISC | American Institute of Steel Construction |
| ASTM | American Society for Testing and Materials |
| BCH | Bilinear Kinematic Hardening |
| FE | Finite Element |
| FEA | Finite Element Analysis |
| FEM | Finite Element Method |
| MISO | Multilinear Isotropic Hardening |
| MKIN | Multilinear Kinematic Hardening |
| MW | Menétrey–Willam |
| RC | Reinforced Concrete |

# LIST OF FIGURES

**Figure 1.1** The exploded views of fuse-type mechanical couplers (FTMCs) without and with jacket [4] ..... 3

**Figure 1.2** Schematic illustration of the FTMC system [4] ..... 4

**Figure 1.3** Scheme of BCC connection types [5] ..... 5

**Figure 1.4** Schematic configuration of the proposed beam–column connection systems with energy-dissipating components: (a) JD1 connection detail and (b) JD2 connection detail [6] ..... 6

**Figure 1.5** Dissipative fuse Sismocell device [7] ..... 7

**Figure 1.6** Configuration of the FUSEIS system within a building frame [8] ..... 8

**Figure 1.7** Replaceable slit plate fuse elements with different slit geometries [9] ..... 9

**Figure 1.8** Representative geometries of shear-type structural fuse elements [14] ..... 10

**Figure 1.9** Schematic illustrations of the Pin-Fuse Joint, Pin-Fuse Frame, and Link-Fuse Joint seismic energy dissipation systems proposed [16] . 11

**Figure 1.10** Finite element model of the replaceable fuse steel–concrete composite connection [24] ..... 13

**Figure 1.11** Hybrid damper-linked steel frame (HDSF) system with MFHD and SRC fuse elements [25] ..... 14

**Figure 1.12** Replaceable shear fuse (RSF) beam-to-column connection [26] ..... 15

**Figure 2.1** General view of the seismic connection device [28] ..... 22

**Figure 2.2** Main components of the seismic connection device [28] ..... 23

**Figure 2.3** Load transfer mechanism occurring in the seismic connection device under rotational action [28] ..... 25

**Figure 3.1** Piecewise approximation of a function used in the FEM [31] ..... 27

**Figure 3.2** Link, Plane and Shell Type Elements in Ansys [33] ..... 29

**Figure 3.3** SOLID Type Element in Ansys [33] ..... 31

**Figure 4.1** Cross-sectional properties, loading configuration, and boundary conditions of Beam A1 ..... 35

**Figure 4.2** Finite element discretization of the beam and illustration of the element types used for concrete and reinforcement. ..... 36

**Figure 4.3** The constitutive model for concrete ..... 37

**Figure 4.4** Comparison between the load–midspan deflection curves obtained from the finite element analysis in this study and the experimental results ..... 38

**Figure 5.1** Idealized half-span beam model based on the moment distribution under lateral loading..... 39

**Figure 5.2** Geometric properties, reinforcement detailing, boundary conditions, and mesh structure of the reference RC beam (units:mm)..... 41

**Figure 5.3** Geometry of the connection device and finite element model..... 42

**Figure 5.4** Detailed dimensions of the friction and elastomeric components on the outer plate and the hole arrangement of the first inner plate ..... 42

**Figure 5.5** Finite element representation of the RC beam integrated with the seismic connection device, including the component configuration and mesh discretization..... 44

**Figure 5.6** Embedment length of the longitudinal plate ($L_{long}$)of the connection device within the RC beam ..... 44

**Figure 5.7** Material constitutive relationships used in the numerical model: (a) bolts, (b) steel components, and (c) elastomeric material (experimental data and Yeoh hyperelastic curve fitting). ..... 46

**Figure 5.8** Mesh Details of the model ..... 47

**Figure 6.1** Global moment–rotation hysteresis response of T600-F40-1Ls..... 56

**Figure 6.2** Global moment–rotation hysteresis response of T900-F40-1Ls..... 57

**Figure 6.3** Global moment–rotation hysteresis response of T900-F40-1L ..... 57

**Figure 6.4** Global moment–rotation hysteresis response of T1100-F40-1L ..... 57

**Figure 6.5** Global moment–rotation hysteresis response of T1100-F40-3L. ..... 58

**Figure 6.6** Global moment–rotation hysteresis response of T1440-F30-3L. ..... 58

**Figure 6.7** Global moment–rotation hysteresis response of T900-F50-3L ..... 58

**Figure 6.8** Cumulative energy dissipation capacities of the analyzed models ... 61

**Figure 6.9** The equivalent plastic strain distributions of the reference RC beam: (a) RC beam (-0.5 rad); (b) RC beam (0.71 rad)..... 62

**Figure 6.10** The equivalent plastic strain distributions of the T600-F40-1Ls model: (a) T600-F40-1Ls (-0.75 rad); (b) T600-F40-1Ls (end) ..... 63

**Figure 6.11** The equivalent plastic strain distributions of the T900-F40-1Ls model: (a) T900-F40-1Ls (-0.375 rad); (b) T900-F40-1Ls (-0.48 rad)..... 63

**Figure 6.12** The equivalent plastic strain distributions of the T900-F40-1L model: (a) T900-F40-1L (-0.50 rad); (b) T900-F40-1L (end) ..... 63

**Figure 6.13** The equivalent plastic strain distributions of the T1100-F40-1L model: (a) T1100-F40-1L (-0.50 rad); (b) T1100-F40-1L (1.50 rad) ..... 64

**Figure 6.14** The equivalent plastic strain distributions of the T1100-F40-3L model: (a) T1100-F40-3L (-0.50 rad); (b) T1100-F40-3L (end) ..... 64

**Figure 6.15** The equivalent plastic strain distributions of the T1440-F30-3L model: (a) T1440-F30-3L (-0.50 rad); (b) T1440-F30-3L (end) ..... 64

**Figure 6.16** The equivalent plastic strain distributions of the T900-F50-3L model: (a) T900-F50-3L (-0.50 rad); (b) T900-F50-3L (end) ..... 65

**Figure 6.17** The frictional forces developed within the individual friction members ..... 68

**Figure 6.18** Force transfer response of elastomeric pads ..... 71

**Figure A.1** General view of Model 1 and the placement of longitudinal steel plates within the reinforced concrete beam: (a) general model view, (b) placement of embedded longitudinal plates..... 91

**Figure A.2** Finite element representation of Model 1 and the longitudinal plate configurations adopted in Models 2 and 3. ..... 92

**Figure A.3** Moment–rotation responses of the reference beam and Models 1-3 . 93

**Figure A.4** Dissipated energy values of the reference beam and Models 1–3..... 94

**Figure A.5** Equivalent plastic strain distributions of the reference beam and Models 1– 3..... 95

# LIST OF TABLES

**Table 1.1** Comparison of Connection-to-Beam Capacity Ratios Reported in the Literature ..... 16

**Table 4.1** Concrete material properties defined according to the Menétrey –Willam model ..... 37

**Table 5.1** Material constants determined for the third-order Yeoh hyperelastic model [28] ..... 47

**Table 5.2** Finite Element Model Configurations and Defining Properties ..... 53

**Table 6.1** Comparison of theoretical and finite element moment capacities of the analyzed models ..... 60

# ABSTRACT

## Finite Element Analysis of Reinforced Concrete Beams Incorporating a Frictional and Elastomeric Seismic Energy Dissipation Device

Lal OĞUZ

Department of Civil Engineering
Master of Science Thesis

Supervisor: Asst. Prof. Dr. Orkun YILMAZ

In conventional seismic design, reinforced concrete (RC) systems are designed to dissipate energy through plastic hinging. However, this approach may lead to significant and often irreparable damage in load-bearing members under severe seismic effects. In recent years, low-damage design approaches have gained prominence by concentrating inelastic deformation demands in dedicated energy-dissipating components rather than in the primary structural system. In this study, a friction-based and elastomeric seismic device originally developed for steel structures is numerically integrated into an RC beam to control structural damage.

Within the scope of the study, a three-dimensional nonlinear finite element model was first validated using experimental data from the literature. Subsequently, utilizing the validated modeling approach, the behavior of the reference RC beam and the device-integrated beam models under reversed cyclic loading was evaluated. The parametric investigation considered the variables of friction

coefficient, bolt pretension force, number of embedded longitudinal plates, and embedment length.

The obtained results showed that the proposed device can significantly enhance the cyclic behavior and energy dissipation capacity of the RC beam. While the reference beam exhibited failure at a drift ratio of approximately 0.71%, the device-integrated models maintained stable hysteretic response up to a drift ratio of 1.5%. Furthermore, the cumulative energy dissipation capacity, which was 2.77 kNm for the reference model, was determined to reach approximately 17.5 kNm in the best-performing device-equipped models. However, in short single-plate embedment details, strain concentrations and early concrete damage were observed at the plate termination regions, whereas configurations incorporating multiple plates provided more stable behavior by distributing the damage over a wider area.

The findings obtained from this study reveal that the embedded connection details hold decisive significance and that the proposed design strategy constitutes a promising option for hybrid RC systems.

**Keywords:** Reinforced concrete (RC) beam, seismic device, frictional energy dissipation, elastomeric energy dissipation, finite element analysis.

# ÖZET

## Sürtünmeli ve Elastomerli Sismik Enerji Sönümleme Cihazı İçeren Betonarme Kirişlerin Sonlu Elemanlar Analizi

Lal OĞUZ

İnşaat Mühendisliği Anabilim Dalı
Yüksek Lisans Tezi

Danışman: Dr. Öğretim Üyesi Orkun YILMAZ

Geleneksel sismik tasarımda betonarme sistemler, enerjiyi plastik mafsallaşma yoluyla sönümleyecek şekilde tasarlanır. Ancak bu yaklaşım, şiddetli deprem etkileri altında taşıyıcı elemanlarda önemli ve çoğu zaman onarımı güç hasarlara neden olabilmektedir. Bu nedenle son yıllarda, doğrusal olmayan şekil değiştirme taleplerinin ana taşıyıcı sistemden uzaklaştırılarak özel enerji sönümleyici bileşenlerde toplanmasını hedefleyen düşük hasarlı tasarım yaklaşımları ön plana çıkmıştır. Bu çalışmada, yapısal hasarı kontrol altına almak amacıyla başlangıçta çelik yapılar için geliştirilmiş olan sürtünmeli ve elastomerik bir sismik cihaz, betonarme bir kiriş içerisine sayısal olarak entegre edilmiş ve incelenmiştir.

Çalışma kapsamında, öncelikle üç boyutlu doğrusal olmayan sonlu eleman modeli literatürdeki deneysel veriler kullanılarak doğrulanmıştır. Ardından doğrulanan modelleme yaklaşımı ile referans betonarme kiriş ve cihaz entegreli kiriş modellerinin tersinir çevrimsel yükler altındaki davranışı değerlendirilmiştir.

Parametrik incelemede sürtünme katsayısı, bulon öngerme kuvveti, gömülü boyuna levha sayısı ve gömme boyu değişkenleri dikkate alınmıştır.

Elde edilen sonuçlar, önerilen cihazın betonarme kirişin çevrimsel davranışını ve enerji sönümleme kapasitesini önemli ölçüde iyileştirebildiğini göstermiştir. Referans kiriş yaklaşık %0,71 ötelenme oranında göçme davranışı sergilerken, cihaz entegreli modeller %1,5 ötelenme oranına kadar kararlı histeretik tepki gösterebilmiştir. Ayrıca referans modelde 2,77 kNm olan kümülatif enerji sönümleme kapasitesinin, en iyi performans gösteren cihazlı modellerde yaklaşık 17,5 kNm'ye ulaştığı belirlenmiştir. Bununla birlikte, kısa tek levhalı gömme detaylarında levha bitim bölgesinde şekil değiştirme yığılmaları ve erken beton hasarı gözlenirken, çoklu levha içeren konfigürasyonların hasarı daha geniş bir bölgeye yayarak daha kararlı bir davranış sağladığı görülmüştür.

Bu çalışmadan elde edilen sonuçlar, gömülü bağlantı noktalarının belirleyici bir öneme sahip olduğunu ve önerilen tasarım stratejisinin hibrit betonarme sistemler için ümit vadeden bir seçenek olduğunu ortaya koymaktadır.

**Anahtar Kelimeler**: Betonarme kiriş, sismik cihaz, sürtünmeli enerji sönümlemesi, elastomerik enerji sönümlemesi, sonlu eleman analizi.

# 1
# INTRODUCTION

## 1.1 Seismic Damage and Energy Dissipation in Reinforced Concrete Structures

Since the earliest stages of civilization, humanity has sought to construct durable structures in order to ensure the safety of life and property against the destructive effects of natural disasters. As societies developed, structural systems evolved beyond merely satisfying basic sheltering needs and became one of the fundamental components of social, economic, and technological development. Over time, construction materials and structural systems advanced significantly, and reinforced concrete (RC) structures became widely used throughout the world due to their strength, durability, and economic advantages.

Nevertheless, RC structures are highly susceptible to significant damage under seismic loading. During strong ground motions, RC systems are required to dissipate a substantial portion of earthquake-induced energy through nonlinear deformation mechanisms.

RC structures primarily achieve their energy dissipation capacity under earthquake loading through ductile behavior and the formation of plastic hinges. However, in conventional force-based seismic design approaches, the dissipation of seismic energy through nonlinear deformations occurring in structural members inevitably results in structural damage. In this context, Priestley et al. [1] stated that plastic deformations occurring particularly in critical regions such as beam-column joints lead to concrete crushing, permanent strains in reinforcement, and significant residual drifts in structures. Although this approach satisfies life-safety objectives, the resulting damage significantly increases post-earthquake repair costs and limits the reusability performance of structures. Similarly, Bertero [2] emphasized that

while ductility is a fundamental requirement for seismic energy dissipation, irreversible damage and stiffness degradation occurring under cyclic loading adversely affect the post-earthquake serviceability performance of structures.

The structural damage, residual deformations, and high repair demands resulting from the conventional approach of dissipating seismic energy directly within primary structural members have increased interest in alternative energy dissipation strategies in recent years. Within this context, systems in which seismic energy is dissipated through specially designed energy-dissipating components rather than the primary structural system have gained increasing attention. Vargas and Bruneau [3] theoretically demonstrated that structural fuse systems can concentrate nonlinear behavior within sacrificial components, thereby enabling the primary structural members to remain within the elastic range. Through this approach, seismic energy is mainly dissipated by the damping elements acting as structural fuses, while potential structural damage in the main system is significantly limited.

Accordingly, in modern seismic design approaches, providing energy dissipation capacity through independent, controllable, and replaceable systems has become an important area of research. In particular structural fuse systems, friction-based dampers, and hybrid mechanisms with self-centering capability offer promising solutions for limiting post-earthquake damage, reducing residual drifts, and maintaining structural serviceability. Among these systems, fuse-type energy dissipation mechanisms have attracted considerable attention due to their ability to concentrate on damage within predefined sacrificial components while preserving the integrity of the primary structural system. Consequently, a significant portion of recent studies has focused on dissipating seismic energy through such specially designed energy-dissipating components rather than through the primary load-carrying system. Based on this approach, different fuse-type energy dissipation systems developed for reinforced concrete structures are reviewed in the following section.

## 1.2 Fuse-Type Energy Dissipation Systems in Reinforced Concrete Structures

RC structures developed with fuse-type energy dissipation systems aim to concentrate the damage occurring under earthquake effects in pre-designed components rather than in the main load-bearing members. Within this approach, inelastic behavior is intentionally directed toward specific elements, allowing damage to be confined to designated regions while preserving the integrity of the primary structural system. Accordingly, various systems have been proposed to achieve low-damage behavior in RC applications. These systems are generally designed to dissipate seismic energy through controlled deformation mechanisms, thereby reducing damage in critical structural members and improving overall seismic performance.

For instance, Soydan et al. [4] proposed a connection system for precast RC beam–column connections incorporating fuse-type mechanical couplers (FTMC). In this system, it was stated that the seismic energy is dissipated through controlled plastic deformations occurring in the couplers, instead of forming plastic hinges in the beam.

As shown in Figure 1.1, the FTMC elements consist of five main components, namely fuse element, main coupler, steel mace, mace nut and fastener nut. In the jacketed version (J-FTMC), a steel jacket is additionally used in order to prevent buckling of the fuse element and to improve its resistance under high compressive forces.

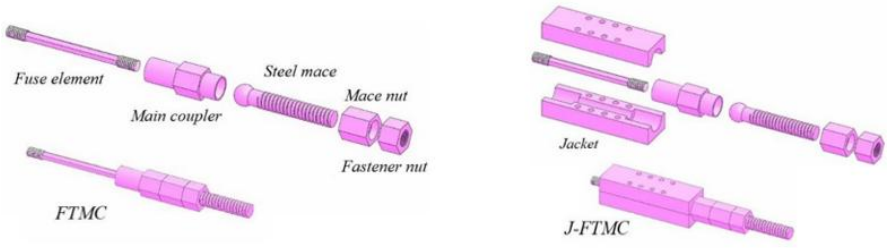



**Figure 1.1** The exploded views of fuse-type mechanical couplers (FTMCs) without and with jacket [4]

The proposed connection system is illustrated in Figure 1.2. The system consists of a steel hinge formed by connecting steel plates through a bolt together with the FTMC devices. These FTMC elements are positioned at the top and bottom

reinforcement levels of the beam. It was stated that moment transfer is provided through these elements, while the shear force is resisted by the steel hinge located at the connection. The system transforms beam moment into an axial force couple and transfers the entire flexural demand through the FTMC devices. In this way, plastic deformation is mainly concentrated in the fuse elements.

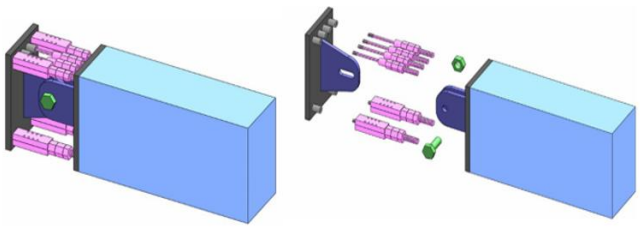


**Figure 1.2** Schematic illustration of the FTMC system [4]

Within the scope of the experimental study, five half-scale precast beam specimens with three different FTMC configurations were subjected to cyclic loading at drift levels ranging from 0.25% to 5%. The results showed that the strength and stiffness of the connection system are directly dependent on the number of FTMC devices. In the best-performing configuration, strength values of approximately 60–63 kN and energy dissipation capacities of 7–9.5 kNm were obtained.

Damage observations indicated that the damage was largely concentrated in the FTMC fuse elements, while it remained limited in the RC beam members. According to the criteria of ACI 374.1-05, it was observed that the successful configurations satisfied all performance requirements.

As a result of the experimental and numerical analyses, it was determined that the system exhibits stable hysteretic behavior, possesses high energy dissipation capacity, and provides satisfactory performance up to approximately 4% drift levels.

In addition to such fuse-type mechanical coupler systems, alternative approaches based on different energy dissipation mechanisms have also been proposed in the literature. In this context Colajanni et al. [5] investigated hybrid connection systems incorporating friction-based energy dissipation devices for RC beam–column joints. In these systems, seismic energy is dissipated through a controlled sliding mechanism provided by friction interfaces formed by steel plates and pretensioned

bolts located within the joint region. This approach aims to concentrate inelastic demand within the connection zone and to protect the primary structural members.

As shown in Figure 1.3, the developed connection types consist of three different BCC models with distinct performance characteristics. The BCC-1 (device with crossed-slotted holes) includes crossed-slotted plates at the lower part and a pin at the top and exhibits limited energy dissipation capacity. In the BCC-2 (curved-slotted hole system), a T-stub steel component is introduced in the joint region, which absorbs seismic energy and undergoes controlled plastic deformation, thereby protecting beam and column members and enabling a more stable rotational response. The BCC-3 (curved-slotted hole device combined with Perfobond connectors) represents an enhanced configuration, where Perfobond connectors extending into the concrete core provide a strong steel–concrete interlock. This results in increased connection stiffness, improved load distribution, and more stable hysteretic behavior. The results indicate that the BCC-3 model provides higher and more stable energy dissipation capacity and more effectively limits damage in beam–column members compared to the other configurations.

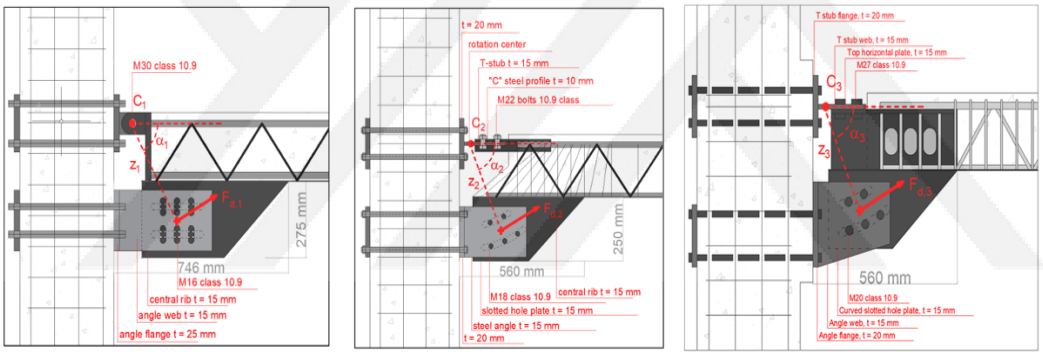



**Figure 1.3** Scheme of BCC connection types [5]

Similarly, Qu et al. [6] proposed two different connection designs with high energy dissipation capacity to improve the seismic performance of precast prestressed RC frames, and the effects of these systems on seismic behavior were investigated.

As shown in Figure 1.4(a), in the JD1 system, the energy-dissipating bars are positioned at the top and bottom regions of the beam and arranged to pass through the column to ensure continuity. In this system, the energy dissipation mechanism takes place within the joint region.

As shown in Figure 1.4(b), in the JD2 system, the energy-dissipating bars located within the joint region were removed, and the energy dissipation mechanism was shifted outside the joint and provided by external dissipating devices positioned at the beam ends. The external dissipating system consists of a fuse bar together with a restraint mechanism composed of filling material and a confining steel tube.

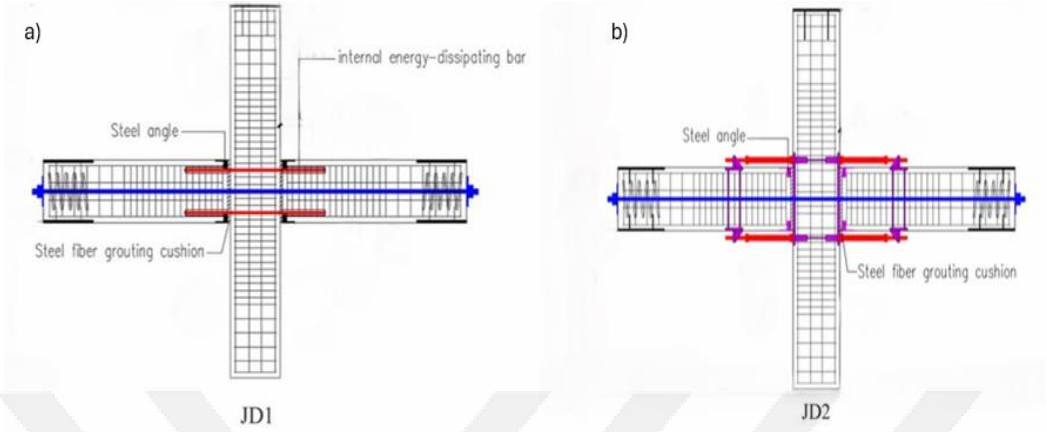



**Figure 1.4** Schematic configuration of the proposed beam–column connection systems with energy-dissipating components: (a) JD1 connection detail and (b) JD2 connection detail [6]

The experimental studies were carried out under a low-cycle reversed loading protocol. In these systems, self-centering behavior is provided by the pretension tendons, while the energy dissipation capacity is achieved through steel dissipating elements. According to the findings, although the JD1 system provides higher energy dissipation capacity, the JD2 system demonstrates superior performance in terms of lower residual deformation, higher initial stiffness, and concentration of damage in replaceable elements. It was observed that residual deformations remained at lower levels in the JD2 system, whereas they were more pronounced in the JD1 system. In addition, both systems achieved ductility factors greater than 3.0 and exhibited stable hysteretic behavior. It was emphasized that external dissipating elements offer advantages in terms of post-earthquake reparability.

Using nonlinear analyses, Sondaa and Pollini [7] showed that fuse-type Sismocell devices used in existing precast RC structures can significantly limit the force transmitted from roof diaphragms to columns, thereby reducing column base moments by approximately 30–69%. (see Figure 1.5). This force-limitation mechanism reduces demand concentration at the column base, limits damage in

joint regions and plastic hinges and supports a damage-control approach that enhances seismic resilience and post-earthquake reparability.

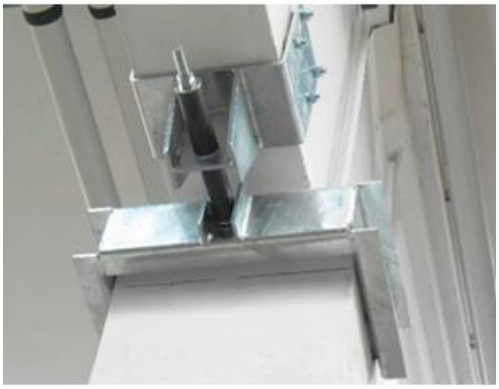


**Figure 1.5** Dissipative fuse Sismocell device [7]

Overall, the reviewed studies demonstrate that fuse-type energy dissipation systems provide an effective approach for RC structural systems by concentrating damage in fuse elements rather than in primary load-bearing members in order to enhance seismic performance. The findings reported in the literature indicate that these systems can provide stable hysteretic behavior, high energy dissipation capacity, reduced residual deformations, and improved post-earthquake reparability. The use of these dissipative elements enables damage to be concentrated in accessible regions, thereby limiting permanent damage in beam–column joints and critical structural members. In addition, experimental and numerical studies have shown that fuse-based connection systems improve structural behavior in terms of ductility and damage control under cyclic loading conditions. Therefore, fuse-type seismic protection systems have emerged as a promising approach for the development of resilient RC structures with enhanced seismic safety and rapid post-earthquake recovery potential.

## 1.3 Fuse-Type Energy Dissipation Systems in Steel Structures

Steel structures have become an important area of research in controlling seismic effects due to their high ductility capacity and energy absorption performance. In this context, fuse-type energy dissipation systems aim to prevent the dispersion of seismic damage throughout the structure by concentrating it in predefined and easily replaceable elements. Based on this approach, the structural fuse concept utilizes steel yielding fuses specially designed components that dissipate energy by

exhibiting controlled yielding behavior during earthquakes. Through this mechanism, the primary load-carrying system is intended to remain within the elastic range. In the literature, steel yielding fuse systems developed for steel structures provide significant advantages by enabling controlled damage and facilitating rapid post-earthquake repair, and they have laid the foundation for adapting energy dissipation concepts to RC systems.

One of the notable applications of the structural fuse concept in steel structures was proposed by Dougka et al. [8], who developed the FUSEIS system, an innovative energy dissipation system consisting of short steel beams connected between two closely spaced strong columns. As illustrated in Figure 1.6, these short beams are not the primary floor beams of the building but are located within a specially added FUSEIS frame integrated into the structure. The system generally exhibits shear wall-like behavior, while seismic energy dissipation and damage are intentionally concentrated in these short steel beams acting as fuse elements during earthquakes. These short beams are not designed to carry gravity loads, but rather to dissipate seismic energy through controlled plastic deformation under seismic actions. Experimental studies demonstrated that plastic deformation occurred only in the fuse beams, while the columns remained elastic. In addition, the system was reported to provide high ductility, stable hysteretic behavior, and easy post-earthquake repair and replaceability.

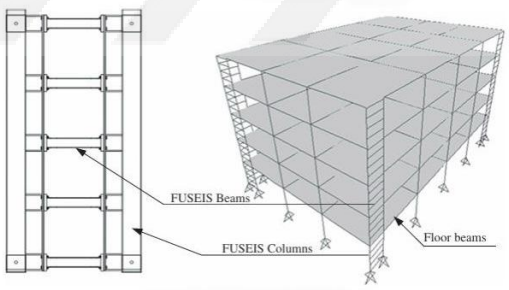



**Figure 1.6** Configuration of the FUSEIS system within a building frame [8]

Similarly, Pratap and Vesmawala [9] investigated the use of replaceable slit plate fuse elements in moment-resisting frames through experimental and numerical studies. In their work, three different replaceable slit damper fuse configurations, namely single oval, dual oval, and single elliptical slit dampers, were proposed and evaluated in terms of seismic performance, as illustrated in Figure 1.7. The results showed that, under seismic loading, damage was confined only to the fuse elements,

while the main structural components such as beams and columns remained in the elastic range.

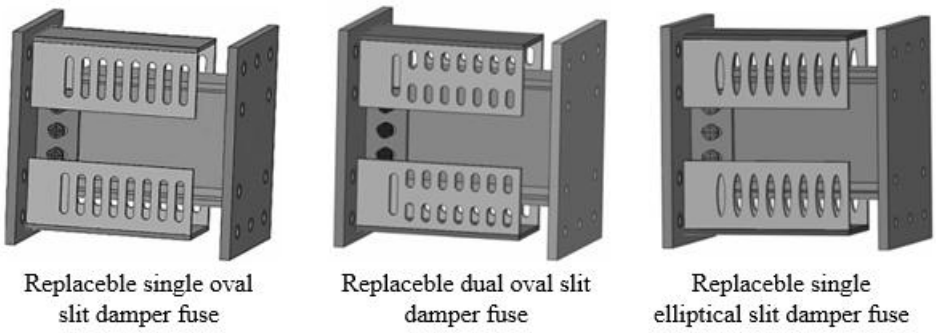



**Figure 1.7** Replaceable slit plate fuse elements with different slit geometries [9]

In another study, Nguyen and Eatherton [10] investigated the behavior of shear-type structural fuse elements used in steel structural systems and proposed optimized geometries that enhance buckling resistance and promote stable yielding behavior. The proposed fuse elements were validated through experimental and numerical analyses, demonstrating high ductility, stable hysteretic response, and effective energy dissipation capacity. Similar approaches have also been adopted for the development of replaceable fuse elements with different geometric configurations. Following these studies, Farzampour [11] proposed butterfly-shaped geometries for shear-type structural fuse elements and investigated the effect of geometry on the yielding behavior, showing that these fuse elements provide higher energy dissipation and more stable behavior. In another geometry optimization-based study, Avecillas and Eatherton [12] investigated the behavior of shear-type steel fuse elements against premature buckling and developed new fuse geometries using topology optimization methods to improve buckling resistance. The results showed that the optimized geometries delayed buckling and provided more stable hysteretic behavior. Similarly, Goshtaei et al. [13] evaluated the cyclic behavior of steel plate fuse elements using a multi-objective optimization approach and investigated the effects of geometric parameters on energy dissipation, ductility, and stiffness. The results demonstrated that appropriate geometric proportions play a significant role in fuse performance.

Expanding on these studies, Eatherton and Nguyen [14] comprehensively investigated different geometric forms of shear-type structural fuse elements and compared the behavior of butterfly-shaped, hourglass-shaped, elliptical-hole,

buckling-resistant optimized, and tied-butterfly fuse geometries, as illustrated in Figure 1.8. Through experimental and numerical investigations, the study demonstrated that fuse geometry has a significant influence on structural stiffness, strength, ductility, buckling resistance, and energy dissipation capacity. The results further indicated that each geometry exhibits distinct mechanical characteristics, making different fuse configurations suitable for different seismic performance objectives.

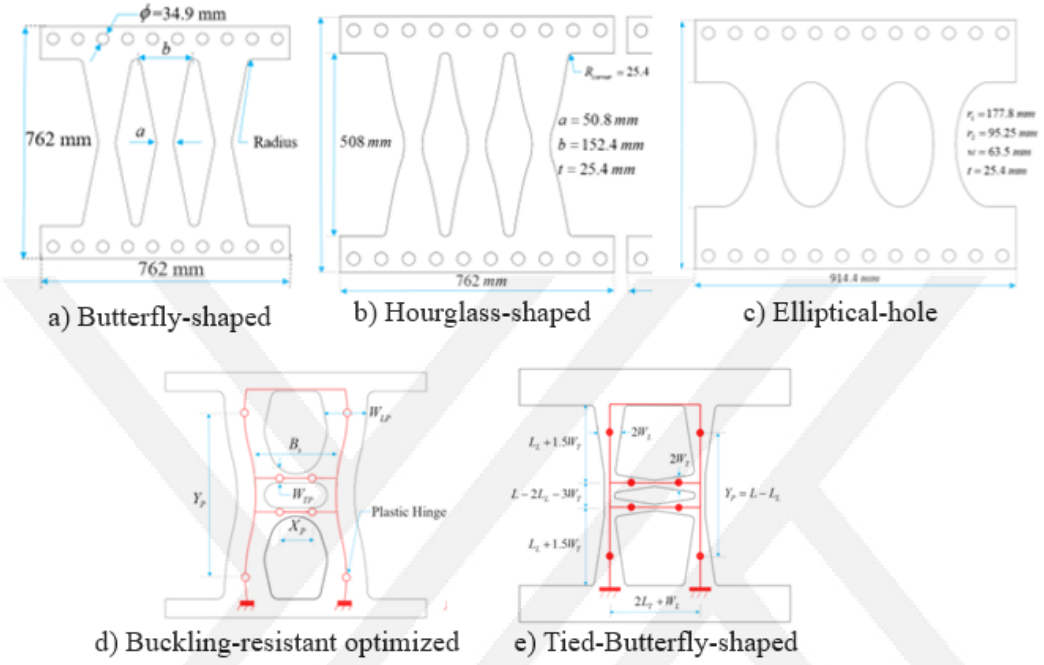



**Figure 1.8** Representative geometries of shear-type structural fuse elements [14]

In addition, Ferraioli et al. [15] investigated the lateral torsional buckling behavior of dumbbell-shaped steel strip dampers under cyclic loading and examined the effects of geometric parameters on buckling initiation, plastic strain distribution, and strength degradation. The study also proposed design equations defining critical slenderness limits to prevent buckling-induced strength degradation.

The successful results obtained in steel structures have demonstrated that the fuse-type energy dissipation approach can also be adapted to different structural materials. However, the tendency of RC systems to exhibit brittle behavior and the complex stress state of joint regions limit the direct application of this approach. Therefore, recent studies have focused on adapting the fuse concept used in steel structures to RC connections and developing new connection details capable of providing controlled energy dissipation.

## 1.4 Steel Friction-Based Fuse Systems

Friction-based fuse systems have attracted significant attention in earthquake engineering due to their ability to dissipate seismic energy through controlled sliding mechanisms. Unlike conventional systems that rely on material yielding, these systems reduce structural damage by concentrating energy dissipation within replaceable fuse components. Owing to their stable hysteretic behavior, recentering capability, and reduced post-earthquake repair demand, friction-based fuse systems have been widely investigated for steel structures subjected to seismic loading.

In a related study to friction-based seismic energy dissipation systems, Sarkisian et al. [16] investigated friction-based fuse systems used in steel structures, particularly the Pin-Fuse Joint, Pin-Fuse Frame, and Link-Fuse Joint systems shown in Figure 1.9. The Pin-Fuse Joint was used in beam–column connections, the Pin-Fuse Frame in steel braced frames, and the Link-Fuse Joint in link elements to dissipate seismic energy through controlled sliding mechanisms during earthquakes. Experimental and numerical analyses demonstrated that these systems exhibited stable hysteretic behavior, improved energy dissipation capacity, and significantly reduced post-earthquake structural damage.

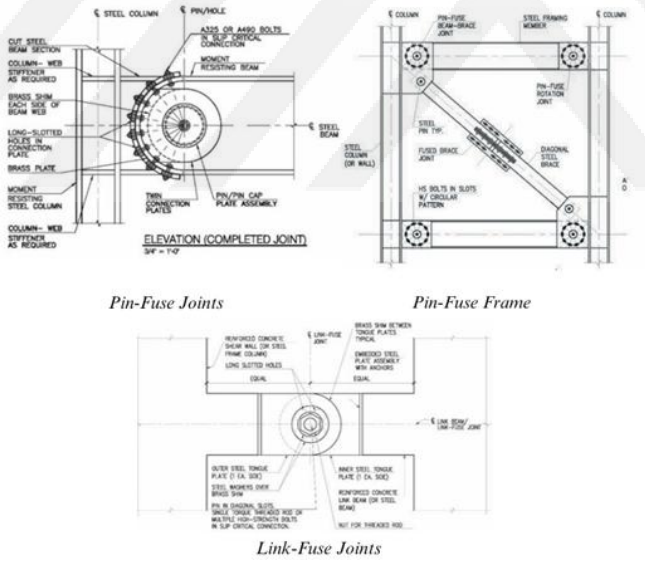



**Figure 1.9** Schematic illustrations of the Pin-Fuse Joint, Pin-Fuse Frame, and Link-Fuse Joint seismic energy dissipation systems proposed [16]

Latour et al. [17] experimentally investigated friction-damped beam-to-column connections using thermally sprayed aluminium friction plates. The proposed system provided stable hysteretic behavior and high energy dissipation capacity

while minimizing structural damage under cyclic loading. Another study by Cui et al. [18] experimentally investigated a slip friction device using symmetric friction connections (SFCs) with different shim materials and bolt tension levels. The results showed that the proposed device exhibited stable rectangular hysteretic behavior, low strength degradation, and effective seismic energy dissipation under cyclic loading. Similarly, Yang et al. [19] investigated rotational friction dampers (RFDs) using different friction materials and bolt configurations. Experimental results showed that fiber-reinforced composite friction materials and optimized bolt arrangements provided more stable hysteretic behavior and improved energy dissipation capacity. In another study focusing on friction-based seismic connections, Bozer et al. [20] developed an adjustable rotational friction-based connection system for seismic energy dissipation. The system dissipates energy through controlled friction generated by replaceable metallic discs clamped using a central bolt. In the study, steel, aluminum, and copper discs were experimentally investigated under cyclic loading with different bolt torque levels. The results showed that the system provided stable hysteretic behavior and high energy dissipation capacity. Steel discs exhibited the highest energy dissipation performance, while copper discs demonstrated the most stable cyclic behavior. In addition to the development of friction-based dampers, several studies also focused on factors affecting the long-term performance of these systems. In this context, Chan and Tang [21] investigated the effects of long-term serviceability conditions of friction dampers on seismic performance. The study experimentally and numerically demonstrated that corrosion and grease contamination significantly reduce the friction coefficient and energy dissipation capacity of the dampers. Lomiento et al. [22] developed an experimentally validated friction model for friction-based seismic isolators. The study demonstrated that vertical load, sliding velocity, and cycle repetition have significant effects on friction behavior and energy dissipation capacity. Subsequently, Shahbazi and Moaddab [23] developed a hybrid friction damper capable of operating under different earthquake intensity levels. In the proposed system, the auxiliary fuse is activated during low-intensity earthquakes, while the main fuse engages during severe earthquakes, thereby providing dual-level energy dissipation. Experimental and numerical results showed that the system exhibited stable hysteretic behavior, increased energy dissipation capacity, and reduced the probability of structural damage.

Friction-based fuse systems have been widely used in steel structures as effective energy dissipation devices in which seismic energy is dissipated through a controlled sliding mechanism. Various experimental and parametric studies have demonstrated that these systems provide stable hysteretic behavior, high energy dissipation capacity, and easy post-earthquake replaceability. In addition, it has been reported that the friction coefficient and the level of bolt pretension significantly influence the overall system performance. In particular, their ability to provide low residual deformations through controlled sliding behavior and the applicability of friction-based energy dissipation mechanisms have encouraged the widespread use of these systems in the development of next-generation seismic connections and energy dissipation devices.

## 1.5 Hybrid and Replaceable Fuse Systems in Steel Frames

He et al. [24] developed a steel-concrete composite connection system incorporating replaceable angle fuse elements. As shown in Figure 1.10, the proposed system consists of a steel column, steel beam, concrete slab, connection plates, and replaceable angle fuse elements, forming a steel-concrete composite connection. In the proposed connection, seismic damage was intended to be concentrated in the replaceable angle elements located at the bottom flange.

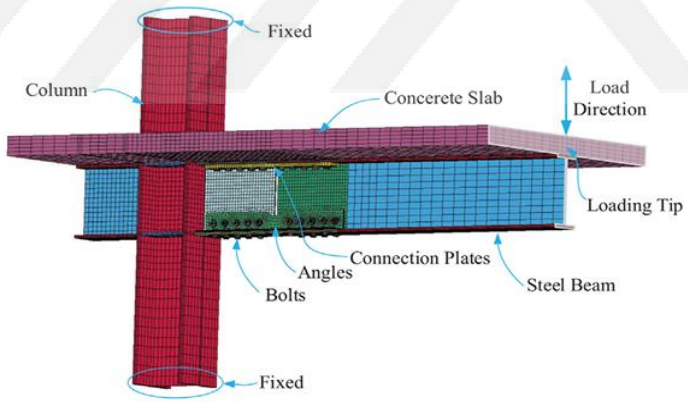



**Figure 1.10** Finite element model of the replaceable fuse steel–concrete composite connection [24]

Full-scale experimental tests and finite element analyses demonstrated that plastic deformations were concentrated in these fuse elements, while the main structural components remained largely within the elastic range. In addition, it was determined that the connection regained its initial strength and stiffness after the

damaged angles were replaced, while the concrete slab remained protected without significant damage throughout the loading process. Consequently, the study revealed that this hybrid mechanism provided an effective structural solution offering low-cost reparability and reliable damage control.

Subsequent studies have focused on developing hybrid fuse systems combining different energy dissipation mechanisms in order to improve seismic performance and damage control capacity. Zhai et al. [25] developed a hybrid damper-linked steel frame system incorporating both metallic and friction-based energy dissipation mechanisms for use under extremely severe earthquake effects. As shown in Figure 1.11, the proposed system includes two different fuse mechanisms. The first consists of metal-friction hybrid damper (MFHD) elements placed within the short link region between closely spaced columns. The MFHD system is based on the series interaction of metallic dampers and friction dampers. Under low-level earthquake effects, the metallic dampers dissipate energy through yielding, whereas under larger earthquake effects, the friction dampers are activated, providing dual-level energy dissipation behavior. The second fuse mechanism consists of semi-rigid connection (SRC) elements located at the beam-to-column connection region. Under severe earthquake effects, these connection elements also exhibit yielding behavior and provide additional energy dissipation. Thus, the proposed system combines a hybrid damper mechanism in the linked-column region with replaceable semi-rigid fuse elements at the beam-column connections.

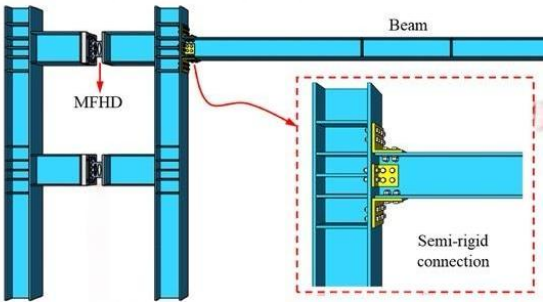



**Figure 1.11** Hybrid damper-linked steel frame (HDSF) system with MFHD and SRC fuse elements [25]

In another study focusing on replaceable fuse-based structural systems, Richards [26] developed a replaceable shear fuse (RSF) connection system for earthquake-resistant steel moment frames and investigated its performance through full-scale experimental tests. As shown in Figure 1.12, the proposed connection consists of a

steel column, steel beam, top connection plates, a shear tab, and a replaceable fuse plate bolted to the bottom flange of the beam. The fuse plate was designed to dissipate seismic energy through shear yielding under severe earthquake loading, thereby protecting the beam and column elements. Within the scope of the study, two full-scale tests were conducted, and in the second test, the damaged fuse plate from the first test was replaced to evaluate the post-earthquake reparability of the system. Experimental results showed that plastic deformations were largely concentrated in the fuse plate, while no significant damage occurred in the main structural components. Furthermore, after replacement of the fuse plate, the connection was able to be reused while maintaining sufficient stiffness and strength. The moment at the column face was reported in normalized form with respect to the nominal plastic moment of the beam ($M_p$), and a resistance of approximately 1.0-1.1$M_p$ was sustained by both specimens without strength degradation prior to tearing of the fuse plate.

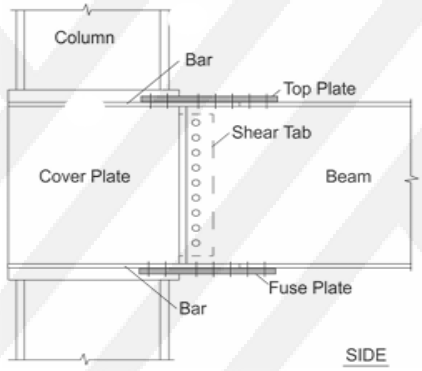



**Figure 1.12** Replaceable shear fuse (RSF) beam-to-column connection [26]

In another study, Tian et al. [27] investigated the design principles of steel beam-to-column connections incorporating replaceable buckling-restrained fuse plates. In the proposed system, energy-dissipating fuse plates were positioned inside the beam flanges and restrained against buckling using C-shaped shear tabs. In this way, the fuse plates were intended to dissipate seismic energy through yielding without experiencing buckling under earthquake loading. Low-yield-point LYP160 steel was adopted for the fuse plates. Parametric analyses performed using Abaqus demonstrated that the joint zone strength, beam height, and fuse plate properties were the primary parameters governing the structural behavior. It was also reported that more than 90% of the energy dissipation was concentrated in the fuse plates for specimens with strong joint zones.

Although numerous energy-dissipating connection systems have been proposed in the literature, only a limited number of studies explicitly report the relationship between the moment capacity of the connection and that of the main beam. Since this relationship directly influences the intended damage distribution and the activation of the fuse mechanism, the reported connection-to-beam capacity ratios are summarized in Table 1.1.

**Table 1.1** Comparison of Connection-to-Beam Capacity Ratios Reported in the Literature

| Reference | Model | Reference quantity for the beam | Connection/Beam Capacity |
|---|---|---|---|
| Soydan et al. [4] | FTMC beam-end connection ([4B]2J, [2J]2J and [2J2B]2J configurations) | Yield moment capacity of the RC beam, $M_{y,beam}$ | 52% (positive), 52–55% (negative) |
| Colajanni et al. [5] | BCC-1, BCC-2 and BCC-3 | Design flexural resistance of the beam, $M_{Rd}$ | 66.70% |
| Pratap and Vesmawala [9] | Beam-column connection with Single Oval Slit Damper Fuse (SOSDF), Dual Oval Slit Damper Fuse (DOSDF), and Single Elliptical Slit Damper Fuse (SESDF) | $M_p$ = 38.66 kNm as reported in the study | $M_{max}/M_p$ = 154–184% |
| Tian et al. [27] | Steel beam-to-column connection with replaceable buckling-restrained fuse plates | Full-section plastic moment of the middle beam | 29–82% (baseline model 65%; recommended minimum $\alpha \geq 0.50$) |
| Latour et al. [17] | TSJ-SA300-320-CYC12 and TSJ-H-SA300-260-CYC13 friction-damped joints | Nominal plastic flexural resistance of the beam | 100% (TSJ); 140% at the column face and 85% at the unstrengthened beam segment (TSJ-H) |
| Richards [26] | Replaceable shear fuse (RSF) connection, Specimens 1 and 2 | Nominal plastic moment of the beam, $M_p$ | Approximately 100–110% |

Table 1.1 summarizes two main design philosophies identified in the reviewed studies. In the first approach, the connection capacity is intentionally limited to a value below that of the connected member. This strategy physically restricts the force transmitted to the primary structural element. In the second approach, the connection capacity is designed to be similar to or greater than the member capacity. In this case, protection of the primary member is achieved by shifting the inelastic mechanism away from the member, rather than by reducing the force transmitted through the connection.

Within the first group, Soydan et al. [4] designed the FTMC beam-end connection with a connection moment capacity corresponding to approximately 52-55% of the yield moment capacity of the reinforced concrete beam. This design strategy intentionally limits the connection capacity below that of the beam, ensuring that plastic deformations and seismic energy dissipation are concentrated within the replaceable FTMC fuse elements rather than the reinforced concrete beam. Similarly, Colajanni et al. [5] proposed the BCC-1, BCC-2, and BCC-3 friction-based connection systems with a connection-to-beam capacity ratio of approximately 66.7%. This ratio was calculated using the design moment of the connection ($M_d$ = 110 kNm) and the positive moment capacity of the hybrid steel-trussed concrete beam ($M_{Rd}$ = 165 kNm) reported in the study, and it follows directly from the overstrength factor of 1.5 adopted for the beam. Following the capacity design philosophy, the frictional connection was intentionally designed with a lower moment capacity than the beam so that seismic energy dissipation would occur within the replaceable connection components before significant damage developed in the primary structural members. A ratio of 75% was reported by the same authors for the column-base connection CBC-2 with respect to the flexural strength of the column. Likewise, Tian et al. [27] introduced a design bearing capacity factor ($\alpha$), defined as the ratio of the full-section plastic moment resistance of the weakened portion of the fuse plate to that of the unenlarged segment of the middle beam flange, which was varied between 0.29 and 0.82 across the parametric models. The lowest value was obtained for fuse plates made of low-yield-point steel proportioned according to the equal stiffness principle, and this configuration was characterized as excessive weakening because of the associated reduction in load-carrying capacity and the increased risk of fuse fracture at large

drift levels. A minimum value of $\alpha \geq 0.50$ was consequently recommended, whereas the baseline model corresponded to $\alpha = 0.65$.

Within the second group, Latour et al. [17] explicitly argued that the bending sliding resistance of the connection should not exceed the nominal flexural resistance of the connected beam but should nevertheless remain as close as possible to unity, so that the beam section is not underutilized under gravity and serviceability actions. Specimen TSJ-SA300-320-CYC12 was accordingly proportioned for a design moment of 133 kNm at the column face, equal to the nominal plastic resistance of the IPE270 beam. In specimen TSJ-H-SA300-260-CYC13, a welded haunch was introduced in order to increase the lever arm, and the design moment at the column face was raised to 187 kNm, corresponding to 1.4 times the nominal beam resistance. Owing to the haunch, the moment acting on the unstrengthened beam segment was reduced to approximately 113 kNm, which is about 85% of the nominal beam resistance, and the beam was therefore kept elastic despite the higher capacity of the connection. A similar outcome was reported by Richards [26], where the moment at the column face reached approximately 1.0-1.1$M_p$ while beam yielding was prevented in both specimens. In such systems, the higher ratio is partly imposed by qualification requirements, since AISC 341 requires a flexural resistance of at least 0.80$M_p$ at the column face at a story drift of 0.04 rad for special moment frame connections.

The study by Pratap and Vesmawala [9] requires particular attention, since the design intent and the reported response do not coincide. A coefficient of $\alpha = 0.5$ was adopted within the sizing equation of the slit dampers in order to ensure yielding of the dampers prior to the formation of a plastic hinge in the beam, and it therefore governs the proportioning of the damper plates rather than expressing the ratio between the connection and beam moment capacities. The reported peak moment capacities of the SOSDF, DOSDF and SESDF connections ranged from 1.54$M_p$ to 1.84$M_p$, and all three connections were classified as full-strength connections according to IS 800-2007, for which a resistance of 1.2$M_p$ is required. Since the derivation of the reference value $M_p$ = 38.66 kNm was not documented and the beam and column sections were stated inconsistently, these ratios should be interpreted with caution.

The reviewed studies therefore indicate that no single capacity ratio can be regarded as representative of energy-dissipating connections in general. The selection of the capacity ratio appears to be governed primarily by the deformation capacity of the protected member, by the extent to which the beam is required to be utilized under gravity and serviceability actions, and by the connection classification requirements of the applicable code. All connections applied to reinforced concrete or precast members fall within the lower band of approximately 50 to 67%, which is consistent with the limited and largely irreversible damage tolerance of concrete elements, in which cracking, crushing, and bond deterioration cannot be recovered after a seismic event. Steel applications, in contrast, are distributed across both bands. Ratios approaching or exceeding unity have been reported where the connection is required to satisfy full-strength classification criteria or where the beam section is intended to be fully exploited under service actions, whereas ratios comparable to those adopted for concrete members have been used where the fuse plate is proportioned according to a strong beam and weak fuse principle. The governing consideration is therefore the reparability of the protected member rather than its material alone.

The reviewed studies indicate that hybrid and replaceable fuse-based connection systems are effective in concentrating seismic damage within designated sacrificial elements, thereby limiting severe inelastic deformations in the primary structural members. The integration of hybrid energy dissipation mechanisms with replaceable fuse components has shown potential for improving seismic resilience, minimizing post-earthquake repair costs, and enhancing the reparability of structures. As a result, the development of hybrid beam-to-column connection systems that combine energy dissipation and replaceability remains a significant research focus for achieving low-damage and resilient structural systems under seismic loading.

Despite these promising developments, the majority of the existing studies have focused on steel structural systems and beam-to-column connection regions. Although replaceable fuse elements, friction dampers, and hybrid energy dissipation mechanisms have demonstrated successful performance in steel structures, their application to RC members remains limited. Existing studies on RC structures have primarily concentrated on connection-level solutions, externally

attached damping devices, or precast connection details. Consequently, the behavior of hybrid systems combining friction-based energy dissipation with elastomeric restoring mechanisms embedded within RC members has not yet been sufficiently investigated. Furthermore, the force-transfer mechanism between embedded steel components and the surrounding concrete, local stress concentrations, damage distribution, and the influence of embedment detailing on the overall structural response remain important research topics requiring further clarification.

## 1.6 Aim of the Thesis

Within the scope of this study, the applicability of a frictional and elastomeric seismic connection device, previously developed by Yılmaz [28] for steel moment-resisting frame systems, was investigated through its integration into a RC beam. In the proposed approach, instead of dissipating seismic energy directly through plastic hinge formation within the RC member, a significant portion of the energy dissipation was intended to occur within the embedded hybrid device. In this manner, it was aimed to reduce the deformation demand and local damage level imposed on the RC member. The proposed system is based on the combined action of a friction-based energy dissipation mechanism and elastomeric components. Bolt pretension forces were defined in order to activate the friction mechanism and to control the energy dissipation capacity of the system. In addition, the elastomeric components were intended to provide supplementary stiffness and restoring behavior to the structural response. Since the device was integrated within the RC member, the influence of the force-transfer mechanism between the internal steel components and the surrounding concrete was also taken into consideration.

The behavior of the proposed system was investigated by means of nonlinear finite element analyses performed using the Ansys Workbench 2024 R2 [29] software. In order to evaluate the accuracy of the numerical modeling approach, a validation study was first carried out by reproducing the response of an experimentally tested RC beam available in the literature. Subsequently, using the validated modeling methodology, the cyclic responses of the reference RC beam and the beams equipped with the device were compared. Within this scope, hysteretic behavior,

energy dissipation capacity, plastic strain distributions, damage progression, and force-transfer mechanisms within the internal components were evaluated in detail.

Furthermore, parametric analyses were conducted to determine the primary parameters affecting the behavior of the proposed system. In these analyses, the effects of the friction coefficient, bolt pretension force, and the number and embedment length of the embedded steel plates on the overall system performance were investigated. Thus, the behavior of the hybrid energy dissipation system integrated into the RC member was evaluated, and it was demonstrated that embedment detailing plays a critical role in the structural performance of the system.

## 1.7 Hypothesis

The present study hypothesizes that integrating a frictional and elastomeric seismic device into RC beam-to-column connections can significantly improve the seismic performance of RC members by transferring the inelastic demand from the concrete beam to the replaceable energy dissipation device. It is further hypothesized that the friction coefficient, bolt pretension force, and the embedment configuration of the longitudinal steel plates are the primary parameters governing the hysteretic response, energy dissipation capacity, and damage distribution of the system. Accordingly, an appropriate combination of these parameters is expected to provide stable hysteretic behavior, increase cumulative energy dissipation, and reduce strain localization within the surrounding concrete, thereby enhancing the damage-control performance of the RC beam under cyclic loading.

# 2
# FRICTIONAL AND ELASTOMERIC SEISMIC DEVICE

## 2.1 General Structure and Components of the Device

The frictional and elastomeric seismic connection device investigated in this study was initially developed by Yılmaz [28] focusing on high energy dissipative moment connections for seismic-resistant steel structures. The developed system was later patented by Yılmaz and Bekiroğlu [30] as a frictional and elastomeric seismic connection device particularly intended for use in buildings.

The device used is fundamentally a mechanical system consisting of steel plates, an elastomer layer, friction surfaces, and high-strength bolts. In this section, the components of the device are described in detail.

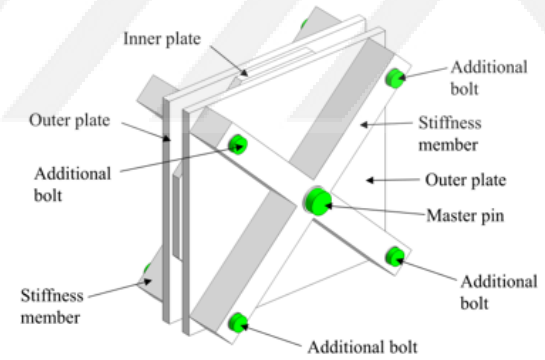



**Figure 2.1** General view of the seismic connection device [28]

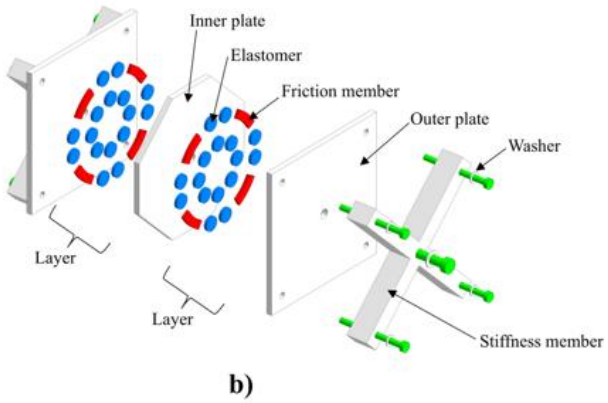



**Figure 2.2** Main components of the seismic connection device [28]

### 2.1.1 Steel Body Plates

The load-carrying framework of the device consists of steel plates. These plates form the regions where moment transfer occurs and friction forces develop.

#### 2.1.1.1 Outer Plate

The outer connection plates are positioned on the front and rear faces of the seismic connection device, with one plate on each side, resulting in a total of two plates. This configuration is illustrated in Figure 2.1.

#### 2.1.1.2 Inner Plate

The number of layers in the device is determined during the design stage depending on the targeted moment capacity and energy dissipation level. Since the number of layers directly affects the number of inner connection plates, the geometry is selected by considering that additional bolts must not come into contact with the plate during rotation. As shown in Figure 2.1, the device configuration includes a single central inner connection plate.

### 2.1.2 Master Pin

As shown in Figure 2.1, the master pin positioned at the exact center of the device is the fundamental component defining the system's axis of rotation and is used as a single unit. During assembly, a pretension force is applied to this bolt to ensure the operating conditions of the device.

### 2.1.3 Additional Bolts

Bolts are the main elements that hold the components of the device together and provide the pretension necessary for the friction mechanism to work. Therefore, bolts need to be selected with high strength, sufficient performance against fatigue effects, and low long-term capacity loss under pretension. Additional bolts are used to ensure that the total pretension force applied to the device is transferred more evenly to the surface of the outer connection plate. This way, the continuity of contact between the friction elements and the connection plates is maintained, supporting the stable operation of the friction mechanism. The number of additional bolts is determined based on the number of friction elements in each layer.

### 2.1.4 Stiffness Member

The stiffness member is used to limit bending deformations that may occur in the external connection plates due to pretension forces applied through bolts. This element contributes to the more stable transfer of the pretension force by increasing the out-of-plane stiffness of the external connection plate. The geometry of the support element can be modified according to design requirements to limit the bending deformations that may occur in the external connection plate.

### 2.1.5 Friction Members

The friction surfaces are the components of the device responsible for hysteretic energy dissipation and moment transfer. Their primary function is to generate high frictional resistance through the normal force produced by bolt pretension, dissipate energy during repeated sliding movements, and ensure the formation of hysteretic loops in the moment–rotation response.

The friction element is welded to the outer connection plate, and a friction-based energy dissipation mechanism develops at the contact interface between the friction element and the inner connection plate during sliding.

### 2.1.6 Elastomeric Element

The elastomer is made of rubber and forms an essential part of the device's moment-resisting mechanism. The elastomer resists deformation mainly through shear. During the rotational response of the connection, it generates an additional elastic moment. This moment increases with the shear stiffness of the elastomer.

Therefore, a stiffer elastomer also enhances the secant stiffness of the connection. Consequently, the elastomer thickness, shear stiffness, and shear modulus are critical design parameters in the device design. In Figure 2.2, a circular shape has been preferred for representation.

## 2.2 Calculation of the Moment-Carrying Capacity of the Seismic Connection Device

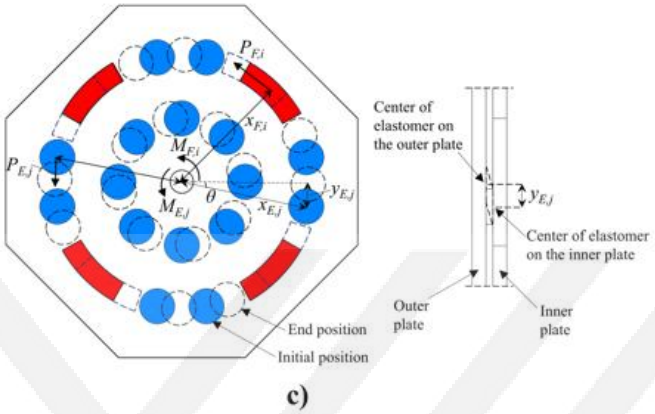



**Figure 2.3** Load transfer mechanism occurring in the seismic connection device under rotational action [28]

The load-carrying mechanism of the device under seismic action is defined by two primary components as it undergoes rotation. The first component is the sliding resistance developed in the friction elements, and the second is the shear forces generated within the elastomer layers. These two mechanisms produce moments about the center of the device and together constitute the total moment capacity.

The frictional moment $M_F$ generated by the friction elements is expressed as follows:

$$M_F = T_F \mu x_F \tag{2.1}$$

In this equation, $\mu$ denotes the friction coefficient of the sliding interface; $T_F$ represents the total pretension force applied to the main bolt and all additional bolts; and $x_F$ is the distance between the centroid of the friction element and the center of the device.

Elastomer components contribute to the development of moment resistance by deforming under shear effects. The rotational motion of the device is represented

by the rotation angle $\theta$. The lower surface of each elastomer layer is bonded to the rear plate, while the upper surface is bonded to the front plate. As the device rotates, these two plates slide relative to each other, resulting in a relative displacement denoted as $y_{E,j}$.

The shear stiffness of the elastomer, ($k_E$), is determined based on the shear modulus, cross-sectional area, and thickness of the elastomer as follows:

$$k_E = GA/h \tag{2.2}$$

where $G$ is the shear modulus of the elastomer, $A$ is the cross-sectional area of the elastomer, and $h$ is the elastomer thickness.

The total moment contribution of all elastomers within the device $M_E$ is expressed as follows:

$$M_E = \sum_{j=1}^{m} M_{E,j} = \sum_{j=1}^{m} \left( k_E y_{E,j} x_{E,j} \right) = \sum_{j=1}^{m} \left( k_E \theta x_{E,j}^2 \right) \tag{2.3}$$

In this equation; the number of elastomers in a single layer is denoted by $m$, the shear stiffness of the elastomer is $k_E$, the distance between the centroid of the elastomer and the geometric center of the device is expressed as $x_{E,j}$, and the moment value for each elastomer is represented by $M_{E,j}$. The tangential displacement of the elastomer is denoted by $y_{E,j}$, and this displacement is directly proportional to the rotation angle. Accordingly, the total moment-carrying capacity of the device, $M_{dev}$, is calculated by the equation given below.

$$M_{dev} = n \left[ T_F \mu x_F + \sum_{j=1}^{m} \left( k_E \theta x_{E,j}^2 \right) \right] \tag{2.4}$$

# 3
# GENERAL INFORMATION ON THE CONCEPTS DISCUSSED IN THE THESIS

## 3.1 Finite Element Method (FEM)

The Finite Element Method (FEM) is a powerful numerical analysis technique widely used in almost every field of mathematical physics and engineering. It has broad applications in structural mechanics, stress analysis, fluid mechanics, heat transfer, thermal insulation, wave propagation, static and dynamic elasticity, plasticity, impact problems, and seismic earthquake engineering.

FEM enables the analysis of structures with complex geometries and boundary conditions. In engineering applications, physical phenomena are generally represented by differential equations; however, these equations are often too complex to be solved using classical analytical methods. FEM overcomes this limitation by discretizing the continuum into a finite number of smaller subdomains called elements. The behavior of each element is mathematically formulated, and the overall structural response is obtained by assembling the contributions of all elements into a global system of equations [31].

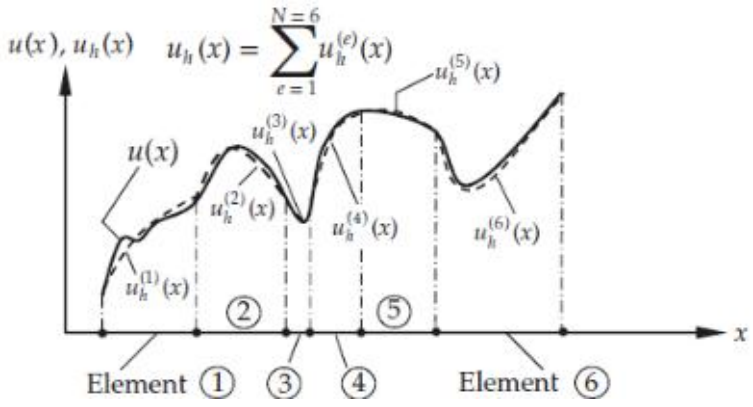



**Figure 3.1** Piecewise approximation of a function used in the FEM [31]

Figure 3.1 illustrates the approximate representation of a complex function by dividing it into smaller parts in the FEM. A continuous function, $u(X)$, is approximately expressed using simpler functions defined over different subregions. Each subregion represents a "finite element," while the combination of these elements forms the approximate solution of the entire system. The expression $u_h(x)$ shown in the figure represents the summation of the approximate solutions obtained on an element basis [31].

The finite element analysis procedure generally consists of eight fundamental steps [32].

Step 1: The structure to be analyzed is discretized into smaller elements connected through nodes, and appropriate element types are selected according to the problem. This process is called meshing, and the mesh density directly affects the accuracy of the solution.

Step 2: Shape functions are defined for each element to approximately represent the displacement field within the element.

Step 3: Strain–displacement and stress–strain relationships are established to mathematically describe the material behavior.

Step 4: Using these relationships, the stiffness matrices and element equations for each element are derived.

Step 5: The element contributions are assembled to form the global equation system of the structure, and appropriate boundary conditions and external loads are applied to the system. The general finite element equation can be expressed as:

$$[K]\{u\} = \{F\} \tag{3.1}$$

where $[K]$ represents the global stiffness matrix, $\{u\}$ denotes the unknown nodal displacement vector, and $\{F\}$ represents the external load vector.

Step 6: The global equation system is solved to determine the unknown degrees of freedom and nodal displacements.

Step 7: Element strains, stresses, and internal forces are calculated using the obtained displacements.

Step 8: The results are evaluated through deformation shapes, stress distributions, contour plots, and other graphical representations to interpret the structural behavior.

In the studies conducted within the scope of this thesis, the finite element analysis steps described above were carried out using computer-based finite element analysis software. In this study, Ansys Workbench finite element analysis software [29] was used for the analysis of three-dimensional solid models.

## 3.2 Finite Element Types in Ansys

In Ansys, a range of finite-element types is available, and the selection is made in accordance with the model's geometry, constituent materials, and anticipated loading conditions. Figures 3.2 and 3.3 shows some of the finite element types available in Ansys. Different element types are used for different purposes. The main features of these elements are summarized in the following sections [33].

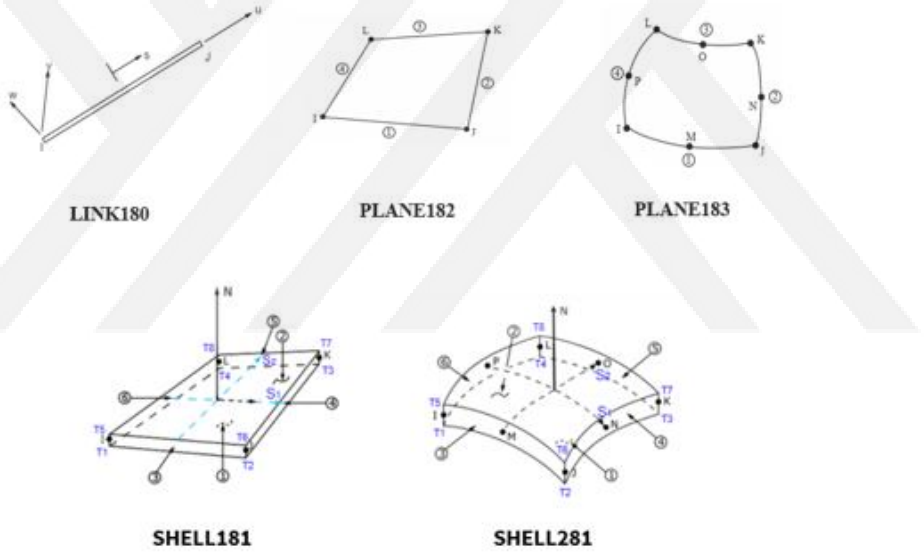



**Figure 3.2** Link, Plane and Shell Type Elements in Ansys [33]

**LINK180**

LINK180 is a three-dimensional spar element used for modeling trusses, cables, and connection elements. The element consists of two nodes and has three translational degrees of freedom at each node in the x, y, and z directions. It exhibits

uniaxial tension–compression behavior and can be defined as tension-only or compression-only, while bending effects are neglected.

**PLANE182**

PLANE182 is a two-dimensional solid element used for modeling plane stress, plane strain, and axisymmetric problems. The element is defined by four nodes with two translational degrees of freedom at each node in the x and y directions. It supports nonlinear behaviors such as plasticity, hyperelasticity, large deflection, and large strain effects.

**PLANE183**

PLANE183 is a higher-order two-dimensional solid element with quadratic shape functions. The element can be defined with six or eight nodes and is suitable for modeling irregular mesh geometries. It can be used in plane stress, plane strain, and axisymmetric analyses, while also supporting nonlinear behaviors including plasticity, creep, large deflection, and large strain effects.

**SHELL181**

SHELL181 is a four-node shell element used for the analysis of thin and moderately thick shell structures. Each node has six degrees of freedom consisting of three translational and three rotational components. The element is suitable for both linear and nonlinear analyses involving large rotations and large strains and can also be used for modeling layered and composite shell structures.

**SHELL281**

SHELL281 is a higher-order shell element used for modeling three-dimensional structural problems. The element is defined by eight nodes, and each node possesses six degrees of freedom consisting of three translational and three rotational components.

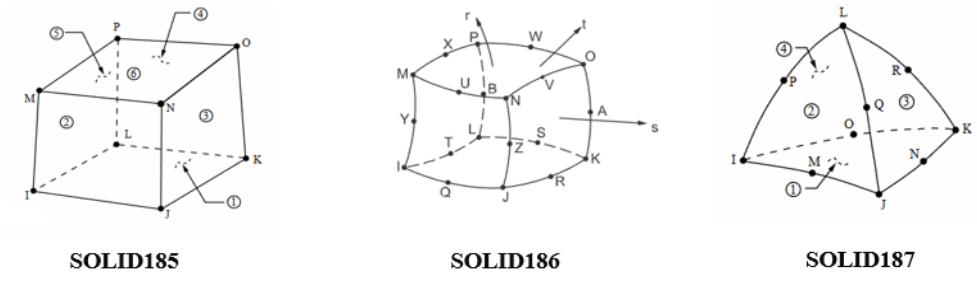



**Figure 3.3** SOLID Type Element in Ansys [33]

**SOLID185**

SOLID185 is an eight-node solid element used for modeling three-dimensional solid structures. Each node has three translational degrees of freedom in the x, y, and z directions. The element supports nonlinear behaviors such as plasticity, hyperelasticity, creep, large deflection, and large strain effects.

**SOLID186**

SOLID186 is a higher-order three-dimensional solid element with quadratic displacement behavior. The element is defined by 20 nodes, each having three translational degrees of freedom. It supports nonlinear capabilities including plasticity, hyperelasticity, creep, stress stiffening, large deflection, and large strain behavior.

**SOLID187**

SOLID187 is a higher-order three-dimensional solid element suitable for modeling irregular mesh geometries. The element consists of 10 nodes with three translational degrees of freedom at each node in the x, y, and z directions. It supports nonlinear analysis features such as plasticity, hyperelasticity, creep, large deflection, and large strain effects.

**REIN264**

REINF264 is a three-dimensional reinforcing element in Ansys used for modelling embedded reinforcement within solid structural elements. The element allows reinforcing fibers to be defined in arbitrary orientations while sharing the same nodal locations and degrees of freedom as the host solid element. REINF264 supports nonlinear analyses including plasticity, creep, large deflection, and large

strain effects. It is widely used in the numerical modelling of reinforced concrete structures.

## 3.3 Contacts

In finite element analyses, contact definitions are employed to represent the interaction behavior between different structural components. Depending on the connection characteristics and expected mechanical response, various contact elements and contact types can be defined in Ansys to simulate separation, sliding, and frictional behavior between contacting surfaces [34].

### 3.3.1 Contact Elements

**CONTA174**

CONTA174 is a surface-to-surface contact element used for modeling frictional, frictionless, or bonded contact behavior in three-dimensional analyses. The element can simulate nonlinear effects such as sliding and separation between contacting surfaces.

**CONTA175**

CONTA175 is a node-to-surface contact element employed in three-dimensional contact analyses. The element is generally used together with target elements to represent the interaction behavior between contacting components.

**TARGE170**

TARGE170 is a target element used together with contact elements in three-dimensional contact analyses. The element defines the target surface onto which the contact elements interact.

### 3.3.2 Contact Types

**Bonded Contact**

Bonded contact fully restrains the contacting surfaces and prevents both separation and sliding between them.

**No Separation Contact**

No Separation contact prevents separation of the contacting surfaces while allowing tangential sliding.

**Frictionless Contact**

Frictionless contact permits sliding between contacting surfaces without considering frictional resistance.

**Frictional Contact**

Frictional contact transfers both normal and tangential forces between contacting surfaces through a defined friction coefficient.

## 3.4 Material Models

### 3.4.1 Plasticity Models

In the Ansys environment, plastic behavior is represented through material models defined under the Plasticity category. The Bilinear and Multilinear Isotropic/Kinematic Hardening models are developed to represent the behavior of ductile materials exhibiting plastic deformation after yielding. These models are used to describe conditions in which the material undergoes permanent deformation and plastic flow after exceeding the elastic limit [33,35].

#### 3.4.1.1 Bilinear Isotropic Hardening

Bilinear isotropic hardening is a bilinear stress–strain approach that defines a constant plastic slope after the elastic region. In this model, the yield surface expands concentrically with increasing plastic deformation. Due to its simple formulation and numerical stability, it is widely used in nonlinear finite element analyses [33].

#### 3.4.1.2 Multilinear Isotropic Hardening

Multilinear isotropic hardening allows the stress–strain relationship in the plastic region to be represented by multiple linear segments. This model is employed to obtain results that are closer to experimental material behavior and provides realistic responses under monotonic loading conditions [33].

#### 3.4.1.3 Bilinear Kinematic Hardening

It is based on the translation of the yield surface in stress space. It is preferred due to its capability to represent the Bauschinger effect occurring under cyclic loading conditions [33,36].

#### 3.4.1.4 Multilinear Kinematic Hardening

The multilinear kinematic hardening model [33] is a kinematic hardening approach used to describe the plastic behavior of the material under cyclic loads. The model is based on representing the stress–plastic strain curve with multiple linear segments and relies on the principle of the translation of the yield surface in stress space as plastic deformation progresses. This approach is widely used, especially in modeling the Bauschinger effect and hysteretic behavior that occur under cyclic loading. The theoretical foundation of the model is based on the mathematical representation of the multiaxial Bauschinger effect developed by Armstrong and Frederick and was later expanded with viscoplastic and kinematic hardening theories developed by Chaboche [36,37].

### 3.4.2 Concrete Model – Menétrey–Willam Model

The Menétrey–Willam model is an advanced plasticity model developed to describe the complex and nonlinear behavior of concrete [38]. Based on the Willam–Warnke yield surface, the model considers both hydrostatic stress conditions and deviatoric stress effects, enabling accurate representation of cracking, crushing, and plastic deformation processes of concrete under multiaxial stress states [39]. The model is widely preferred particularly in finite element analyses of RC structures performed using software such as Ansys. Recent studies conducted by Mestnikov et al. [40] have further confirmed the capability and numerical stability of this model in representing the stress–strain behavior of RC beams.

### 3.4.3 Hyperelastic Model

Hyperelastic models have been developed to characterize the large deformations and nonlinear elastic behavior exhibited by rubber-like materials. In these models, material behavior is defined through the strain energy density function, which represents the energy stored per unit volume [41]. Different hyperelastic approaches such as Neo-Hookean, Mooney–Rivlin, and Ogden can be defined in the Ansys environment. These models are particularly preferred for the realistic representation of elastomeric and rubber-based materials.

# 4
# VERIFICATION OF THE NUMERICAL MODEL

To assess the accuracy and reliability of the finite element model developed in this study, a validation procedure was performed using the experimental results reported by Arduini et al. [42]. The reference specimen, denoted as Beam A1, was selected as the benchmark case for comparison. The numerical model was established to replicate the geometry, reinforcement detailing, loading configuration, and boundary conditions of the experimental setup as closely as possible. This approach enabled a direct and consistent comparison between numerical predictions and laboratory observations.

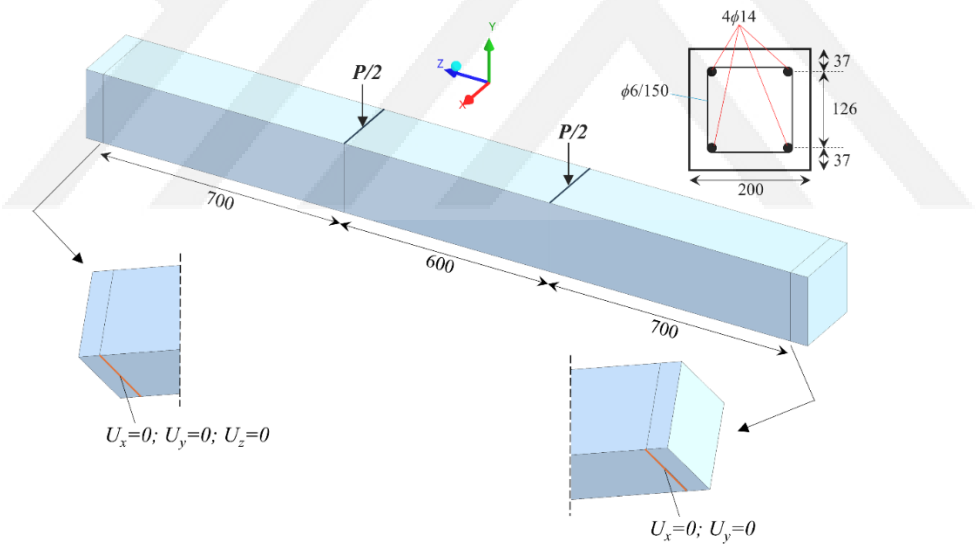



**Figure 4.1** Cross-sectional properties, loading configuration, and boundary conditions of Beam A1

As shown in the Figure 4.1, the RC beam had a square cross-section of 200×200 mm and was reinforced with four longitudinal bars of 14 mm diameter placed in both tension and compression zones. Shear reinforcement consisted of 6 mm

diameter stirrups spaced at 150 mm intervals. The beam was subjected to a two-point loading scheme, and appropriate boundary conditions were defined at the supports to reproduce the experimental conditions.

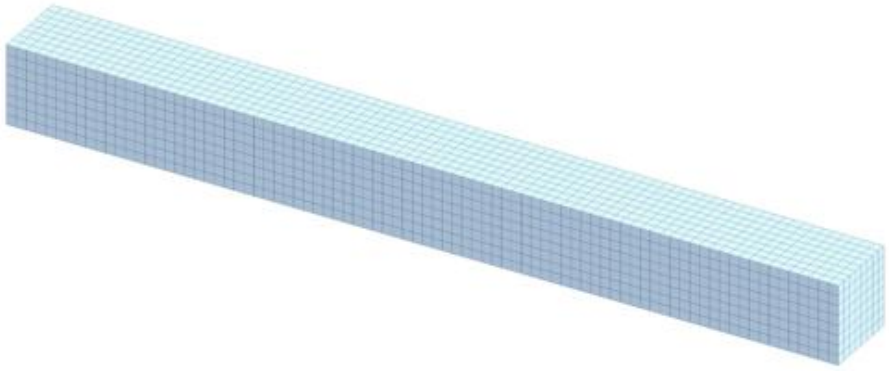


**Figure 4.2** Finite element discretization of the beam and illustration of the element types used for concrete and reinforcement.

Figure 4.2 illustrates the finite element model in which the concrete was represented using SOLID185 elements, while the reinforcement was modeled using REINF264 elements embedded within the concrete domain. A perfect bond assumption was adopted between concrete and reinforcement, eliminating relative slip at the interface. A mesh sensitivity study was conducted, and a global element size of approximately 25 mm was selected as a balance between computational efficiency and solution accuracy.

The nonlinear behavior of concrete was simulated using the Menétrey–Willam failure criterion available in the Ansys material library. The compressive strength of concrete was taken as 36.3 MPa, while the tensile strength was defined as 2.6 MPa [42]. The Poisson's ratio was assumed as 0.2, and a dilation angle of 12° was adopted. The compressive stress–strain relationship was defined using a parabolic formulation, whereas an exponential softening model was employed to represent the tensile behavior of concrete. These constitutive relationships are illustrated in Figure 4.3, where the uniaxial compression and tension responses used in the numerical model are presented. The curves demonstrate the nonlinear nature of concrete, including stiffness degradation and post-peak softening, which are essential for accurately capturing cracking and crushing mechanisms.

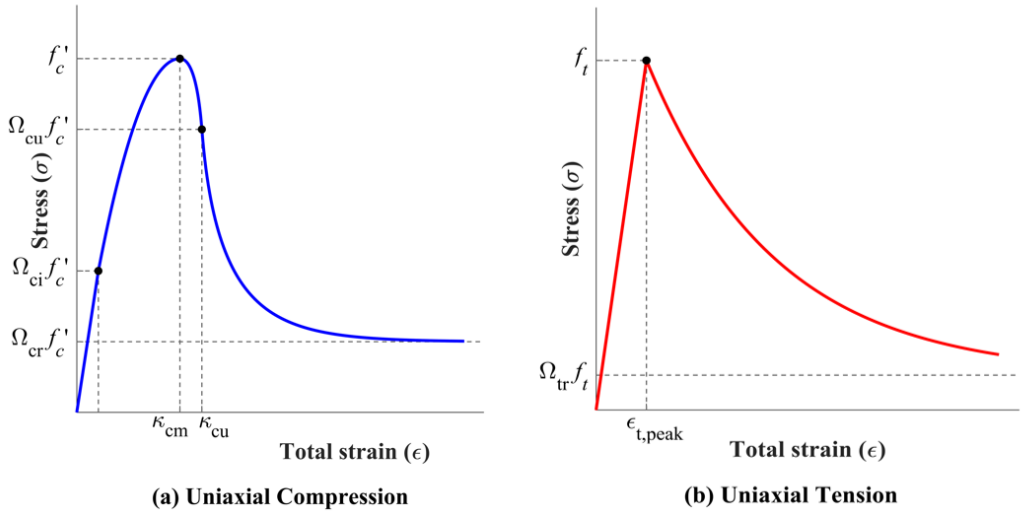



**Figure 4.3** The constitutive model for concrete

The material parameters adopted for the concrete model are summarized in Table 4.1. These definitions allow the model to capture stiffness degradation, cracking, and post-peak softening behavior of concrete.

The reinforcement steel was modeled using a bilinear isotropic hardening model with an elastic modulus of 200 GPa, Poisson's ratio of 0.3, yield strength of 540 MPa, and ultimate strength of 700 MPa and an ultimate strain of 0.1 [42].

Although the elastic modulus of concrete was initially taken as 25 GPa based on the experimental data [42], a calibration study was performed to improve the agreement between numerical and experimental responses. As a result, an effective elastic modulus of 20 GPa was adopted in the simulations. This adjustment accounts for the inherent heterogeneity of concrete, as well as microcracking effects that influence the initial stiffness of the specimen.

**Table 4.1** Concrete material properties defined according to the Menétrey–Willam model

| Parameter | Value |
|---|---|
| Plastic strain at uniaxial compressive strength ($\kappa_{cm}$) | 0.002 |
| Plastic strain at transition from power law to exponential softening ($\kappa_{cu}$) | 0.0025 |
| Relative stress at start of nonlinear hardening ($\Omega_{ci}$) | 0.4 |
| Residual relative stress at transition from power law to exponential softening ($\Omega_{ci}$) | 0.8 |
| Residual compressive relative stress ($\Omega_{cr}$) | 0.2 |
| Mode 1 area specific fracture energy ($G_{ft}$, N/m) | 140 |
| Residual tensile relative stress ($\Omega_{tr}$) | 0.1 |

The comparison between the numerical and experimental results is presented in Figure 4.4 in terms of load versus mid-span deflection response. The numerical model demonstrates a high level of agreement with the experimental data throughout the loading history. In particular, the model successfully captures the initial stiffness, cracking behavior, and post-yield response of the beam. The ultimate load capacity predicted by the numerical model differs from the experimental result by approximately 2%, confirming the validity and robustness of the adopted modeling approach and material parameters.

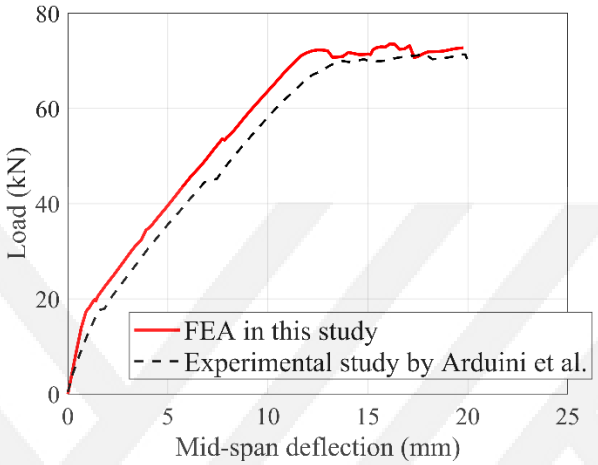



**Figure 4.4** Comparison between the load–midspan deflection curves obtained from the finite element analysis in this study and the experimental results [42]

# 5
# FINITE ELEMENT MODELS

## 5.1 Idealization

In the development of the structural model, the typical internal force distribution observed in RC moment-resisting frames under seismic loading was taken into consideration. When the bending moment diagram along beam elements in frame systems subjected to lateral earthquake loads is examined, it is observed that the moment values reach their maximum levels at the beam–column joint regions and pass through zero at a location close to the mid-span of the beam. This location is commonly referred to as the zero-moment point or the inflection point in structural analysis. This situation is illustrated schematically in Figure 5.1. The bending moment diagram shown by the red line in the frame system on the right side of the figure indicates that the moment becomes zero near the beam mid-span, while the maximum moment values occur at the beam–column joints. Considering this moment distribution, it becomes possible to cut the beam element at its mid-point and model only half of the span. With this approach, the computational model is simplified while the critical behavior at the connection region can still be accurately represented.

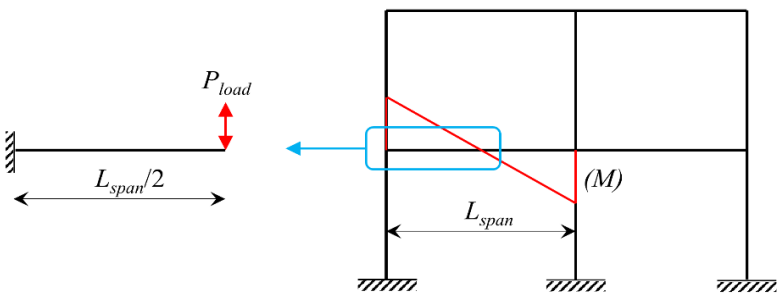



**Figure 5.1** Idealized half-span beam model based on the moment distribution under lateral loading

For this reason, the analysis model was simplified as a cantilever beam with a length corresponding to half of the clear span ($L_{span}$/2). In the simplified model shown on the left side of Figure 5.1, the end of the beam connected to the column was defined as a fixed support. This region represents the critical connection zone where the highest moment demands occur under seismic effects. The other end of the model corresponds to the beam mid-span, where the bending moment is zero in the real structural system, and a vertical load ($P_{load}$) was applied at this point. In this way, a loading condition equivalent to the moment distribution occurring in frame systems under seismic loading was obtained.

In this modeling approach, the fixed support condition was directly assigned to the beam–column interface. The free end represents the mid-span location of the beam in the actual structural system. However, it is known that the assumption of a fully fixed support does not completely represent the rotational flexibility of the column and the joint region. Nevertheless, this simplification is considered acceptable since the primary objective of the present study is to investigate the hysteretic behavior, energy dissipation capacity, and damage distribution of the proposed connection device.

Although the flexibility of the column element and the deformations occurring in the joint region may influence the global structural response in real structures, the main mechanism investigated in this study is the interaction between the device and the RC beam. Therefore, neglecting the rotational flexibility of the column in the model does not significantly affect the overall system behavior and provides sufficient accuracy for evaluating the performance of the device.

Through this idealized model, the moment transfer occurring at the beam end under seismic loading, together with the energy dissipation behavior resulting from the friction mechanism and the contribution of the elastomer elements, could be examined in detail.

## 5.2 Geometry of RC Beam

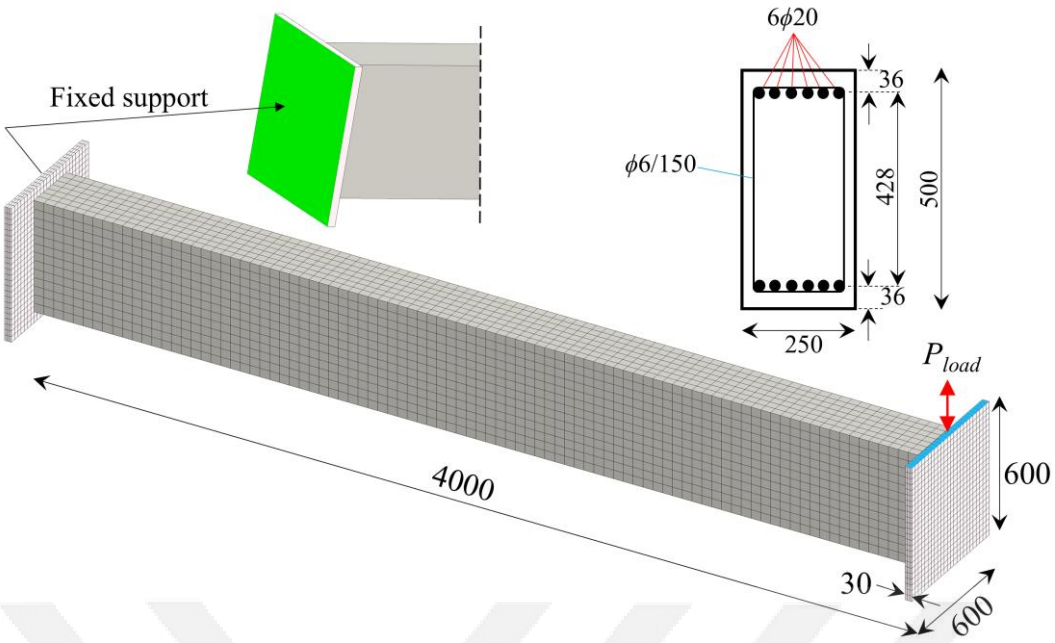



**Figure 5.2** Geometric properties, reinforcement detailing, boundary conditions, and mesh structure of the reference RC beam (units:mm)

The geometric properties, reinforcement layout, and the generated finite element mesh of the reference RC beam are presented in Figure 5.2. The beam element used in the model has a rectangular cross-section with dimensions of 250 mm in width and 500 mm in height. The total length of the beam is 4000 mm, which represents half of the clear span ($L_{span}$/2). The cross-sectional design was developed considering the ductile behavior principles commonly adopted in RC beam design.

Within the cross-section, the longitudinal reinforcement is arranged symmetrically. Six longitudinal reinforcing bars with a diameter of 20 mm (6$\phi$20) are used in both the tension and compression regions. These reinforcements are located at the top and bottom regions of the section and are designed to increase the flexural capacity of the beam and to resist the tensile stresses that occur under seismic loading. Since the flexural behavior of RC members is largely controlled by longitudinal reinforcement, the proper placement of these bars within the section is of great importance. The positioning of the longitudinal reinforcement was determined considering the concrete cover and the required edge distances.

The transverse reinforcement (stirrups) used in the section has a diameter of 6 mm and is placed at 150 mm spacing ($\phi$6/150). The main functions of the stirrups are to

resist shear forces, prevent buckling of the longitudinal reinforcement, and confine the concrete core in order to enhance the ductile behavior of the structural element. For this reason, the stirrups were placed at regular intervals in the model and defined in a way that realistically represents the behavior of the RC member.

## 5.3 Geometry of the RC Beam Integrated With The Seismic Device

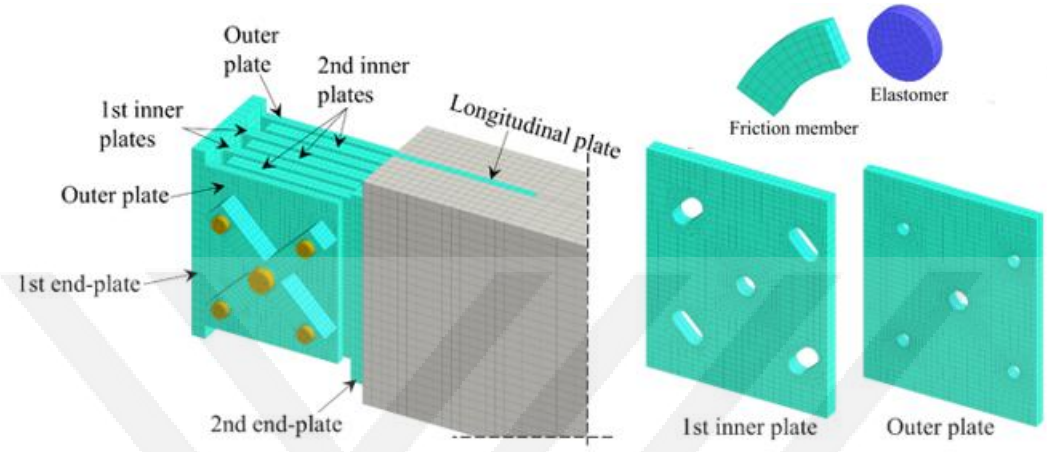



**Figure 5.3** Geometry of the connection device and finite element model

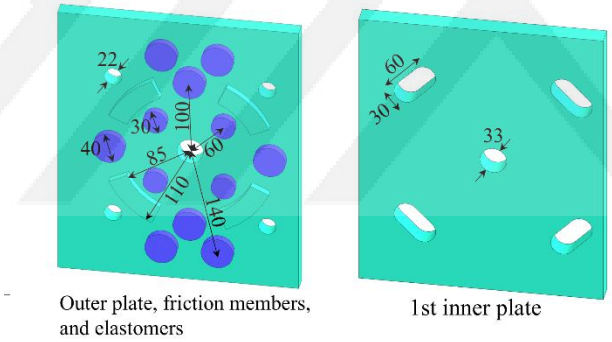



**Figure 5.4** Detailed dimensions of the friction and elastomeric components on the outer plate and the hole arrangement of the first inner plate

The device used in this study consists of six functional layers as illustrated in Figure 5.3. The system is formed by assembling two outer plates and five inner plates located between them. In order to define the boundary conditions and the force transfer mechanism more clearly in the analysis, the inner plates were classified into two groups according to their positions. The two inner plates located on the support side are defined as the first inner plates, while the three inner plates located on the span side are defined as the second inner plates.

The first inner plates are welded to the end plate on the support side, which is intended to be connected to the column face. The second inner plates are welded to the second end plate that provides the connection with the beam. In addition, a longitudinal steel plate welded to the second end plate is embedded into the RC beam in order to provide force transfer between the steel device and the RC member.

In the geometric configuration of the device, friction members and elastomeric pads are positioned at specific radial distances. The locations of these elements and their distances from the center directly affect the moment capacity and the energy dissipation behavior of the device. The central master pin used in the connection is selected as an M30 bolt, while the additional connection elements are defined as M20 bolts. The thickness of both the friction members and the elastomeric pads is specified as 10 mm for each layer.

The geometric details and component arrangement of the outer plate and the first inner plate of the device are illustrated in detail in Figure 5.4. In the outer plate design, the friction elements and elastomeric pads are defined in a circular pattern. The friction elements are positioned at an average radial distance of 97.5 mm from the center.

Regarding the first inner plate geometry, load-transfer connection holes and slot (oval) holes are defined. While a primary connection hole with a diameter of 33 mm is located at the center of the plate and there are four holes for the additional bolts with a diameter of 22 mm, it is surrounded by four oval slots measuring 30×60 mm. These slot holes facilitate assembly tolerances and allow for the precise placement of the connecting fasteners.

The final configuration of the joint formed by the integration of the beam and the connection device is presented in Figure 5.5. The beam has a total length of 3610 mm, while the length of the connection device located at the support side is 390 mm. The support region is modeled as a fixed support, and the load ($P_{load}$) is applied vertically at the free end of the beam.

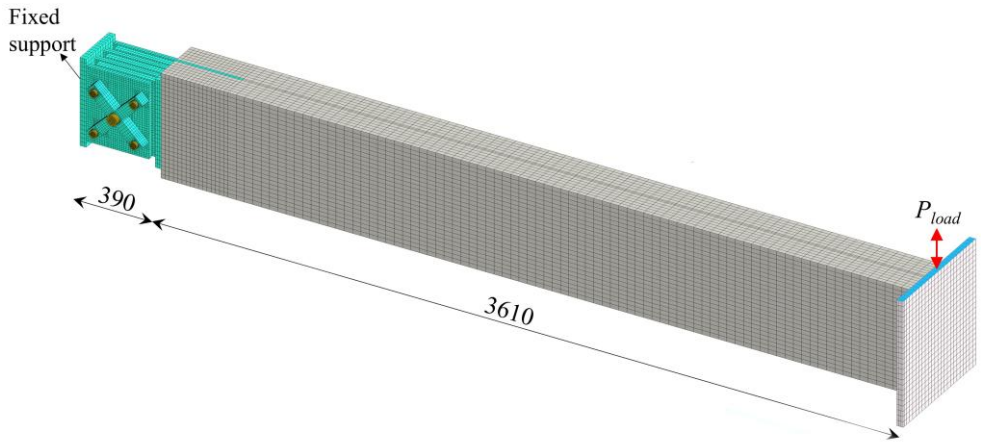



**Figure 5.5** Finite element representation of the RC beam integrated with the seismic connection device, including the component configuration and mesh discretization

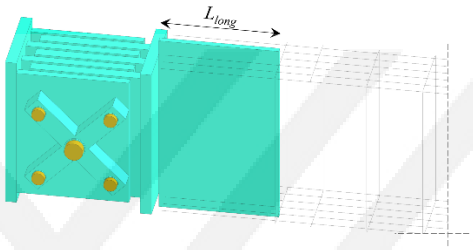



**Figure 5.6** Embedment length of the longitudinal plate ($L_{long}$) of the connection device within the RC beam

The final connection geometry obtained after integrating the beam with the connection device was designed to ensure the safe transfer of structural loads. In this configuration, the fundamental operating principle of the system is based on fixing the first end plate of the device to the column face, while the longitudinal steel plate welded to the second end plate is anchored into the RC beam body. In order to more clearly observe the position and continuity of the longitudinal plate within the beam, the RC component is presented in Figure 5.6 with a semi-transparent appearance. One of the most distinctive features of this design is that conventional stirrups were intentionally not placed along the embedment length of the longitudinal plate, defined as $L_{long}$. This arrangement is based on the assumption that the high shear capacity of the steel plate is sufficient to resist the shear forces that develop in this critical region. Therefore, the plate is not only considered as a connection interface, but also as a structural element that directly assumes the structural function of conventional shear reinforcement (stirrups) within the region where it is embedded.

## 5.4 Boundary Conditions

In the finite element model, the boundary conditions were defined to represent the fixed support behavior at the beam–column connection region. At this location, all displacement degrees of freedom of the beam end were restrained in order to simulate a fixed support condition. The loading was applied at the other end of the beam through a transverse displacement to generate bending effects and investigate the structural response. A displacement-controlled loading method was adopted due to its ability to provide stable solutions in nonlinear analyses.

To ensure a more uniform transfer of loads and boundary conditions over the beam cross-section, rigid steel plates with dimensions of 600×600×30 mm were attached to both ends of the beam, as illustrated in Figure 5.2. These plates enable a more uniform distribution of loads and reaction forces across the section and reduce local stress concentrations at the loading points.

## 5.5 Materials and Parameters

In the finite element model of the seismic connection device, different material models were assigned to accurately represent the mechanical behavior of each component. The primary structural components, including the outer plates, inner plates, and friction elements, were modeled using ASTM A572 Grade 50 structural steel. The fastening components, including the master pin, bolts, and washers, were modeled using high-strength ASTM A490 steel.

The material properties of ASTM A572 steel were defined with a density of 7850 kg/m$^3$, a modulus of elasticity of 202800 MPa, and a Poisson's ratio of 0.30. For ASTM A490 steel, the density was taken as 7850 kg/m$^3$, the modulus of elasticity as 205700 MPa, and the Poisson's ratio as 0.30.

Nonlinear cyclic behavior of the steel components was represented using the Multilinear Kinematic Hardening plasticity model. The stress–strain data used to define the hardening behavior of ASTM A572 and ASTM A490 steels were adapted from Gerami et al. [43].

The elastomeric pads used in the seismic connection device were modeled as Neoprene rubber. Since elastomeric materials exhibit nonlinear stress–strain behavior together with large deformation capacity, a hyperelastic material model

was required in the finite element analysis. In this study, the third-order Yeoh hyperelastic model was adopted to represent the mechanical response of the elastomer material under large strain levels.

The material definition was based on experimental data including uniaxial, biaxial, and shear test responses available in the Ansys material library and reported by Naeim and Kelly [44]. The Yeoh model parameters, namely $C_{10}$, $C_{20}$, $C_{30}$ and the compressibility constants $D_1$, $D_2$ and $D_3$ were obtained through a curve-fitting procedure performed using the experimental datasets. This procedure enabled the numerical model to accurately reproduce the nonlinear deformation characteristics of the elastomer material.

The constitutive stress–strain relationships used for the steel components and bolts, together with the curve-fitting results of the Yeoh hyperelastic model for the elastomeric material, are presented in Figure 5.7. The material constants determined for the Yeoh model are summarized in Table 5.1.

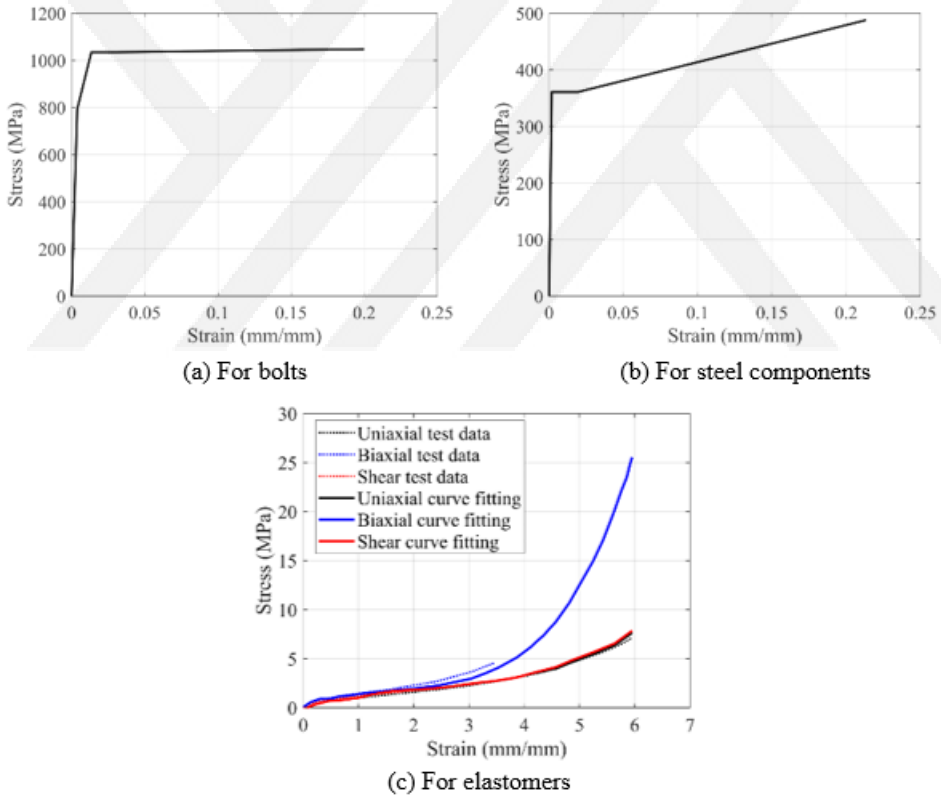



**Figure 5.7** Material constitutive relationships used in the numerical model: (a) bolts, (b) steel components, and (c) elastomeric material (experimental data and Yeoh hyperelastic curve fitting).

**Table 5.1** Material constants determined for the third-order Yeoh hyperelastic model [28]

| $C_{10}$ (MPa) | $C_{20}$ (MPa) | $C_{30}$ (MPa) | $D_1$ (MPa$^{-1}$) | $D_2$ (MPa$^{-1}$) | $D_3$ (MPa$^{-1}$) |
|---|---|---|---|---|---|
| 0.36149 | $-32.747\times10^{-4}$ | $0.78785\times10^{-4}$ | $53.653\times10^{-4}$ | $-65.26\times10^{-4}$ | $2.1414\times10^{-4}$ |

The nonlinear behavior of concrete was simulated using the Menétrey–Willam failure criterion available in the Ansys material library. The concrete material model adopted in the analyses was defined in accordance with the material properties and constitutive relationships presented in Chapter 4.

## 5.6 Mesh Details

Appropriate mesh generation strategies were employed in the finite element model to accurately represent the stress distributions, contact behavior, and force transfer mechanisms in the connection region. The mesh details and mesh control strategies used in the numerical model are illustrated in Figure 5.8.

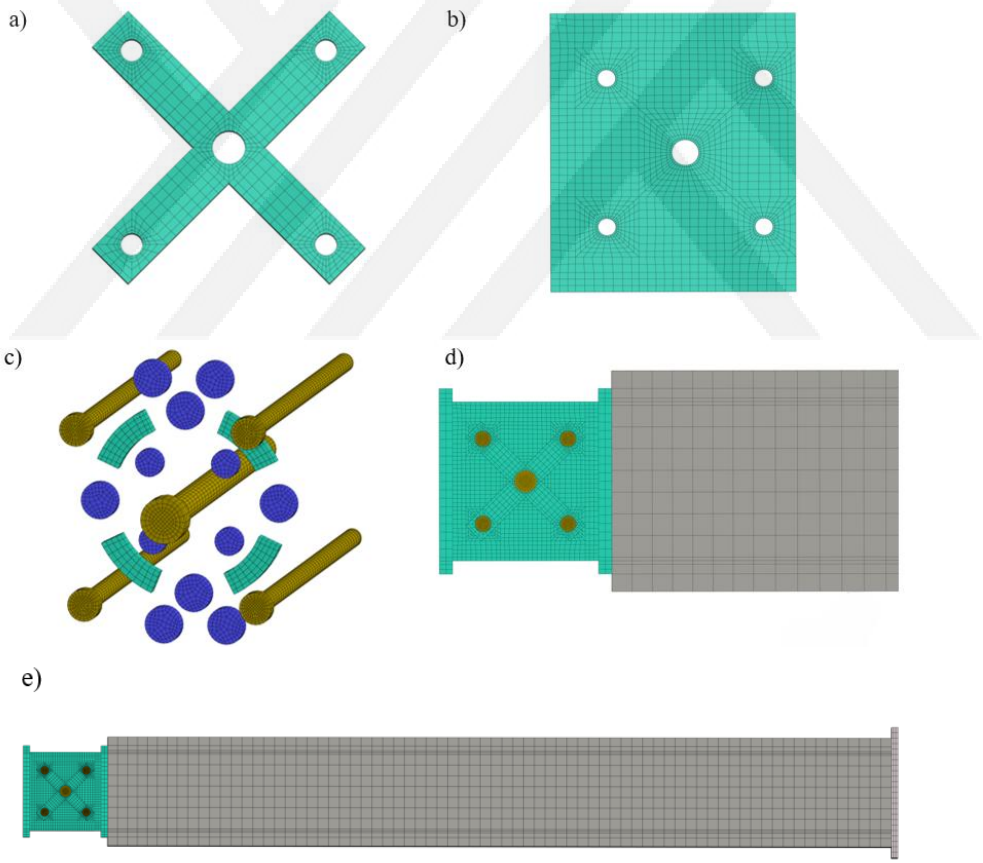



**Figure 5.8** Mesh Details of the model

Figure 5.8(a) illustrates the mesh generation strategy adopted for the friction member. A regular and structured mesh configuration was obtained using the MultiZone method. In addition, finer mesh regions were generated around the bolt holes and contact regions through the application of edge sizing controls. In this way, local stress concentrations and deformation behavior occurring on the contact surfaces could be represented more accurately.

Figure 5.8(b) presents the mesh structure generated around the inner plate region and bolt holes. Local mesh refinements were applied around the circular openings to accurately capture stress concentrations and contact behavior.

Figure 5.8(c) shows the mesh distribution of the master pins, elastomers, and friction members. A regular and dense mesh structure was employed along the master pins to achieve a more precise representation of the force transfer mechanism. Finer mesh regions were generated around the edge zones of the circular elastomeric components and arc-shaped friction members by applying edge sizing controls. Thus, local stress concentrations, deformation behavior, and force transfer mechanisms occurring on the contact surfaces could be represented more accurately.

Figure 5.8(d) presents the overall mesh structure of the connection region together with the RC beam. While finer mesh regions were defined around the connection components, a relatively coarser mesh structure was used in the beam region to reduce computational cost.

Figure 5.8(e) shows the overall finite element mesh structure of the numerical model. Mesh density was increased in the connection region where nonlinear behavior and stress concentrations were expected, whereas a more regular and relatively uniform mesh structure was employed along the beam.

The generated mesh structure provided stable convergence behavior throughout the nonlinear analyses involving material nonlinearity, large deformations, and complex contact interactions, and contributed to the reliable representation of stress distributions within the connection region.

## 5.7 Contacts

Contact definitions were incorporated into the numerical model to accurately represent the interaction between the connected structural components. Proper definition of the contact behavior is essential for simulating force transfer, interface constraints, and sliding mechanisms under cyclic loading conditions.

### 5.7.1 Bonded Contact Definitions

The interfaces between the friction elements and both the outer and first inner plates were modeled as bonded contacts to maintain precise alignment and to ensure uniform pressure distribution, thereby mitigating the risk of eccentric loading or tipping. This modeling strategy enforces kinematic compatibility, ensuring that the friction elements and the respective plates act as a rigid assembly without relative sliding or separation.

Similarly, the connections representing physical welds specifically located between the inner and end plates were characterized using bonded contact definitions. This approach effectively constrains relative motion at these interfaces, ensuring that the monolithic behavior of the welded joints is accurately captured within the finite element framework.

### 5.7.2 Frictional Contact Definitions

Within the scope of this thesis, several frictional contact definitions were introduced in the finite element model to accurately represent the mechanical interactions between the device components. In accordance with the working principle of the proposed energy dissipative connection device, the primary interaction representing the energy dissipation mechanism occurs between the friction members and the second inner plates. Therefore, frictional contact was defined between these surfaces. This definition allows the relative sliding motion occurring at the friction interfaces under cyclic loading to be represented in the finite element model, thereby realistically simulating the energy dissipation behavior of the device.

In the literature, the coefficient of friction for high-strength steel surfaces is reported to vary approximately between 0.30 and 0.50, depending on the surface preparation method. As reported by Kulak et al. [45], standard clean mill scale surfaces typically provide a friction coefficient of approximately 0.30, whereas blast-cleaned surfaces

may achieve values close to 0.50 due to their increased surface roughness. Accordingly, the frictional behavior and energy dissipation performance of the connection are directly influenced by both the surface characteristics and the geometric configuration of the contact interfaces. In this study a friction coefficient of 0.40 was selected throughout the finite element analyses. This value represents an intermediate and commonly accepted coefficient within the range reported in the literature and provides a realistic basis for evaluating the cyclic response and energy dissipation performance of the proposed device.

In addition to this primary interaction, additional frictional contact definitions were introduced in the model in order to represent other mechanical interactions between the device components. The frictional contact pairs defined in the model are presented below according to their interaction groups:

**Energy dissipation interface:** The fundamental friction interface representing the energy dissipation mechanism of the proposed connection device is the interaction between the friction members and the second inner plates. The relative sliding motion occurring between these surfaces during cyclic loading generates the frictional resistance that enables the device to dissipate energy.

**Plate–stiffness member interface:** In the finite element model developed in this study, frictional contact was defined between the outer plate and the stiffness member. This definition enables the representation of contact forces and potential limited relative sliding behavior between these two components during loading.

**Bolt shank–hole interaction:** In order to accurately represent the behavior of the bolted connection system, frictional contact was defined between the bolt shank surfaces of the master pin and the additional bolts and the hole surfaces located in the outer plate, first inner plates, second inner plates, stiffness member, and washers. This modeling approach allows the finite element model to capture contact pressure, bearing stresses, and limited sliding behavior occurring at the bolt–hole interfaces.

**Bolt head–washer interaction**: Frictional contact was defined between the bottom surfaces of the bolt heads (master pin and additional bolts) and the top surface of the washer. This interaction represents the transfer of forces from the bolt heads to the connected steel components through the washer.

**Washer–stiffness member interaction:** Frictional contact was defined between the bottom surface of the washer and the contacting top surface of the stiffness member. This interaction represents the load transfer mechanism from the bolt head to the stiffness member through the washer within the bolted connection system.

### 5.7.3 Frictionless Contact Definitions

The interaction between the second end plate and the concrete surface of the RC beam was modeled as frictionless contact. This modeling approach ensures that the transfer of shear forces primarily occurs through the embedded longitudinal steel plate. In this way, the shear force transfer takes place through the steel plate rather than relying on surface friction at the beam end, while the transfer of compressive forces between the contacting surfaces remains possible.

### 5.7.4 Contact Formulation

For all frictional and frictionless contact pairs defined in the finite element model, the Augmented Lagrange contact formulation was employed. This formulation is commonly used in nonlinear contact analyses due to its stable convergence behavior and its ability to control penetration between contacting surfaces with adequate accuracy.

The formulation is particularly suitable for contact problems involving friction, sliding, and separation between interacting surfaces. By using this approach, the interaction behavior between the structural components and the nonlinear response associated with the friction-based energy dissipation mechanism were represented within the finite element model.

## 5.8 Loading Protocol

The numerical analyses were conducted in two successive loading stages to simulate the installation and loading conditions of the connection system. In the first stage, pretension forces were applied to the master pin and additional bolts in order to activate the friction mechanism. This procedure was applied only to the models containing the seismic device and was not required for the reference RC beam.

After the pretension stage, cyclic displacement-controlled loading was applied at the free end of the cantilever beam, as shown in Figure 5.7. A vertical displacement was imposed to generate bending action at the fixed support region.

The loading history was established based on a simplified form of the AISC 341 loading protocol [46]. Fully reversed single cycles were applied at increasing drift ratios of 0.00375, 0.005, 0.0075, 0.01, and 0.015 radians. The corresponding displacement values were determined according to the beam span length.

In the original AISC 341 protocol, multiple repeated cycles are applied at each drift level in order to evaluate cyclic degradation effects such as stiffness deterioration, strength loss, and overall damage progression. However, in the present study, a simplified loading protocol consisting of a single fully reversed cycle at each drift level was adopted, since the primary objective was to determine the fundamental hysteretic behavior, moment capacity, and the envelope boundary of the obtained hysteresis curves. This approach reduced the analysis duration and computational cost while still providing an adequate representation of the essential structural response of the connection system. Considering the high computational demand of the three-dimensional finite element model, which incorporates contact interactions and material nonlinearities, the adopted loading protocol was considered sufficient for evaluating the initial stiffness, moment-carrying capacity, and energy dissipation performance of the connection.

## 5.9 Finite Element Model Configurations

A total of eight finite element models were prepared in the study. One of these models was the conventional RC beam used as the reference specimen, while the remaining seven models consisted of beams incorporating the seismic connection device.

**Table 5.2** Finite Element Model Configurations and Defining Properties

| Model Name | Friction Coefficient | Pretension Force (kN) | Number of Longitudinal Plates | Length of Longitudinal Plate ($L_{long}$) (mm) | $M_F$ (kNm) | $M_E$ (kNm) | $M_{dev}$ (kNm) |
|---|---|---|---|---|---|---|---|
| RC Beam | - | - | - | - | - | - | - |
| T600-F40-1Ls | 0.40 | 600 | 1 | 320 | 140.4 | 1.04 | 141.44 |
| T900-F40-1Ls | 0.40 | 900 | 1 | 320 | 210.6 | 1.04 | 211.64 |
| T900-F40-1L | 0.40 | 900 | 1 | 640 | 210.6 | 1.04 | 211.64 |
| T1100-F40-1L | 0.40 | 1100 | 1 | 640 | 257.4 | 1.04 | 258.44 |
| T1100-F40-3L | 0.40 | 1100 | 3 | 640 | 257.4 | 1.04 | 258.44 |
| T1440-F30-3L | 0.30 | 1440 | 3 | 640 | 252.7 | 1.04 | 253.74 |
| T900-F50-3L | 0.50 | 900 | 3 | 640 | 263.3 | 1.04 | 264.34 |

In order to evaluate the performance of the device, four main parameters were considered in the parametric study. First, the friction coefficient ($\mu$), representing the frictional resistance at the sliding interfaces, was investigated using values ranging from 0.30 to 0.50. Second, the pretension force ($T_F$), which represents the total clamping force applied to the bolts, was evaluated by considering different pretension levels varying between 600 kN and 1440 kN. In addition, models containing one and three longitudinal plates were prepared to investigate the influence of the number of longitudinal plates used in the device. Finally, longitudinal plate lengths ($L_{long}$) of 320 mm and 640 mm were considered in order to examine the effect of plate length on the behavior of the device.

The theoretical moment capacity of the device was determined by considering the combined moment contributions provided by the frictional and elastomeric components. The friction-induced moment contribution was calculated by considering the friction coefficient ($\mu$), the total pretension force applied to the bolts ($T_F$), and the effective distance between the center of rotation and the friction members ($x_F$). The moment contribution of the elastomeric components was determined by considering the shear stiffnesses of the elastomers ($k_E$) and the rotation angle ($\theta$). Finally, the total theoretical moment capacity of the device ($M_{dev}$) was obtained by combining the moment contributions of the frictional and

elastomeric components. The equations and geometric distances used in the calculations were derived from the geometry of the seismic device shown in Figure 2.3. The calculation procedure was applied to all models presented in Table 5.2, and the T600-F40-1Ls model was selected as an example to demonstrate the calculation steps.

For the T600-F40-1Ls model, the friction coefficient was taken as ($\mu$=0,40) and the total pretension force was ($T_F$ = 600 kN). Accordingly, the moment that the friction members were required to carry was obtained using Equation 2.1 as $M_F$ = 6·600·0.4·((0.11+0.085)/2) = 140.4 kNm. The elastomers used in the device have diameters of 30 mm and 40 mm, while their thickness is 10 mm. Accordingly, the shear stiffness of the 30 mm diameter elastomers was calculated using Equation 2.2 as $k_{E,30}$ = 0.723·(π·30$^2$/4)/10 = 51.11 N/mm while the shear stiffness of the 40 mm diameter elastomers was calculated as $k_{E,40}$ = 0.723·(π·40$^2$/4)/10 = 90.85 N/mm. A rotation angle of ($\theta$ = 0.01508) rad was assumed in the calculations. Accordingly, the moment contribution of the elastomers was calculated using Equation 2.3 as $M_E$ = 6·(4·51.11·0.015·0.06$^2$ + 4·90.85·0.015·0.1$^2$ + 4·90.85·0.015·0.14$^2$) = 1.04 kNm. Finally, the total theoretical moment capacity of the device was obtained by combining the moment contributions of the frictional and elastomeric components using Equation 2.4 as $M_{dev}$ = 140.4 + 1.04 = 141.44 kNm.

The reference RC beam exhibited a flexural moment capacity ($M_{rc}$) of approximately 206 kNm. This value was calculated using the standard flexural strength equation for doubly reinforced reinforced concrete sections given in Equation 5.1. The reference beam had a rectangular cross-section with dimensions of 250×500 mm and was reinforced with 6$\phi$20 tensile and 6$\phi$20 compression reinforcement.

$$M_{rc} = \left(A_s f_y - A_s' \sigma_s'\right)\left(d - \frac{a}{2}\right) + A_s' \sigma' \left(d - d'\right) \tag{5.1}$$

where $A_s$ and $A_s'$ are the tensile and compression reinforcement areas, $f_y$ is the yield strength of the reinforcing steel, $\sigma_s'$ is the stress in the compression reinforcement, $d$ is the effective depth, $d'$ is the depth of the compression reinforcement, and $a$ is the equivalent rectangular stress block depth. The tensile and compression reinforcement areas were calculated as $A_s$ = $A_s'$ = 6·(π·20$^2$/4) = 1885 mm$^2$. The

effective depth and the depth of the compression reinforcement were taken as $d$ = 464 mm and $d'$ = 36 mm, respectively. The concrete compressive strength, design concrete compressive stress, and yield strength of the reinforcing steel were taken as $f'_c$ = 33 MPa, $f_{cd}$ = 2.6 MPa, $f_y$ = 250 MPa. The reinforcement ratio was calculated as $\rho = \rho' = A_s / (b_w \cdot d)$ = 0.01625. The minimum reinforcement ratio was calculated as $\rho_{min} = 0.8 \cdot f_{cd}/f_y = (0.8 \cdot 2.6)/250 = 0.00832$. Since $\rho - \rho' = 0$, the coefficients required for determining the neutral axis depth were calculated as $A_1 = 0.85 \cdot f'_c \cdot b_w \cdot k_1 = 0.85 \cdot 33 \cdot 250 \cdot 0.80 = 610$, $A_2 = A'_s \cdot 600 - A_s \cdot f_y = 1885 \cdot 600 – 1885 \cdot 250 = 659750$ and $A_3 = -A'_s \cdot 600 \cdot d' = - 1885 \cdot 600 \cdot 36 = -40716000$. Accordingly, the neutral axis depth was calculated as $c$ = 44.71 mm. The equivalent rectangular stress block depth was then obtained as $a = k_1 \cdot c = 0.80 \cdot 44.71 = 35.77$ mm. The stress in the compression reinforcement was calculated as $\sigma'_s = 600 \cdot ((c - d')/c) = 600 \cdot ((44.71 - 36)/44.71) = 116.89$ MPa. Finally, using Equation 5.1, the flexural moment capacity was calculated as $M_{rc} = (1885 \cdot 250 – 1885 \cdot 116.89) \cdot (464 - 35.77/2) + 1885 \cdot 116.89 \cdot (464 - 36) = 206$ kNm. The calculated reference moment capacity was subsequently used as the baseline value for evaluating the contribution of the proposed seismic connection device in the subsequent numerical analyses.

# 6
# RESULTS

## 6.1 Hysteresis Response of the Prepared Models

During an earthquake, structural members are repeatedly forced to move in both directions. The cyclic bidirectional displacements occurring in structural members under seismic effects lead to cyclic rotations at the connection. Consequently, the induced bending moments fluctuate between positive and negative regimes. Hysteresis curves illustrate this cyclic behavior and the response of the connection under repeated loading. Each cycle observed in the hysteresis curves represents the loading, unloading, and reloading behavior in the opposite direction. The moment–rotation hysteresis responses obtained under cyclic loading for the analyzed models are presented in Figures 6.1–6.7. In each graph, the pink curve represents the proposed connection model, while the black curve represents the reference RC beam. The area enclosed by the hysteresis curves indicates the energy dissipated by the system under cyclic loading.

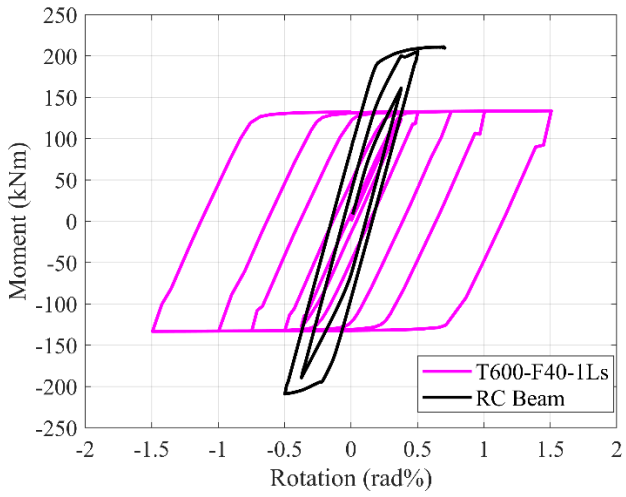



**Figure 6.1** Global moment–rotation hysteresis response of T600-F40-1Ls

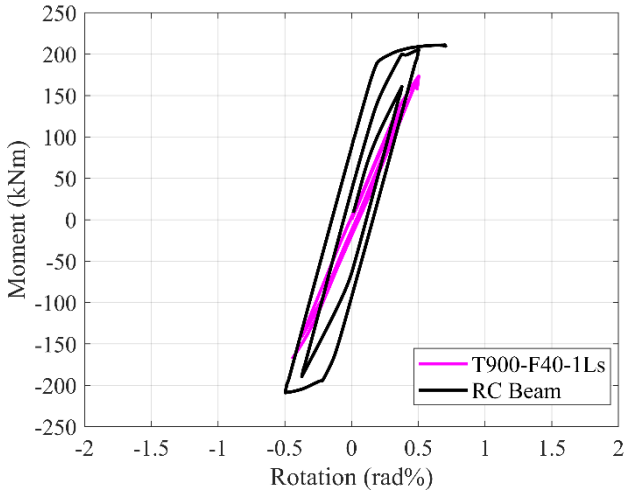



**Figure 6.2** Global moment–rotation hysteresis response of T900-F40-1Ls

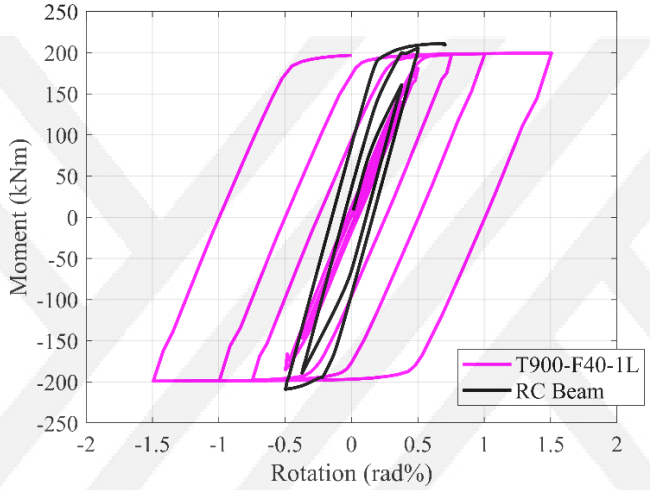



**Figure 6.3** Global moment–rotation hysteresis response of T900-F40-1L

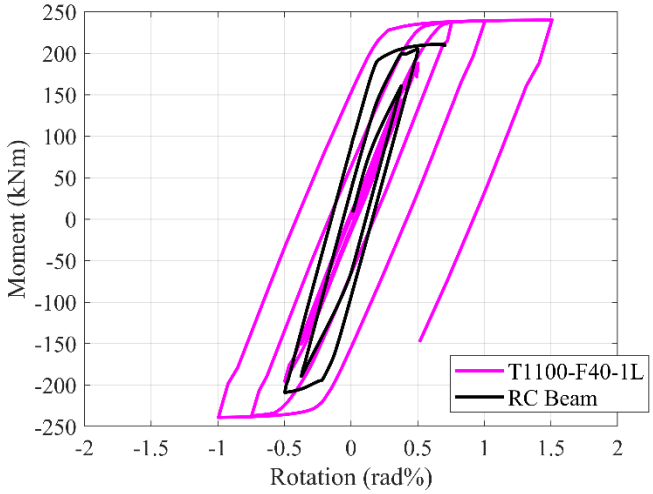



**Figure 6.4** Global moment–rotation hysteresis response of T1100-F40-1L

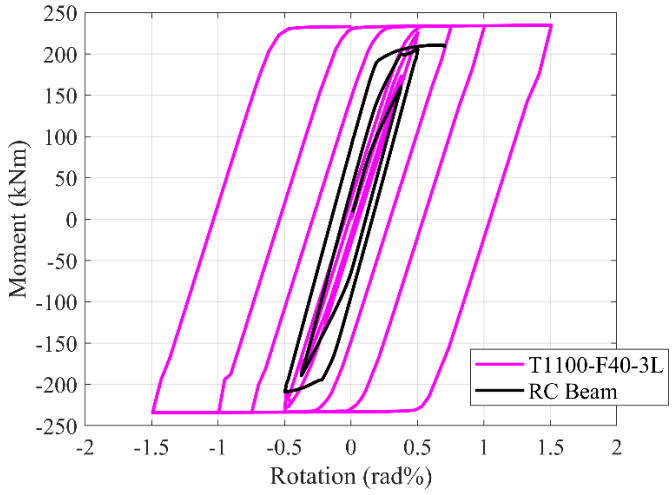



**Figure 6.5** Global moment–rotation hysteresis response of T1100-F40-3L.

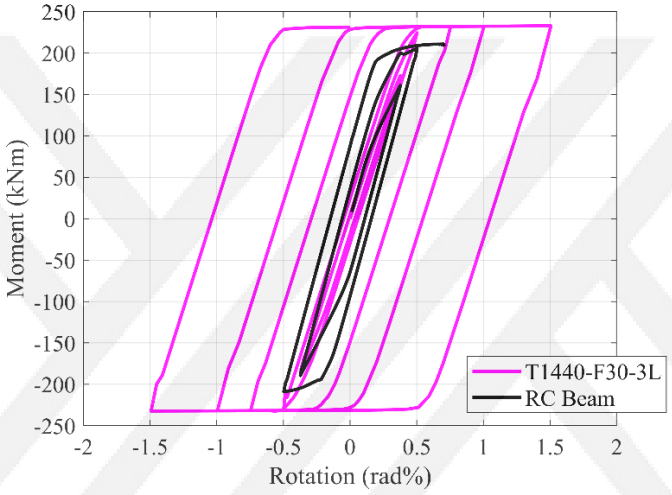



**Figure 6.6** Global moment–rotation hysteresis response of T1440-F30-3L.

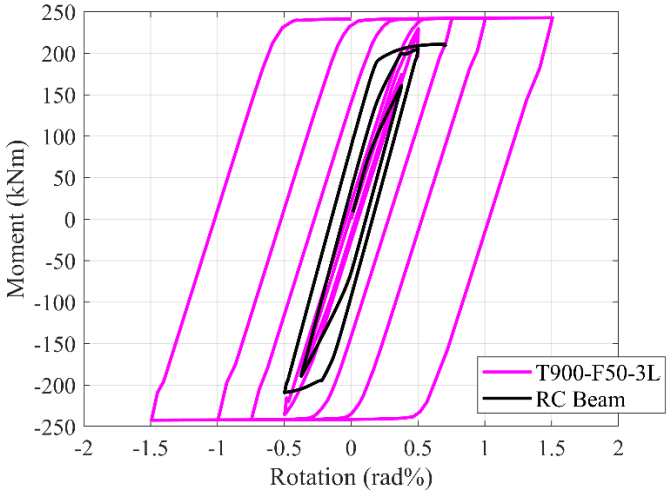



**Figure 6.7** Global moment–rotation hysteresis response of T900-F50-3L

In the hysteresis loops, the vertical axis denotes the bending moment (kNm) sustained by the joint, which corresponds to the total bending moment generated at the fixed support interface. Higher vertical peaks on the curve indicate that the connection possesses a greater moment capacity.

The horizontal axis represents the rotational response of the connection (rotation, rad%), corresponding to the rotation angle measured at the free end. This axis reveals the deformation and rotational capacity of the connection under seismic effects. The curve reaching large rotation values in both positive and negative directions indicate that the connection possesses a high deformation capacity and maintains its structural integrity without sudden failure under cyclic loading.

The reference RC beam model exhibited a ductile flexural response under cyclic loading, consistent with theoretical expectations. As the load increased, the longitudinal reinforcements in the cross-section reached their yielding limit, and the member subsequently engaged its non-linear (plastic) rotation capacity.

When the load was applied in a reversible manner, no sudden strength degradation or stiffness loss occurred throughout the beam. In addition, the absence of a significant pinching effect in the obtained hysteresis curves confirmed that the bond between the concrete and reinforcement did not deteriorate under seismic loading and that the shear cracks remained stable.

The theoretical moment capacities of the proposed connection system were determined using the $M_{dev}$ values presented in Table 5.2 from the previous section. These values were obtained by combining the moment contribution provided by the friction members ($M_F$) and the moment contribution generated by the elastomeric components ($M_E$) through Equations 2.1–2.4. For the reference RC beam, the theoretical flexural capacity ($M_{rc}$) was calculated using Equation 5.1.

Within this scope, the accuracy of the proposed analytical formulation was evaluated by comparing the maximum moment values obtained from the finite element analyses ($M_{max,FEA}$) with the theoretical moment capacities.

The $M_{max,FEA} / M_{dev}$ ratio indicates the capability of the theoretical calculations to represent the finite element analysis results. A ratio close to 1.0 indicates a good agreement between the proposed analytical formulation and the numerical results. The obtained comparative results are presented in Table 6.1.

**Table 6.1** Comparison of theoretical and finite element moment capacities of the analyzed models

| Model Name | $M_{rc}$ or $M_{dev}$ (kNm) | $M_{max,FEA}$ (kNm) | $M_{max,FEA}/M_{dev}$ |
|---|---|---|---|
| **RC Beam** | 206 | 210.9 | 1.024 |
| **T600-F40-1Ls** | 141.44 | 133.6 | 0.945 |
| **T900-F40-1Ls** | 211.64 | 173.5 | 0.820 |
| **T900-F40-1L** | 211.64 | 199.4 | 0.942 |
| **T1100-F40-1L** | 258.44 | 240.1 | 0.929 |
| **T1100-F40-3L** | 258.44 | 234.7 | 0.908 |
| **T1440-F30-3L** | 253.74 | 232.9 | 0.918 |
| **T900-F50-3L** | 264.34 | 242.9 | 0.919 |

For the device-equipped models, the $M_{max,FEA}/M_{dev}$ ratio varied between 0.945 for the T600-F40-1Ls model and 0.820 for the T900-F40-1Ls model. The T600-F40-1Ls model developed relatively stable rectangular-shaped hysteresis loops during the initial loading cycles. However, due to the limited strength capacity of the short embedment configuration, the moment capacity of this model remained considerably lower than that of the reference RC beam. The T900-F40-1Ls model, which exhibited the lowest ratio (0.820), showed a more limited deformation capacity and unstable hysteretic behavior at larger displacement levels.

Among the models with long embedment plates, the T900-F40-1L and T1100-F40-1L models reached maximum moment capacities of 199.4 kNm and 240.1 kNm, respectively. The analytical-to-numerical capacity ratios for these models were calculated as 0.942 and 0.929, respectively. Under cyclic loading, these models exhibited fuller and more stable hysteresis loops with lower strength degradation. Compared to the short embedment plate configurations, they maintained their moment resistance under higher rotation demands and developed greater deformation capacities.

The most stable hysteretic responses were obtained from the multi-plate configurations T1100-F40-3L, T1440-F30-3L, and T900-F50-3L. These models

exhibited wide and stable hysteresis loops throughout the cyclic loading history without experiencing any sudden strength degradation. The areas enclosed by these loops were larger than those of the short single-plate configurations.

To quantitatively evaluate the seismic performance of the proposed connection system, the cumulative energy dissipation ($E_d$) of each model was calculated. The energy dissipated by the system under cyclic loading was obtained from the area enclosed within the moment–rotation hysteresis loops. The moment–rotation data obtained from the finite element analyses were transferred to MATLAB [48], and the enclosed area of each hysteresis loop was numerically integrated for every loading cycle. Subsequently, the energy values corresponding to all loading cycles were summed to determine the total cumulative energy dissipation of each model. The calculated energy dissipation values are presented in Figure 6.8.

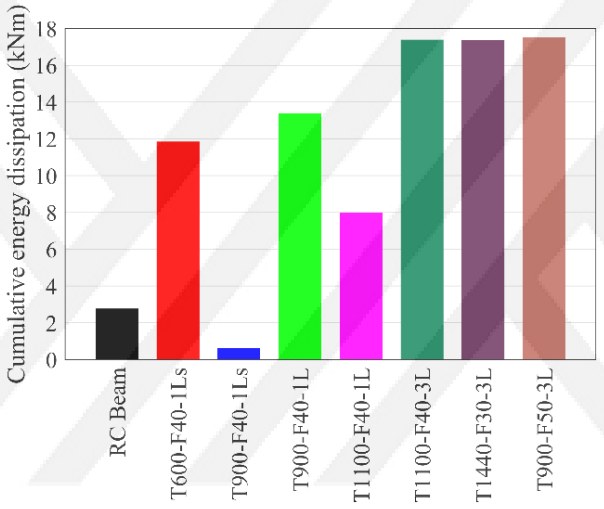



**Figure 6.8** Cumulative energy dissipation capacities of the analyzed models

The reference RC beam dissipated 2.77 kNm of energy. This beam experienced severe damage and reached its ultimate failure state at a drift ratio of approximately 0.71%. In contrast, the device-equipped models continued to dissipate energy up to a drift level of 1.5%.

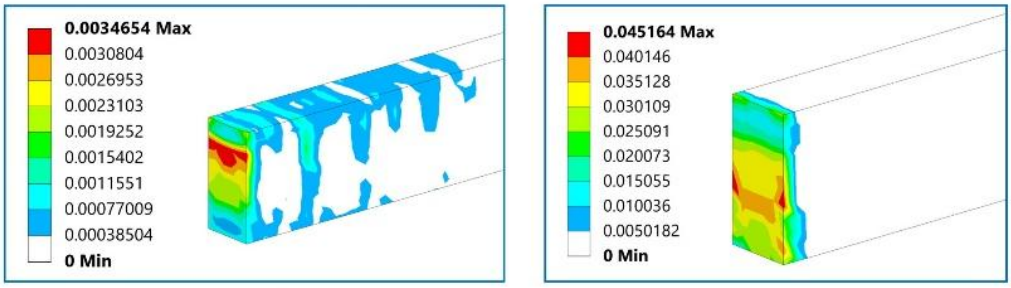
When the short single-plate models were examined, the T600-F40-1Ls model dissipated approximately 12.0 kNm of energy, whereas the T900-F40-1Ls model with the same embedment length dissipated only 0.63 kNm. Despite having the same embedment length, a significant difference in energy dissipation capacity was observed between these two models.

For the T900-F40-1L and T1100-F40-1L models, in which the embedment length was increased, the dissipated energy values were obtained as 13.5 kNm and 7.99 kNm, respectively. A more stable moment resistance under cyclic loading was observed in these models with the increased embedment length.

Among the investigated configurations, the T1100-F40-3L, T1440-F30-3L, and T900-F50-3L models, which utilized three longitudinal embedment plates, achieved the highest cumulative energy dissipation capacities, reaching approximately 17.4–17.5 kNm. In these models, plate continuity and sufficient embedment length were observed together with stable hysteretic behavior.

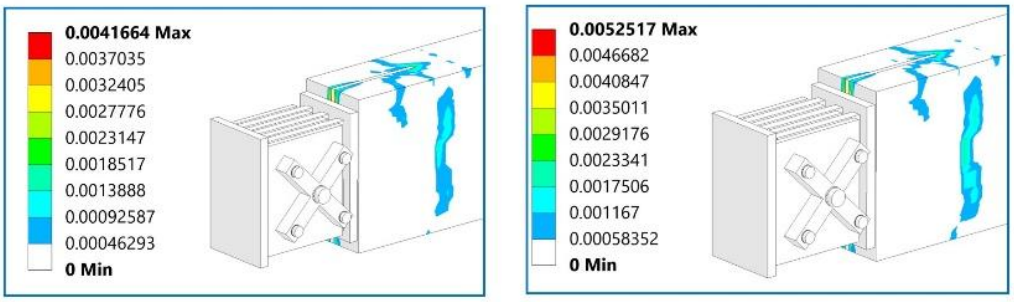
## 6.2 Distribution of Plastic Deformations and Failure Modes

In this study, the equivalent plastic strain parameter was chosen to evaluate damage development and localization in different connection models. The main reason for selecting this parameter is that plastic strain directly reflects the permanent deformations occurring in the material. While the material returns to its original state upon unloading within the elastic limits, the point at which plastic strain begins indicates the onset of physical damage such as cracking, crushing, or yielding in the material. As a single output parameter, plastic strain offers the advantage of simultaneously tracking cracking in the tension zone of concrete, crushing in the compression zone, and yielding behavior in reinforcement and connection elements. In this way, it has been possible to consistently assess at which load level, in which region, and with what intensity different types of damage occur.



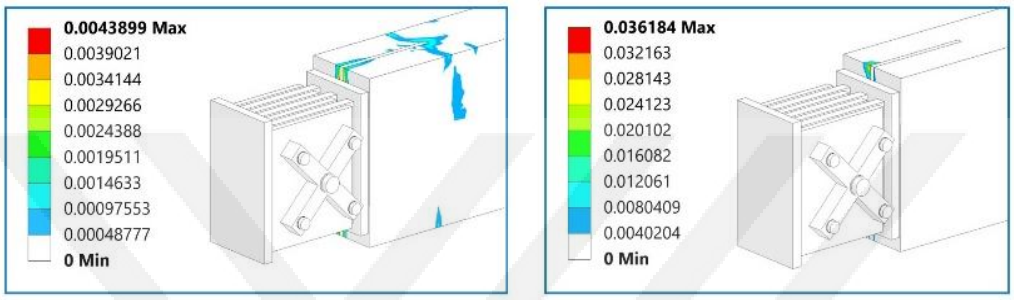

a) RC beam (-0.5 rad%) b) RC beam (0.71 rad%)

**Figure 6.9** The equivalent plastic strain distributions of the reference RC beam: (a) -0.5 rad; (b) 0.71 rad



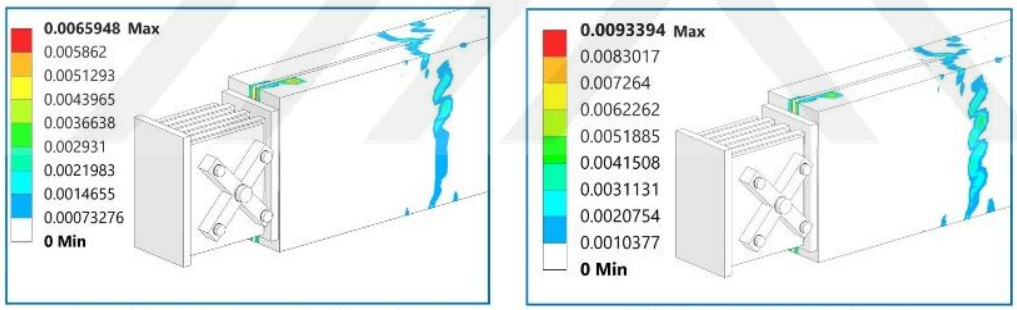

a) T600-F40-1Ls (-0.75 rad%) b) T600-F40-1Ls (end)

**Figure 6.10** The equivalent plastic strain distributions of the T600-F40-1Ls model: (a) -0.75 rad; (b) end



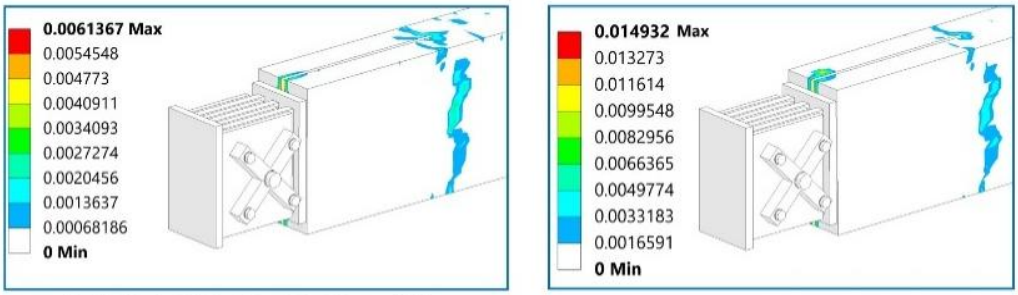

a) T900-F40-1Ls (-0.375 rad%) b) T900-F40-1Ls (-0.48 rad%)

**Figure 6.11** The equivalent plastic strain distributions of the T900-F40-1Ls model: (a) -0.375 rad; (b) -0.48 rad



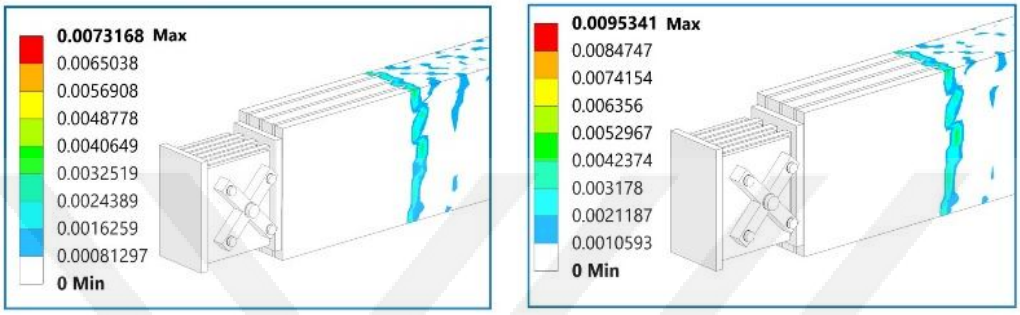

a) T900-F40-1L (-0.50 rad%) b) T900-F40-1L (end)

**Figure 6.12** The equivalent plastic strain distributions of the T900-F40-1L model: (a) -0.50 rad; (b) end



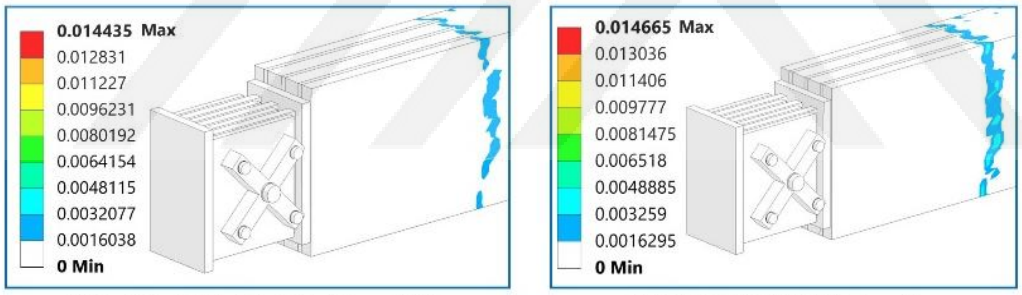

a) T1100-F40-1L (-0.50 rad%) b) T1100-F40-1L (1.50 rad%)

**Figure 6.13** The equivalent plastic strain distributions of the T1100-F40-1L model: (a) -0.50 rad; (b) 1.50 rad



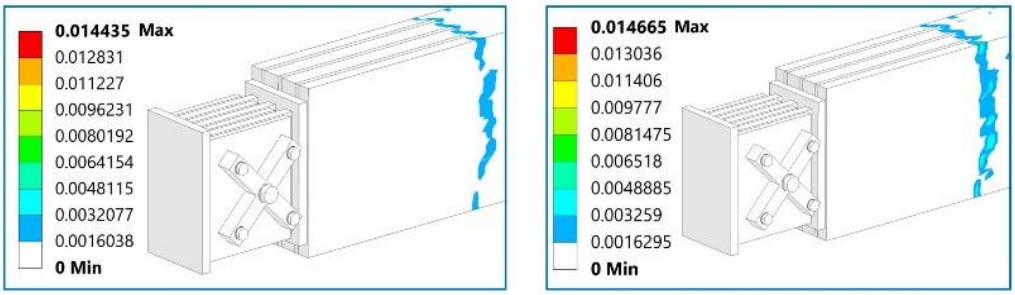

a) T1100-F40-3L (-0.50 rad%) b) T1100-F40-3L (end)

**Figure 6.14** The equivalent plastic strain distributions of the T1100-F40-3L model: (a) -0.50 rad; (b) end




a) T1440-F30-3L (-0.50 rad%) b) T1440-F30-3L (end)

**Figure 6.15** The equivalent plastic strain distributions of the T1440-F30-3L model: (a) -0.50 rad; (b) end




a) T1440-F30-3L (-0.50 rad%) b) T1440-F30-3L (end)

**Figure 6.16** The equivalent plastic strain distributions of the T900-F50-3L model: (a) -0.50 rad; (b) end

In the numerical analysis of the reference RC beam, plastic strains were observed to begin localizing at the fixed support interface during the first loading stage under a small rotation demand of 0.00375 rad. At this stage, the maximum equivalent plastic strain was approximately 0.0034 mm/mm. As shown in Figure 6.9(a), damage initiated near the support region and exhibited only limited propagation along the beam. As the loading was increased to the ultimate state corresponding to a 0.71% drift ratio, the damage became completely localized within a very narrow region at the fixed support interface, rather than spreading throughout the beam, as illustrated in Figure 6.9(b). The maximum equivalent plastic strain in this region reached a very high value of 0.045 mm/mm.

The device-integrated short single plate T600-F40-1Ls model, as shown in Figure 6.10(a), exhibited a maximum plastic strain value of 0.0041664 mm/mm at a drift level of -0.75% rad. Plastic deformation remained limited, while damage was concentrated near the termination region of the longitudinal plate and at the end portion of the embedment zone. Figure 6.10(b) presents the behavior of the same model at the end of the analysis. As the loading progressed, plastic deformations spread along the embedment region, and the maximum plastic strain value increased to 0.0052517 mm/mm. The plastic deformations remained concentrated within limited regions of the embedded zone.

In the T900-F40-1Ls model, where the pretension force was increased to 900 kN, the behavior changed significantly. As shown in Figure 6.11(a), at a drift level of -0.375% rad, the plastic strain value was obtained as 0.0043899 mm/mm. Plastic deformations were concentrated near the termination region of the longitudinal plate. In Figure 6.11(b), corresponding to the behavior at −0.48% rad drift level,

plastic deformations became significantly concentrated, and the maximum plastic strain value reached a considerably high level of 0.036184 mm/mm. Plastic strains were observed to occur mainly within the embedment region.

In the longer single-plate T900-F40-1L model, increasing the embedment plate length delayed the initiation of severe damage. As shown in Figure 6.12(a), a maximum equivalent plastic strain value of 0.0065948 mm/mm was obtained at a drift level of −0.50% rad. In Figure 6.12(b), the maximum plastic strain value increased to 0.0093394 mm/mm at the end of the loading protocol. Similar to the short single-plate models, plastic deformations were mainly concentrated along the boundary of the embedded plate.

In the T1100-F40-1L model, where the pretension force was increased to 1100 kN, a similar but more pronounced behavior was observed. As shown in Figure 6.13(a), a maximum equivalent plastic strain value of 0.0061367 mm/mm was obtained at a drift level of −0.50% rad, while plastic deformations remained limited around the plate boundary. However, during the final loading stage shown in Figure 6.13(b), plastic deformations became significantly concentrated and the maximum plastic strain value reached 0.014932 mm/mm. Although the strain localization propagated along the embedment region, the response was still observed to be governed by the confined region surrounding the embedded plate.

In the T1100-F40-3L model with a three-plate embedment configuration, as shown in Figure 6.14(a), the maximum equivalent plastic strain value was obtained as 0.00732 mm/mm at a drift level of 0.50% rad. In Figure 6.14(b), the maximum plastic strain value increased to 0.00953 mm/mm at the end of the loading protocol. Plastic deformations continued to develop as the loading progressed, but this development occurred in a controlled manner. That is, the connection did not create a sudden strain concentration while consuming more energy. Plastic deformations were concentrated mainly in the boundary regions of the outer embedded plates. However, it was observed that the maximum plastic strain value was significantly lower compared to the values obtained in single-plate models (e.g., 0.03618 mm/mm in the T900-F40-1Ls model).

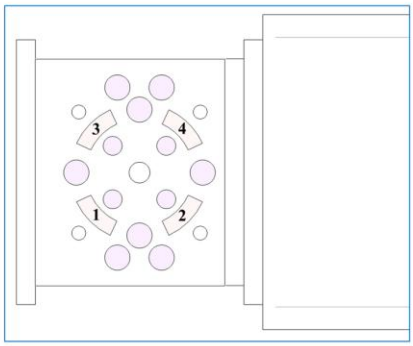
In the T1440-F30-3L model, the plastic strain demands within the connection region increased. As shown in Figure 6.15(a), the maximum equivalent plastic

strain value reached 0.014435 mm/mm at a drift level of −0.50% rad. In Figure 6.15(b), representing the end of the loading protocol, the maximum plastic strain value increased to 0.014665 mm/mm. Despite the increase in loading, the maximum plastic strain value changed only slightly from 0.014435 mm/mm to 0.014665 mm/mm, while the overall strain distribution remained relatively stable. Despite the higher strain levels, the deformation distribution remained relatively stable without abrupt localization within a single region.

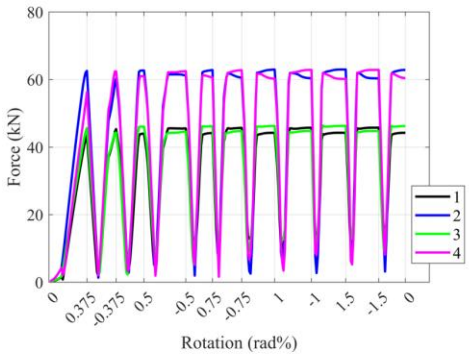
The T900-F50-3L model exhibited a maximum plastic strain value of 0.011157 mm/mm at the end of the loading protocol. In this model, plastic deformations were mainly concentrated along the embedded plate boundaries.

## 6.3 Force Transfer in Friction Members

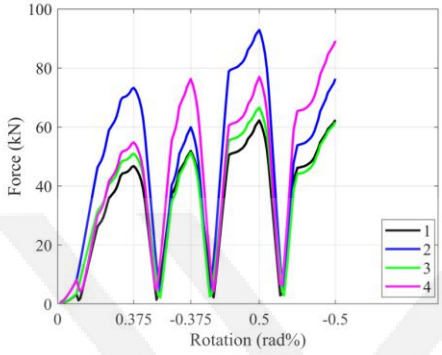
The findings regarding the force transfer of the friction members under the applied load are presented below. Friction members are components placed on the contact surfaces between the outer plate and the inner plate. In Figure 6.17(a), four friction parts on the plate are numbered. As seen in Figure 6.17, the horizontal axis in the graphs shows the rotation demand (Rotation, rad%), while the vertical axis shows the forces occurring in the friction elements (Force, kN).



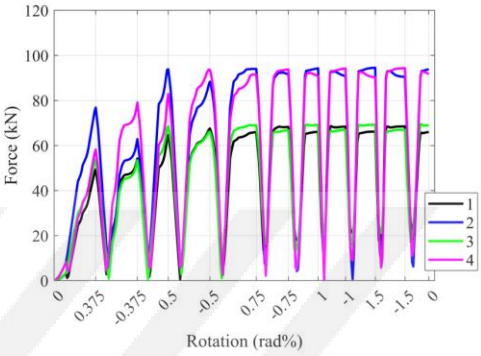

a) Friction members' number



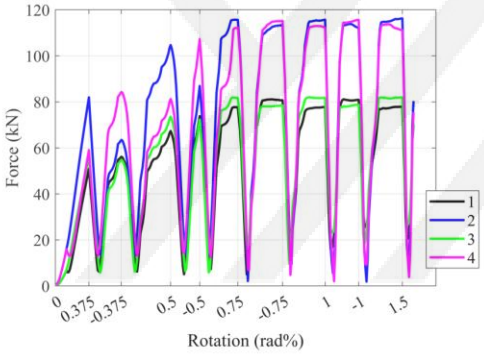

b) T600-F40-1Ls



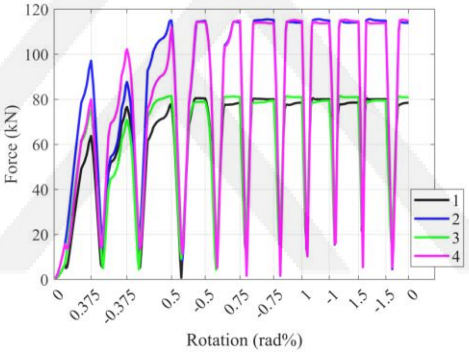

c) T900-F40-1Ls



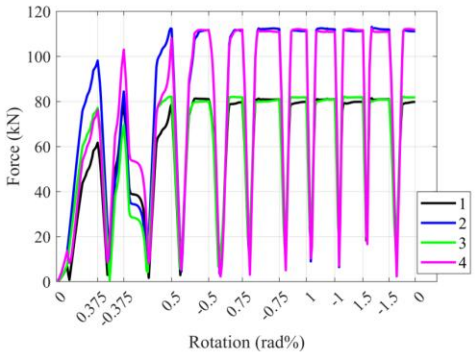

d) T900-F40-1L



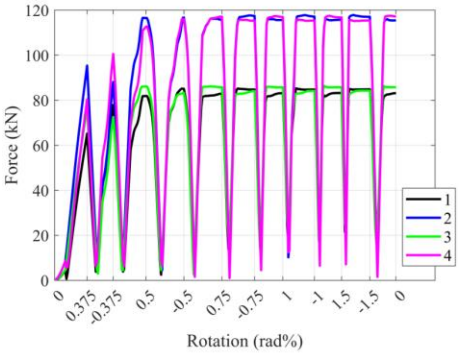

e) T1100-F40-1L




f) T1100-F40-3L




g) T1440-F30-3L




h) T900-F50-3L

**Figure 6.17** The frictional forces developed within the individual friction members

When the graph of the T600-F40-1Ls model given in Figure 6.17(b) is examined, the force levels are observed to be the lowest in this model compared to the other models. While friction elements 1 and 3 on the support side stabilize at approximately 45 kN, elements 2 and 4 on the beam side carry a force of about 60 kN. The curves did not show any significant deterioration throughout the cycles.

By contrast, the T900-F40-1Ls model shown in Figure 6.17(c) exhibited irregular behavior. The force cycles did not repeat each other exactly, and the curves displayed an unstable character.

For the long single plate configuration, The T900-F40-1L model shown in Figure 6.17(d), although having the same pretension level as the T900-F40-1Ls model, exhibited more stable behavior. The force cycles became more regular and reached an approximately constant level as the cycles progressed. Friction elements 1-3 reached approximately 65 kN, while elements 2-4 developed forces up to approximately 95 kN.

In the T1100-F40-1L model shown in Figure 6.17(e), with the increase in bolt pretension force, the force levels in all friction members increased. While the members on the support side transfer approximately 80 kN of force, the members on the beam side reach approximately 115 kN.

In the three plate configuration, the T1100-F40-3L model shown in Figure 6.17(f) exhibited one of the most stable behaviors. With the increase in the number of longitudinal plates to three, the force cycles became more regular. While the friction members on the support side stabilized at approximately 80 kN, the members on the beam side reached approximately 115 kN. In this model, cyclic degradation was at a minimum level.

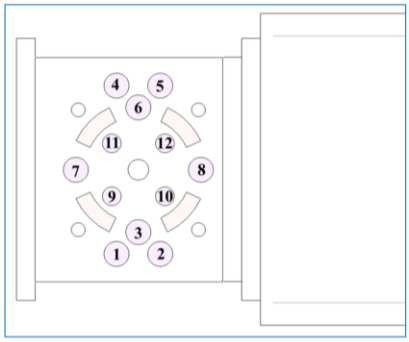
In the T1440-F30-3L model shown in Figure 6.17(g), the friction coefficient was reduced, but the pretension force was increased. The damping capacity values turned out to be close to those of the T1100-F40-3L model. Forces of approximately 80 kN developed in the members on the support side and approximately 110 kN in the members on the beam side. In the T900-F50-3L model shown in Figure 6.17(h), a high friction coefficient was preferred and the pretension force was slightly reduced. Forces reaching approximately 115 kN developed in the friction members

on the beam side, while the members on the support side stabilized at approximately 85 kN.

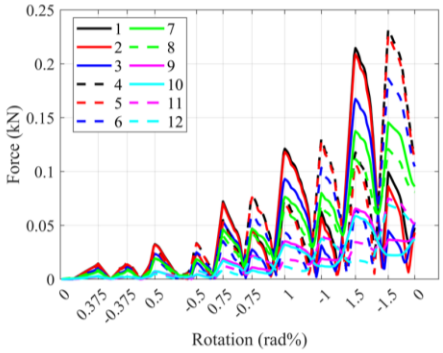
## 6.4 Force Transfer in Elastomeric Pads

The force transfer histories of each elastomeric pad were recorded and the findings are shown in Figure 6.18 below. Each layer contains a total of 12 elastomeric pads. Pads numbered 1–8 have a larger diameter and a larger radial distance. These outer elastomers have a diameter of 40 mm, while the inner pads numbered 9–12 have a diameter of 30 mm. It is expected that the outer elastomers, having a larger moment arm, will contribute more to force transfer.

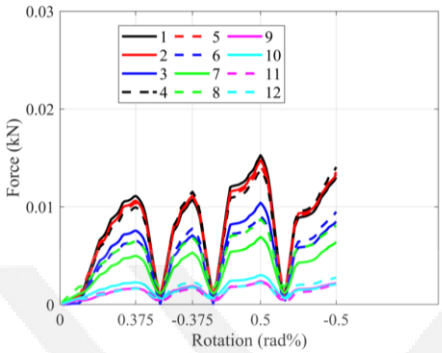
In the T600-F40-1Ls and T900-F40-1Ls models, the forces generated in the elastomeric pads increase with the applied rotation. As seen in Figure 6.18(b), the maximum force reaches approximately 0.23 kN. In contrast, the T900-F40-1Ls model exhibits significantly lower force values, with maximum forces of approximately 0.015 kN (Figure 6.18(c)). In both models, the forces developed in the inner elastomers (pads 9–12) are significantly lower than those in the outer elastomers (pads 1–8). In the T900-F40-1L and T1100-F40-1L models, the elastomeric forces generally increase with rotational demand. As seen in Figures 6.18(c–d), at the peak cycle under 1.5% drift ratio, the elastomers at larger radial distances reach approximately 0.15–0.20 kN, while the inner elastomers develop lower forces. Regular peak formations and cycle-to-cycle increases were observed with increasing rotation. In the multi-plate models (T1100-F40-3L, T1440-F30-3L, and T900-F50-3L), although the elastomer contribution increased noticeably compared to the single-plate models, the total moment remained lower than that of the friction elements, indicating that the elastomers contribute secondarily to the moment capacity.



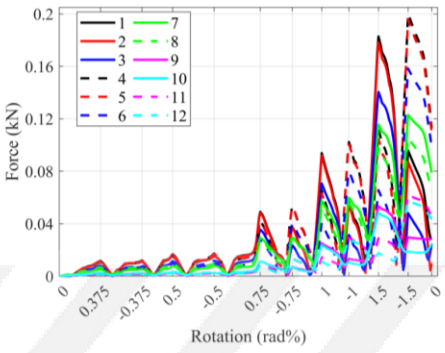

a) Elastomers' number



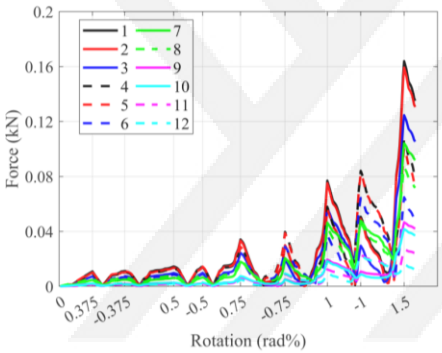

b) T600-F40-1Ls



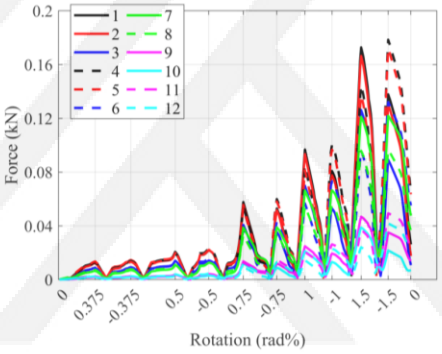

c) T900-F40-1Ls



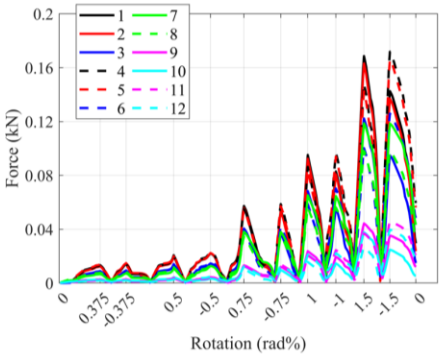

d) T900-F40-1L



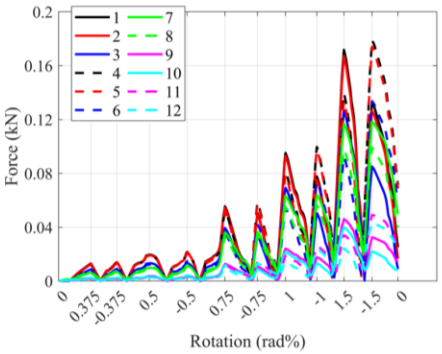

e) T1100-F40-1L




f) T1100-F40-3L




g) T1440-F30-3L




h) T900-F50-3L

**Figure 6.18** Force transfer response of elastomeric pads

# 7
# DISCUSSION

## 7.1 Effect of Embedment Length and Multiple Plates on Damage Mitigation

### 7.1.1 Hysteretic Behavior and Energy Dissipation

The hysteretic behavior and energy dissipation findings presented in Section 6 are evaluated below to assess the influence of embedment length and multiple-plate configurations on cyclic performance.

The findings obtained from the hysteresis curves indicate that the connection behavior was significantly influenced by the embedment length and plate configuration.

The unstable hysteretic behavior observed in the T900-F40-1Ls model indicates that the short single plate configuration was unable to maintain a stable force transfer mechanism throughout the loading protocol. This finding suggests that premature deterioration at the plate–concrete interface and irregularities in force transfer occurred, particularly at large displacement levels. In contrast, the relatively rectangular hysteresis loops observed during the initial cycles of the T600-F40-1Ls model suggest that a certain level of energy dissipation could be achieved despite its lower moment capacity. However, the considerably lower moment capacities of both models compared to the reference RC beam indicate that a single-plate connection detail with a short embedment depth is not a sufficient alternative for such applications.

In the T900-F40-1L and T1100-F40-1L models, where the embedment length was increased, fuller and more stable hysteresis loops were obtained. This observation indicates that sufficient embedment length contributes to maintaining moment

resistance under cyclic loading and allows the connection to reach higher deformation levels.

Among the multi-plate configurations, the most stable hysteretic responses were obtained from the T1100-F40-3L, T1440-F30-3L, and T900-F50-3L models. The transfer of load to the concrete through multiple plates resulted in a more stable cyclic response. This behavior is considered to be associated with a wider distribution of load transfer over the concrete region.

The ability of the hysteresis curves to reach higher rotation levels, their more regular and symmetric shape, and their ability to better preserve their form as the loading cycles progressed indicate that the multi-plate configurations exhibited more stable cyclic behavior. Furthermore, the larger areas enclosed by the hysteresis loops compared to those of the short single-plate configurations indicate a higher energy dissipation capacity. These results demonstrate that the combination of plate number and embedment details has a significant influence on the cyclic performance of the connection.

The cumulative energy dissipation results further support the findings obtained from the hysteresis curves. The fact that the reference RC beam experienced severe damage and collapsed at a drift ratio of approximately 0.71%, dissipating only 2.77 kNm of energy, highlights its limited performance under cyclic loading. In contrast, the device-equipped models continued to dissipate energy up to a drift level of 1.5%, indicating that the proposed connection detail remained effective for a longer duration under cyclic loading.

In the model with a 320 mm long single integrated short plate, such as T900-F40-1Ls, early failure behavior was observed due to severe stress concentrations at the plate tip. The abrupt termination of the thick steel plate within the concrete volume creates a significant stiffness discontinuity; before the friction mechanism fully engages and stable energy dissipation through sliding is achieved, the local bearing stresses occurring at the tip of the short plate exceed the concrete strength. This leads to early internal cracking and loss of structural integrity. The observed difference among short single-plate models lies in the interaction between the pretension force and the embedment length. Although both models have the same embedment length, the T600-F40-1Ls model dissipates 12.0 kNm of energy,

whereas the T900-F40-1Ls model dissipates only 0.63 kNm. This finding indicates that a higher pretension force does not always improve stable behavior in systems with short embedment lengths. The low energy dissipation capacity (0.63 kNm) and irregular force transfer histories observed in the T900-F40-1Ls model are a direct reflection of this adverse interaction.

High energy dissipation values obtained in the T900-F40-1L and T1100-F40-1L models indicate that more stable cyclic responses and sufficient embedment length positively affect system performance. However, although increasing the embedment length to 640 mm in T900-F40-1L delays early yielding, due to the single longitudinal plate, force transfer still occurs in a single plane within the section. Moreover, under high pretension forces, this single-plane transfer causes local yielding in the concrete along the plate boundary; indeed, progressive deformation localization at large displacement rates clearly demonstrates this situation.

The three-plate configuration applied in the 3L-type models emerged as the most effective approach for limiting damage among the investigated parameters. Owing to the presence of three separate longitudinal plates, the effects of shear and compression were distributed over a larger volume of the RC beam, thereby reducing the severity of local bearing stress concentrations. As a result, the damage pattern shifted away from highly localized fracture lines and evolved into a more uniformly distributed crack network, in other words, vertical deformation bands. This distributed load transfer system enabled the friction elements to maintain stable sliding over numerous loading cycles even at large drift levels, resulting in the highest overall energy dissipation performance. Indeed, the energy dissipation values measured in the T1100-F40-3L, T1440-F30-3L, and T900-F50-3L models remained relatively high at approximately 17.4–17.5 kNm compared to the other models. This finding clearly demonstrates the importance of plate continuity and the beneficial effect of using multiple plates in sustaining cyclic behavior.

Overall, both the hysteretic behavior and cumulative energy dissipation results indicate that increasing the embedment length and employing multiple plates improve the seismic performance of the connection. In contrast, short single-plate configurations exhibited more limited performance, particularly under high pretension levels. Therefore, the use of long embedment lengths and multiple plates

is considered to be a more appropriate design approach for the proposed connection system.

### 7.1.2 Plastic Deformation Distributions and Failure Modes

This section evaluates the plastic deformation distributions and failure modes to understand how embedment length and the use of multiple plates influence damage localization and failure mechanisms.

Plastic deformations in the reference RC beam initiated at very low rotation levels, and the equivalent plastic strain reached approximately 0.0034 mm/mm. This value represents a deformation level consistent with the onset of unconfined concrete crushing and the initial yielding of the longitudinal reinforcement. Therefore, this stage can be considered the loading level at which nonlinear behavior begins to become significant in the beam.

At the ultimate loading state of the reference RC beam, the maximum equivalent plastic strain in this region reached a very high value of 0.045 mm/mm. Although this value appears exceptionally large, an important point should be emphasized from a numerical modeling perspective: a plastic strain value of this magnitude does not represent the physical deformation capacity of concrete. In reality, concrete would already have undergone physical failure processes such as cracking, crushing, or spalling before reaching such a deformation level. This high numerical value is a consequence of the smeared crack approach and the exponential softening behavior defined for concrete in the finite element model.

In such models, when damage becomes concentrated within a localized region (strain localization), mathematically excessive strain values may develop in that area. Therefore, the primary finding is not the absolute magnitude of deformation, but rather the severe localization of damage at the support interface and the formation of a conventional flexural failure mechanism.

In the T600-F40-1Ls model, the plastic deformations remained concentrated within limited regions of the embedded zone. This indicates controlled inelastic behavior and stable energy dissipation capacity without sudden overall failure.

Regarding the T900-F40-1Ls model, severe plasticization initiated in the connection region and the damage was no longer controlled but instead became localized within a specific area. This behavior suggests that the short embedment

single-plate T900-F40-1Ls model exhibited a more brittle response and was prone to early damage development due to the concentration of load transfer within a limited region. In addition, the high pretension level in the model appears to have made the load transfer mechanism stiffer, causing deformations to concentrate within a narrow region.

Regarding the longer single-plate models, the T900-F40-1L model exhibited a more controlled strain localization compared to the short single-plate models. In this model, the initiation of severe damage was delayed, and the strain localization zone shifted from the plate end region toward the interior of the beam. Furthermore, increasing the embedment length in the T1100-F40-1L model also delayed the initiation of severe damage and contributed to a more controlled progression of the connection behavior, with the strain concentration propagating along the embedment region rather than remaining localized at a single critical point.

While increasing the embedment length improved the damage distribution in the single-plate models, a more pronounced improvement was observed when the number of embedded plates increased.

This behavior is clearly reflected in the maximum plastic strain values obtained at the end of the loading protocol. The maximum plastic strain values recorded for the T1100-F40-3L, T1440-F30-3L, and T900-F50-3L models were 0.00953 mm/mm, 0.01467 mm/mm, and 0.01116 mm/mm. These values are considerably lower than the value of 0.03618 mm/mm observed in the short single-plate T900-F40-1Ls model. The pronounced strain concentration observed in the single-plate configuration indicates that the transferred forces were resisted within a relatively limited region, resulting in localized damage accumulation. In contrast, the multi-plate configurations promoted a more distributed transfer of strain demands throughout the embedment region, thereby reducing peak plastic deformation values and contributing to more uniform damage distribution.

In general, the use of a seismic energy dissipation device has contributed to addressing earthquake effects in a more controlled manner by altering the damage mechanism that concentrates at the joint region in traditional RC systems. In the models incorporating the seismic device, it was observed that the dominant damage region shifted away from the critical joint interface compared to that observed in

the reference beam. However, the findings indicate that the device does not completely eliminate damage in the RC member but rather modifies the location and development pattern of the damage depending on the embedment detail. In particular, the embedment length and plate configuration were found to have a decisive influence on the stress distribution, damage localization, and overall performance of the connection. Therefore, for seismic devices to be used effectively and safely in RC structures, not only their energy dissipation capacity but also the load transfer mechanism between the device and the RC member, as well as the embedment details, should be carefully designed.

## 7.2 Discussion Of Force Transfer Mechanisms

### 7.2.1 Friction Mechanism

The force transfer histories of the friction elements reveal the effects of plate configuration, pretension force, and friction coefficient on the behavior of the proposed connection. In the T600-F40-1Ls model with a short plate length, the absence of significant deterioration in the force cycles indicates that the system was able to sustain load transfer without developing sudden instability. However, the low force capacity suggests that the friction mechanism was activated only to a limited extent. In the T900-F40-1Ls model, the friction elements were unable to develop stable force transfer and consistent resistance behavior throughout the loading protocol. The irregularities observed in the force cycles suggest that a stable resistance mechanism could not be established on the friction surfaces. This condition may have adversely affected the energy dissipation capacity of the system.

In the T900-F40-1L and T1100-F40-1L models, the improvement in the plate arrangement (longer plate length) resulted in a more balanced contact pressure distribution and provided a relatively more stable force transfer behavior.

Among the investigated models, the T1100-F40-3L model exhibited one of the most regular force transfer behaviors. In this model, the more limited cyclic deterioration may be associated with the ability of the three-plate configuration to distribute contact stresses more uniformly. This result indicates that increasing the

number of longitudinal plates has a positive effect on the stability of the friction mechanism.

In the T1440-F30-3L model, although the friction coefficient was reduced, the increase in pretension force maintained the damping capacity at a level close to that of the T1100-F40-3L model. This result indicates that the increase in pretension force can significantly compensate for the reduction in friction coefficient and that pretension force is a governing parameter affecting the connection behavior.

The T900-F50-3L model was also among the models exhibiting stable force transfer behavior. The combined effect of the relatively high friction coefficient and the three-plate arrangement may have produced a more sustainable friction resistance throughout the loading cycles and contributed to preserving the energy dissipation behavior.

When the 1L (single-plate configuration) and 3L (three-plate configuration) models are compared, it can be observed that the three plate configurations generally produced smoother and more repeatable force transfer curves. In particular, the regular hysteretic behavior observed in the T1100-F40-3L model suggests that the three-plate arrangement provides a more balanced contact mechanism. This condition may have contributed to reducing local irregularities in force transfer and enhancing the overall stability of the system behavior.

The overall evaluation of the graphs indicates that, in all models, the friction elements located on the beam side (Elements 2 and 4) developed higher force levels than the friction elements located on the support side (Elements 1 and 3). This trend suggests that the connection geometry and load transfer path produce a non-uniform force distribution among the friction elements. Consequently, the beam-side friction elements appear to be subjected to greater force demands during the connection response.

The different resistance levels developed in the friction elements are influenced by the geometry of the device and by the different boundary conditions acting on the outer plates located on both sides of the device. In the structural configuration of the device, the outer plate located on the fixed support side is welded directly to the 1st end-plate. When the design pretension force is applied to the main pin and bolts, this welded connection introduces bending and translational restraints in the plate.

The high flexural stiffness of the outer plate and its fixed connection to the support significantly limit its ability to transmit the applied pretension force as normal pressure to Friction Elements 1 and 3.

In contrast, when the bolt pretension force is applied to the system, the outer plate on the beam side is able to undergo inward elastic bending deformation. As a result, the pretension force can be transferred more effectively as normal pressure to Friction Elements 2 and 4. Consequently, higher normal forces develop in the beam-side friction elements, leading to higher frictional resistance levels.

Future studies may investigate alternative design approaches aimed at reducing the resistance differences observed between the friction layers. For this purpose, introducing local gaps in specific regions of the connection may be considered. Local gaps may allow controlled deformation of the connection and facilitate a more effective transfer of pretension force to the friction surfaces. In this way, the stiffness effect caused by the welded connection may be reduced, and a more balanced normal pressure distribution among the friction layers may be achieved.

As another approach, independent clamping systems may be employed. In such systems, the clamping force applied to each friction layer can be controlled separately, thereby reducing differences in pretension force between the layers. This may enable a more uniform distribution of normal force among the friction elements.

Furthermore, revising the weld detail of the outer plate on the support side may also be considered. The current weld detail restricts the deformation capacity of the outer plate and may adversely affect the transfer of pretension force to the friction layers. By adopting a more flexible weld arrangement or alternative connection details, the outer plate may be allowed to undergo limited deformation under pretension. This could improve the transfer of pretension force to the friction surfaces and reduce the differences in frictional resistance observed between the layers.

Such design improvements may contribute to achieving a more balanced normal pressure distribution among the friction layers and help the internal force transfer mechanism of the device operate in a more uniform manner.

### 7.2.2 Elastomeric Pad Mechanism

In the T900-F40-1L and T1100-F40-1L models, the force transfer behavior of the elastomeric pads exhibited a regular progression with increasing rotation demand. Although the elastomer forces reached approximately 0.15–0.20 kN during the peak cycles, these values remained considerably lower than the resistance levels developed by the friction elements. This indicates that, in these models, the elastomers functioned primarily as a supplementary energy dissipation mechanism rather than as the primary load-carrying component.

In the three-plate models (T1100-F40-3L, T1440-F30-3L, and T900-F50-3L), the contribution of the elastomers was observed to increase compared to the single-plate models. However, the total moment generated by the elastomers remained lower than the moment capacity provided by the friction elements in these models as well. This result indicates that increasing the elastomer contribution supports the overall system performance but does not alter the mechanism controlling the primary moment capacity.

When the contribution of the elastomer to the moment capacity is evaluated, the forces developed in the elastomeric pads increased with the applied rotation demand, whereas the friction members remained the primary component governing the ultimate moment capacity. The elastomers mainly provided additional energy dissipation, resulting in a limited contribution to the overall moment capacity.

This limited contribution may be related to the applied loading protocol. The maximum rotation demand imposed on the cantilever beam was limited to a drift ratio of 1.5%, which may not have provided sufficient deformation for the elastomers to become fully engaged. Since the restoring force developed by the elastomeric pads increases with their shear deformation and, consequently, with the rotation demand, higher drift levels may allow greater deformation and a more pronounced contribution to the overall system behavior and energy dissipation.

# 8
# LIMITATIONS AND FUTURE RESEARCH

The numerical model developed within the scope of this study successfully reflects the fundamental hysteretic behavior of the proposed connection device under idealized conditions. However, it also brings along some important limitations.

One of the most significant limitations of the numerical model in this study is the simplified representation of the interface between the embedded longitudinal steel plates and the surrounding concrete. A fully bonded contact has been defined between these two materials, and full compatibility and complete strain transfer are assumed between them. Contrary to the actual RC behavior, this assumption does not take into account mechanisms such as bond-slip, localized crushing, and potential separation that could occur under cyclic loading [47]. The existing model in this study is insufficient in representing these mechanisms. To overcome these limitations, a more realistic bond formulation should be adopted at the steel-concrete interface in future investigations. For future numerical simulations, it is suggested that interface models based on cohesive zone or bond-slip relationships be employed to capture the variation of force transfer along the embedded length and the progressive damage development at the interface.

Another significant limitation of the numerical model in this study is the omission of transverse reinforcement (stirrups) along the embedded region of the longitudinal steel plate. In the current model, the depth of the beam and embedded plate were assumed to be equal, the plate was positioned with zero clearance from the bottom and top surfaces of the beam. Since stirrups cannot be placed along the embedded region due to the presence of the plate, this assumption leads to an overestimation of the shear capacity. The inability to model stirrups in the embedded region also prevents the direct representation of the confinement effect, which enhances the compressive strength and ductility of concrete through lateral pressure applied to

the concrete core. Furthermore, the contributions of stirrups in restraining crack widths by holding crack surfaces together and improving the performance under service conditions are also disregarded in the current model. Moreover, both the confined and unconfined concrete regions were characterized by a single concrete material model. This approach disregards the beneficial effects of confinement on concrete strength and ductility and provides only an idealized representation of the local damage occurring in this region. Future work should explore alternative geometric configurations that permit the placement of stirrups throughout the embedment zone. For example, transferring the connection at the second end plate to the RC beam through anchor bars, rather than through an embedded longitudinal plate, may allow the stirrups to remain continuous throughout the embedment region.

An additional limitation concerns the simplifications adopted in modeling the connection device. In the present finite element models, both the friction coefficient and the bolt pretension force were assumed to remain constant over the entire course of the analysis. Furthermore, these studies also indicated that wear developed on the sliding surfaces under repeated loading resulted in loss of pretension and a progressive reduction in moment capacity.

Among the advanced design enhancements not incorporated into the numerical models of this study, surface hardening was applied to the secondary inner plates, and Belleville washers (disc springs) were utilized in bolt assemblies in both series and parallel configurations.

These modifications were observed to improve the stability of the pretension force and the persistence of moment capacity over repeated load cycles. Such improvements were not integrated into the numerical models of the current study and were therefore considered beyond its scope. This approach presents promising prospects for future developments. The current investigation, however, was dedicated to examining the fundamental hysteretic behavior of the device under idealized conditions.

Beyond these modeling considerations, the application of the device in RC systems and the provision of its replaceability also involve significant design and implementation challenges. This device was designed to function as a replaceable

seismic fuse that protects the load-bearing system in steel structures. This capability has been validated in steel beam-to-column connections. However, in RC applications, it was observed that the level of protection against potential damage in the beam varies depending on the configuration of the longitudinal plates. According to the capacity design approach, the T600-F40-1Ls model achieved the desired performance criterion with an average moment capacity ratio of 0.69. However, in this model, local concrete damage has occurred in the embedded area due to the short embedding length. This situation proves that the success of protection against damage in structural elements depends not only on global-scale capacity ratios but also on local-level force transfer details. Therefore, it appears that the replaceability of the device in RC elements after an earthquake will largely depend on the quality of detailing in the embedded region and the severity of the damage occurring in that area.

In order for the system in which the device works together with an RC element to be realistically understood, it is clear that the integrated system should be experimentally tested in the future. These experiments will allow the examination of the effects of critical issues such as bond slip behavior at the steel-concrete interface, localized damage in the concrete, transfer of internal forces, and cyclic interaction between the embedded plate and the surrounding concrete.

In future numerical studies, geometric alternatives that allow the modeling of stirrups along the embedment region should be developed. This approach will enable a more realistic representation of the positive contributions of confinement on concrete strength and deformation capacity. In this way, the effects of transverse reinforcement in limiting crack widths by holding crack surfaces together and improving performance under service conditions could also be incorporated into the numerical analyses. Another issue to be considered is the interface wear in the models. Micro-wear resulting from repeated cycles on sliding surfaces causes the friction coefficient to change over time, thereby gradually reducing the bolt pretension force. Accounting for this loss in the numerical modeling is of great importance for evaluating the realistic long-term cyclic performance of the device.

# 9
# CONCLUSION

In this study, a friction and elastomer-based seismic device was placed inside an RC beam. The energy dissipation capacity of the system, damage mechanisms, and force transfer characteristics were examined. This hybrid system provided a positive perspective for low-damage seismic design, but it was observed that design should be carried out with careful attention to detailing.

1- In conventional RC beams, energy dissipation primarily occurs through plastic hinging within the plastic hinge region. In the proposed system, however, a portion of this dissipative demand is transferred to the integrated steel fuse device, thereby reducing the damage concentration in the plastic hinge region.
2- Instead of aiming for damage-free behavior, an approach in which damage is concentrated in controlled areas and energy dissipation is provided through certain mechanisms is more realistic for RC systems. The results of this study have shown that the proposed system does not completely eliminate damage in RC elements, but it can reduce the damage intensity in critical areas by changing the distribution and development mechanism of the damage.
3- The results showed that system performance largely depends on the force transfer mechanism between the embedded steel plates and the surrounding concrete. The embedment length is a critical parameter that determines joint performance. Short single-plate configurations exhibited unstable hysteretic behavior and limited deformation capacity at high prestress levels. Extending the embedment length in single-plate models delayed damage initiation.

4- The distributed force transfer has decisively improved the system's behavior. Three-plate configurations have effectively reduced damage localization by spreading the force transfer over a larger volume of concrete and have provided a more uniform stress distribution in the concrete core. This situation has increased the cyclic stability of the joint, enhanced the deformation capacity, and contributed to obtaining a more effective energy dissipation behavior.
5- While increasing the embedment length has improved performance in single-plate models, it has not completely eliminated the fundamental limitations of single-plane force transmission. When all performance indicators are evaluated together, it has been observed that the most successful behavior is obtained in configurations where a long embedment length is used together with multiple plates.
6- In the examined deformation range, the system behavior was largely controlled by the friction mechanism. While the elastomeric pads contributed to the deformation capacity and system behavior, their effects on moment capacity and energy dissipation remained limited compared to the friction elements. Therefore, while the elastomeric components played a complementary role, the main energy dissipation mechanism was provided by the friction elements.

As a result, this study has demonstrated the feasibility of the integrated hybrid seismic damping system developed for RC elements and has shown that the system holds significant potential in terms of low-damage design. However, to ensure reliable and sustainable performance, the device-concrete interaction, force transfer details, and local stress distributions must be carefully designed. This favorable low-damage behavior can be achieved with carefully designed embedding details. Future studies are recommended to focus on the bond-slip behavior, the effects of local wrapping, the optimization of the force transfer mechanism, and the experimental verification of behavior at higher displacement levels.

# REFERENCES


[1] G. M. Calvi, M. J. N. Priestley, and M. J. Kowalsky, "Displacement-Based Seismic Design of Structures," in *Proc. 3rd Panhellenic Conf. Earthquake Eng. and Technical Seismology*, Nov. 5–7, 2008.

[2] V. V. Bertero, "Ductility based structural design," in *Proc. 9th World Conf. Earthquake Eng.*, Tokyo–Kyoto, Japan, vol. VIII, 1988.

[3] R. E. Vargas and M. Bruneau, *Analytical Investigation of the Structural Fuse Concept*, Technical Report MCEER-06-0004, University at Buffalo, State University of New York, Buffalo, NY, USA, 2006.

[4] C. Soydan, H. Özkaynak, M. Sürmeli, E. Şenol, H. Saruhan, and E. Yüksel, "A moment resistant beam end connection using energy dissipative couplers for precast concrete structures," *Bulletin of Earthquake Engineering*, vol. 23, no. 1, pp. 453–487, 2025, doi: 10.1007/s10518-024-02067-9.

[5] P. Colajanni, L. La Mendola, A. Monaco, and S. Pagnotta, "Low-Damage Friction Connections in Hybrid Joints of Frames of Reinforced-Concrete Buildings," *Applied Sciences*, vol. 13, no. 13, p. 7876, 2023, doi: 10.3390/app13137876.

[6] X. Qu, C. Qin, G. Sun, Y. Deng, and X. Fu, "Seismic behavior of precast prestressed concrete frame joints with different energy dissipation designs," *Advances in Structural Engineering*, vol. 27, no. 1, pp. 51–71, 2024, doi: 10.1177/13694332231213455.

[7] D. Sonda and A. V. Pollini, "TH analyses and simplified approach for precast RC frames retrofit with dissipative fuse devices Sismocell," *Procedia Structural Integrity*, vol. 44, pp. 1188–1195, 2023, doi: 10.1016/j.prostr.2023.01.153.

[8] G. Dougka, D. Dimakogianni, and I. Vayas, "Innovative energy dissipation systems (FUSEIS 1-1)—Experimental analysis," *Journal of Constructional Steel Research*, vol. 96, pp. 69–80, 2014, doi: 10.1016/j.jcsr.2014.01.003.

[9] M. Pratap and G. R. Vesmawala, "An experimental and numerical analysis of slit plate as replaceable fuse in moment resisting frame," *Structures*, vol. 67, Art. no. 107011, 2024, doi: 10.1016/j.istruc.2024.107011.

[10] T. N. Nguyen and M. R. Eatherton, "Computational and experimental study of structural fuses optimized to resist buckling," *Journal of Constructional Steel Research*, vol. 201, Art. no. 107688, 2023, doi: 10.1016/j.jcsr.2022.107688.

[11] A. Farzampour, "Structural behavior prediction of the Butterfly-shaped and straight shear fuses," *Structures*, vol. 33, pp. 3964–3972, 2021, doi: 10.1016/j.istruc.2021.07.008.

[12] J. A. Avecillas and M. R. Eatherton, “Topology optimization of steel shear fuses to resist buckling,” in *Proceedings of the Annual Stability Conference*, Structural Stability Research Council, St. Louis, MO, USA, Apr. 2–5, 2019.

[13] S. M. Goshtaei, S. Moradi, and K. M. A. Hossain, “Multi-objective optimization of energy-dissipating steel plate fuse links using response surface method,” *Structures*, vol. 62, Art. no. 106224, 2024, doi: 10.1016/j.istruc.2024.106224.

[14] M. R. Eatherton and T. N. Nguyen, “Structural fuse shapes for resilient structures,” in *Proc. 18th World Conf. Earthquake Engineering (WCEE2024)*, Milan, Italy, 2024, pp. 1–11.

[15] M. Ferraioli, S. Mottola, E. Mistakidis, and G. De Matteis, “Lateral torsional buckling design of dumbbell-shaped steel strip dampers,” *Structures*, vol. 77, Art. no. 109080, 2025, doi: 10.1016/j.istruc.2025.109080.

[16] M. P. Sarkisian, “Building systems using seismic fuses with advanced material and friction,” in *Life-Cycle Performance of Structures and Infrastructure Systems in Diverse Environments*, Y. Li and D. M. Frangopol, Eds. London, U.K.: Taylor & Francis, 2025, pp. 302–309, doi: 10.1201/9781003595120-36.

[17] M. Latour, V. Piluso, and G. Rizzano, “Experimental analysis of beam-to-column joints equipped with sprayed aluminium friction dampers,” *Journal of Constructional Steel Research*, vol. 146, pp. 33–48, 2018, doi: 10.1016/j.jcsr.2018.03.014.

[18] Y. Cui, Z. Yan, X. Wang, and T. Wang, “Experimental studies on slip friction device using symmetric friction connections,” *Structures*, vol. 44, pp. 1886–1897, 2022, doi: 10.1016/j.istruc.2022.09.005.

[19] C. Yang, L. Xie, A. Li, B. Liu, and Y. He, “Experimental study of rotational friction damper for seismic response control: Friction material comparison and configuration optimization,” *Case Studies in Construction Materials*, vol. 21, Art. no. e03825, 2024, doi: 10.1016/j.cscm.2024.e03825.

[20] A. Bozer, H. Özgan, and N. Yıldız, “A novel friction-based energy dissipation system for seismic applications,” in *IWEBSE 2025*, Lecture Notes in Civil Engineering, vol. 692, pp. 325–337, Springer, 2025, doi: 10.1007/978-3-031-97129-7_26.

[21] R. W. K. Chan and W. Tang, “Serviceability conditions of friction dampers for seismic risk mitigations,” *Structures*, vol. 35, pp. 500–510, 2022, doi: 10.1016/j.istruc.2021.11.033.

[22] G. Lomiento, N. Bonessio, and G. Benzoni, “Friction model for sliding bearings under seismic excitation,” *Journal of Earthquake Engineering*, vol. 17, no. 8, pp. 1162–1191, 2013, doi: 10.1080/13632469.2013.814611.

[23] B. Shahbazi and E. Moaddab, “A new hybrid friction damper (HFD) for dual-level performance of steel structures,” *International Journal of Steel Structures*, vol. 21, no. 4, pp. 1332–1345, 2021, doi: 10.1007/s13296-021-00507-9.

[24] He, X., Ke, K., Guo, L., Yam, M. C., & Wang, Z. (2021). A Hybrid Simulation of Controlled R: Force transfer mechanism and design considerations. Journal of Constructional Steel Research, 183, 106760. Doi: 10.1016/j.jcsr.2021.106760

[25] Z. Zhai, F. Zhou, Y. Liu, Y. Ma, and M. Zhang, “Seismic performance assessment of metal-friction hybrid damper linked steel frame considering extremely rare earthquakes,” *Journal of Building Engineering*, vol. 84, Art. no. 108638, 2024.

[26] P. Richards, “A repairable connection for earthquake-resisting moment frames,” *Steel Construction*, vol. 12, no. 3, pp. 191–197, 2019, doi: 10.1002/stco.201900015.

[27] J. Tian, Z. Wang, and J. Pan, “Research on design guidelines for steel beam-to-column connections with replaceable buckling-restrained fuse plates,” *Journal of Constructional Steel Research*, vol. 232, Art. no. 109622, 2025, doi: 10.1016/j.jcsr.2025.109622.

[28] Yılmaz, O. "Depreme Dayanıklı Çelik Çerçevelerde Hasar Alan veya Almayan Yüksek Enerji Tüketen Moment Birleşimlerinin Geliştirilmesi" (Development of Damaged or Non-damaged High Energy Dissipative Moment Connections in Seismic Resistant Steel Frames), PhD Thesis, Yildiz Technical University, 2022. (in Turkish)

[29] Ansys® Academic Research Mechanical, Release 2024 R2, ANSYS, Inc.

[30] Yılmaz, O., Bekiroğlu, S. "Bilhassa binalarda kullanılmak üzere sürtünmeli ve elastomerli sismik birleşim aparatı" (A seismic combination apparatus with elastomer and with friction particu larly for use in buildings), Turkish Patent and Trademark Office, Ankara, Türkiye, Patent No: TR 2020 18195, 2024. (in Turkish)

[31] J. N. Reddy, *An Introduction to the Finite Element Method*, 3rd ed. New York, NY, USA: McGraw-Hill, 2006.

[32] D. L. Logan, *A First Course in the Finite Element Method*, 4th ed. Toronto, ON, Canada: Nelson, 2007.

[33] ANSYS Inc., Mechanical APDL Element Reference, Release 2024 R2, 2024. [Online]. Available: ANSYS Help Documentation

[34] ANSYS Inc., Motion in Workbench User Guide: Contact Types, Release 2025 R1, 2025. [Online]. Available: ANSYS Help Documentation

[35] The Mathematical Theory of Plasticity, Oxford University Press, 1950.

[36] P. J. Armstrong and C. O. Frederick, A Mathematical Representation of the Multiaxial Bauschinger Effect, Report RD/B/N731, Central Electricity Generating Board (CEGB), Berkeley, UK, 1966.

[37] J. L. Chaboche, “A review of some plasticity and viscoplasticity constitutive theories,” International Journal of Plasticity, vol. 24, no. 10, pp. 1642–1693, 2008.

[38] Menétrey, P., Numerical Analysis of Punching Failure in Reinforced Concrete Structures, École Polytechnique Fédérale de Lausanne (EPFL), Lausanne, Switzerland, 1994.

[39] Willam, K.J. and Warnke, E.P., “Constitutive Model for the Triaxial Behaviour of Concrete,” IABSE Reports, vol. 19, pp. 1–30, 1974.

[40] Mestnikov, V.V., Mestnikova, I.V. and Mestnikov, V.V., “Nonlinear Analysis of Stress-Strain of Reinforced Concrete Beam in Ansys Using the Menetrey-Willam Model,” in Hydraulic and Civil Engineering Technology VIII, IOS Press, 2023, pp. 470–475. doi:10.3233/ATDE230751.

[41] R. W. Ogden, Non-Linear Elastic Deformations, Oxford, U.K.: Oxford University Press, 1984.

[42] M. Arduini, A. Di Tommaso, and A. Nanni, “Brittle failure in FRP plate and sheet bonded beams,” *Structural Journal*, vol. 94, no. 4, pp. 363–370, 1997, doi: 10.14359/487.

[43] M. Gerami, H. Saberi, V. Saberi, and A. S. Daryan, "Cyclic behavior of bolted connections with different arrangement of bolts," *Journal of Constructional Steel Research*, vol. 67, no. 4, pp. 690–705, Apr. 2011, doi: 10.1016/j.jcsr.2010.11.011.

[44] F. Naeim and J. M. Kelly, *Design of Seismic Isolated Structures: From Theory to Practice*. New York, NY, USA: John Wiley & Sons, 1999.

[45] G. L. Kulak, J. W. Fisher, and J. H. Struik, *Guide to Design Criteria for Bolted and Riveted Joints*, 2nd ed. Chicago, IL, USA: American Institute of Steel Construction, 2001.

[46] American Institute of Steel Construction, *Seismic Provisions for Structural Steel Buildings*, ANSI/AISC 341-16. Chicago, IL, USA: American Institute of Steel Construction, 2016.

[47] Eligehausen, R., Popov, E. P., Bertero, V. V. "Local bond stress-slip relationships of deformed bars under generalized excitations: experimental results and analytical model", College of Engineering, University of California, Berkeley, CA, USA, Rep. UCB/EERC-83/23, 1983 [online] Available at: https://nehrpsearch.nist.gov/static/files/NSF/PB84192848.pdf [Accessed: 13 March 2026]

[48] The MathWorks, Inc., MATLAB, Natick, MA, USA, 2024.

# A
# EFFECT OF LONGITUDINAL PLATE GEOMETRY ON THE SEISMIC PERFORMANCE OF RC BEAMS

This chapter focuses on the effects of the geometry of embedded longitudinal steel plates connecting the device to the reinforced concrete element on the energy dissipation capacity, hysteretic behavior, and damage distribution when a friction and elastomeric seismic connection device is entegrated into a reinforced concrete beam.

## A.1 Geometry of the RC Beam

In the preliminary study, the RC beam defined in Section 5.2 of this thesis was adopted as the reference model. This model does not contain any energy dissipation device and has a cross-section of 250×500 mm and a length of 4000 mm. The theoretical flexural moment capacity of the reference beam was determined to be approximately 206 kNm, according to the calculations given in Section 5.9. This model was used as the basis for comparing the hysteretic behavior, energy dissipation capacity, and damage distribution of the models with the device.

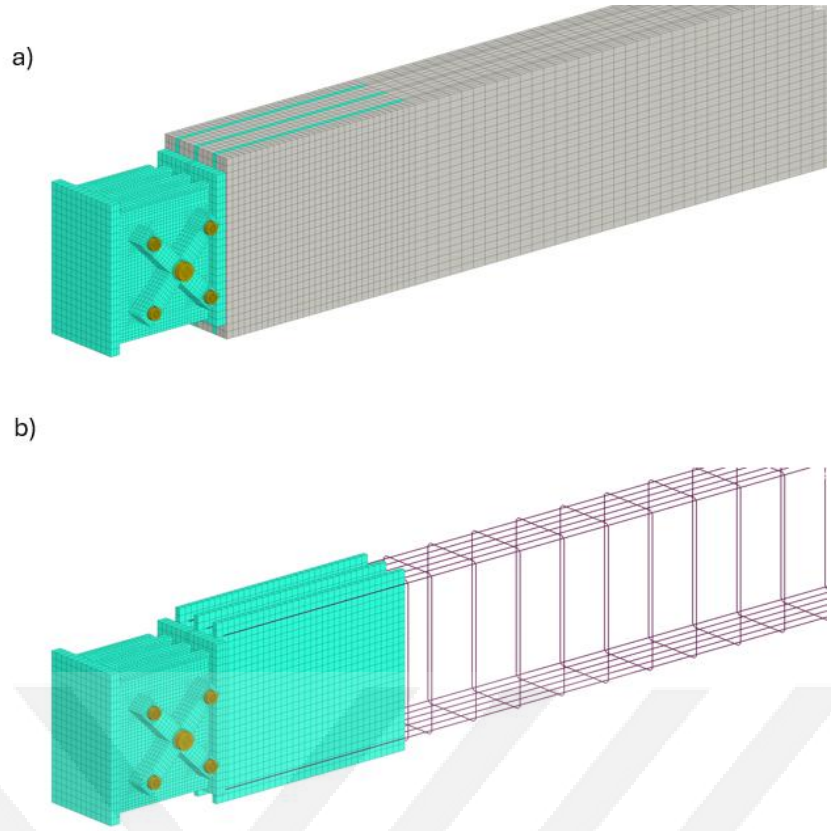



**Figure A.1** General view of Model 1 and the placement of longitudinal steel plates within the reinforced concrete beam: (a) general model view, (b) placement of embedded longitudinal plates

### A.1.1 Model 1

In Model 1, the friction and elastomeric seismic device is modeled as entegrated in the end region of the reinforced concrete beam. The general view of the model is shown in Figure A.1(a). Three longitudinal steel plates are attached to the device in order to provide force transfer between the device and the RC element. By using these plates, it is aimed to transfer the moment and shear forces generated within the device to the reinforced concrete element through the embedded plates. Figure A.1(b) shows the placement of the longitudinal steel plates within the reinforced concrete beam. The longitudinal plate positioned in the middle is located along the central axis of the beam. The other plates are positioned symmetrically on both sides at spaced intervals.

The plates are welded to the end plate of the device and are designed to continue with a constant cross-sectional depth along the beam. Plates with constant depth were preferred because it is aimed to achieve a more uniform force transfer along

the plate and to prevent local stress concentrations caused by sudden cross-sectional changes.

Model 1 does not involve any reduction or inclination in the plate geometry. Therefore, it is used as a reference model for comparison with other tapered models. In the models with the device, the total pretension force was applied as 600 kN, and the friction coefficient was taken as 0.4. In this case, the theoretical moment capacity of the models with the device is calculated as 141.44 kNm.

### A.1.2 Model 2

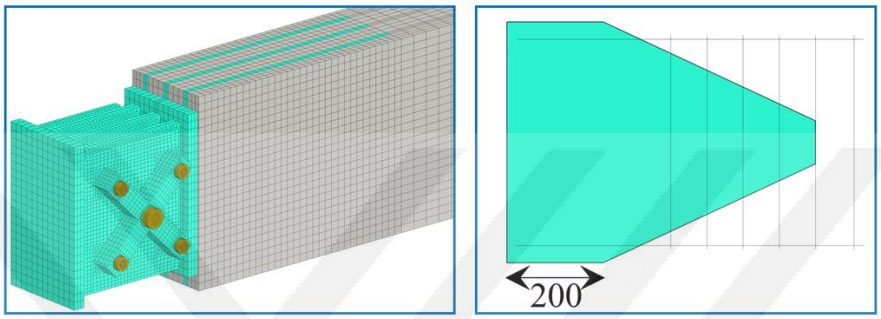



**Figure A.2** Finite element representation of Model 1 and the longitudinal plate configurations adopted in Models 2 and 3.

In Model 2, the same frictional and elastomeric seismic device as in Model 1 was used. In this model, however, the geometry of the longitudinal steel plates connecting the device to the reinforced concrete member was modified. As shown in Figure A.2(b), the plates maintain a constant cross-sectional depth over the first 200 mm from the device connection region, after which they taper toward the interior of the beam at an angle of 15°.

### A.1.3 Model 3

Model 3 has the same geometric characteristics as Model 2, differing only in the adoption of a greater taper angle for the longitudinal plates. This taper angle was selected as 25°. Although the basic configuration of the plate geometry illustrated in Figure A.2(b) is maintained, the tapering ratio is amplified, resulting in a more distinct change in cross-sectional depth.

Model 3 represents the configuration with the highest taper angle examined in this study and is compared with Models 1 and 2 in order to determine the effects of plate geometry on the local behavior.

The angular variation adopted in the geometries is intended to enable a more gradual transfer of the force from the tapered plate to the reinforced concrete beam. This geometric modification was implemented based on the consideration that force transfer in plates with constant cross-section may concentrate in specific regions. By introducing a taper angle to the plate depth, the gradual reduction in cross-section is expected to distribute the stress over a wider area.

The aim was to investigate how the force transfer mechanism between the differently modeled plates and the surrounding concrete, as well as the local damage that may develop, are influenced by plate geometry.

## A.2 Results

### A.2.1 Hysteretic Response

The moment-rotation curves obtained for the reference beam, Model 1, Model 2, and Model 3 are shown in Figure A.3 below. The responses of these models are assessed collectively and displayed in a comparative manner within a single plot.

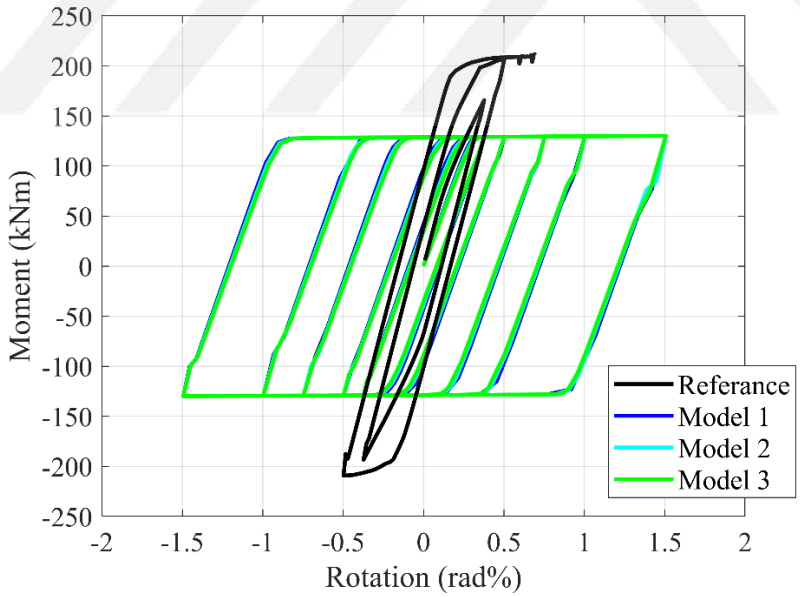



**Figure A.3** Moment–rotation responses of the reference beam and Models 1-3.

As seen in Figure A.3, the reference beam reached an approximate moment capacity of 206 kNm, while the models with fixtures developed a moment capacity of around

125–130 kNm. Moreover, it is observed that the models with fixtures generated stable and repeatable hysteretic cycles throughout the loading cycles.

When examining the graph, it is observed that the differences in plate geometry among all the models with device (Model 1-2-3) do not have a significant effect on the overall behavior. Model 1, which uses a constant cross-section plate, and Models 2 and 3, which have tapered plate geometries, exhibited similar moment capacity, stiffness, and cyclic behavior. Additionally, no significant strength degradation or instability was observed among the models. The hysteresis curves show similar values and behaviors. Therefore, it is assessed that the plate geometry has a greater effect on the force transmission mechanism and local damage distribution rather than on the overall hysteretic behavior of the system.

It is observed that the energy dissipation capacity from the areas under the hysteretic loops is similar for all three-device models. However, in order to numerically verify this observation, the cumulative energy dissipation capacities of the models are compared in the next section.

### A.2.2 Energy Dissipation Capacity

In Figure A.4, the total amount of energy consumed by the reference beam and the models with attachments during cyclic loading is compared.

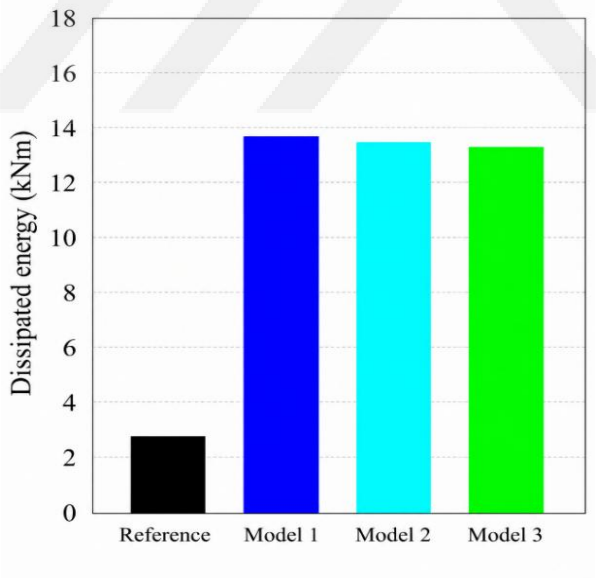



**Figure A.4** Dissipated energy values of the reference beam and Models 1–3.

The reference reinforced concrete beam exhibited an energy dissipation capacity of approximately 2.77 kNm. In contrast, the cumulative energy dissipation capacities

of the device-integrated models ranged between 13.4 and 13.7 kNm. Accordingly, the utilization of the friction and elastomeric seismic device enabled approximately a fivefold increase in energy dissipation capacity compared to the reference RC beam. This indicates that a substantial portion of the energy induced under seismic effects is dissipated through the friction mechanism and the elastomeric components within the device. When comparing Model 1, Model 2, and Model 3, only minor differences were observed among their energy dissipation capacities.

### A.2.3 Equivalent Plastic Strain Distributions

Figure A.5 presents the equivalent plastic strain distributions of the reference beam and the device-equipped models.

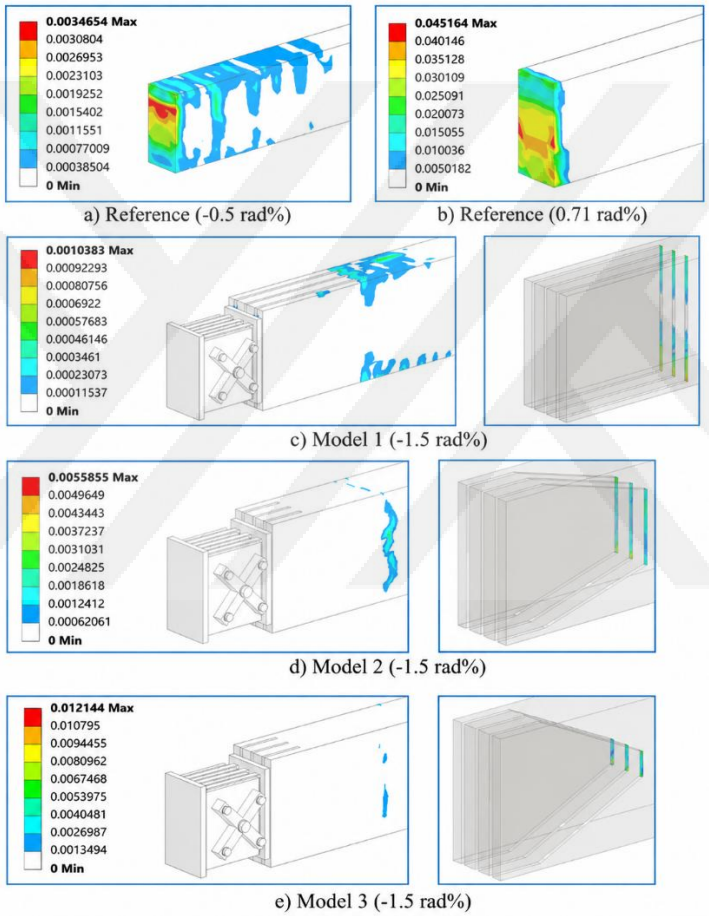



**Figure A.5** Equivalent plastic strain distributions of the reference beam and Models 1–3

In the reference beam, plastic deformations were observed to concentrate in the support region. This indicates that, similar to conventional RC behavior, the energy dissipation under seismic effects occurs within the plastic hinge zone. The

maximum plastic strain value was obtained as approximately 0.045. In the device-integrated models, however, the plastic deformations were observed to shift away from the support region and concentrate at the locations where the embedded connection plates terminate. This outcome demonstrates that the seismic device modifies the force transfer mechanism and redistributes the damage location.

Among the device-integrated models, the lowest maximum plastic strain value was obtained in Model 1, which features longitudinal plates with constant cross-sectional depth, and the plastic deformations remained at more limited levels. In Model 2, where the plate depth was gradually reduced, the maximum plastic strain value increased, and this increase became more pronounced in Model 3, in which the taper angle was further enlarged. With a maximum plastic strain value of approximately 0.012, Model 3 exhibited the highest level of plastic deformation among the models equipped with the device. In Model 3, the local plastic deformation level was elevated, and the damage was concentrated in a confined region. The distribution of plastic deformations indicated that the plate geometry plays a more decisive role in the local behavior.

## A.3 Discussion

In this chapter, the effects of embedded steel plate geometries in a friction and elastomeric seismic connection device on the RC beam were investigated. The device-integrated models exhibited more stable hysteretic behavior and provided higher energy dissipation capacity compared to the reference beam. When the effects of plate geometry were examined, it was observed that the geometric modifications made to the embedded connection plates did not have a significant influence on the moment capacity and energy dissipation characteristics of the system, as these values remained at similar levels. In contrast, the plate geometry was found to be more decisive on the local behavior. The tapering in the plate geometry altered the force transfer mechanism, leading to the concentration of plastic deformations at the plate termination regions. It was determined that as the taper angle increased, local plastic deformation levels rose and damage became more localized in confined zones. This indicates that the force transfer occurs over a smaller region, resulting in increased local stress concentration

# PUBLICATIONS FROM THE THESIS

**Conference Papers**

1. **L. Oğuz**, O. Yılmaz "Betonarme Kirişte Sürtünmeli ve Elastomerli Sismik Birleşim Aparatının Sayısal Olarak İncelenmesi," *GRAD SYMPOSIUM'26*, Fen Bilimleri Enstitüsü, Yıldız Teknik Üniversitesi, İstanbul, Türkiye, 13–14 Mayıs 2026

**Paper**

1. O. Yılmaz, **L. Oğuz**, "Numerical Investigation of RC Beams with an Integrated Frictional and Elastomeric Seismic Device," *Periodica Polytechnica Civil Engineering*, 70(2), pp. 698–716, 2026.